BILINGUAL PUBLISHING GROUP
Pioneer of Global Academics Since 1984

Volume 5 · Issue 1 · January 2023 ISSN 2810-9384(Online)

Advances in Geological and Geotechnical Engineering Research

BILINGUAL
PUBLISHING GROUP
Pioneer of Global Academics Since 1984

Volume 5 Issue 1 • January 2023 • ISSN 2810-9384 (Online)

Advances in Geological and Geotechnical Engineering Research

BILINGUAL PUBLISHING GROUP
Pioneer of Global Academics Since 1984

BILINGUAL PUBLISHING GROUP
Pioneer of Global Academics Since 1984

Volume 5 | Issue 1 | January 2023 | Page1-85

Advances in Geological and Geotechnical Engineering Research

Contents

Articles

BILINGUAL PUBLISHING GROUP
Pioneer of Global Academics Since 1984

Advances in Geological and Geotechnical Engineering Research
https://journals.bilpubgroup.com/index.php/agger

ARTICLE

Geometrical Effect of Under-reamed Pile in Clay under Compression Load Numerical-Study

Ahmed M. Nasr*, *Waseim R. Azzam*, *Ibrahim S. Harran*

Faculty of Engineering, Tanta University, Tanta, 002040, Egypt

ABSTRACT

Recently, the use of deep foundations has increased as a result of the expansion in the construction of high-rise buildings, train tracks, and port berths. As a result of this expansion, it was necessary to use deep foundations that have low cost, high bearing loads, low settlement, and construction time, and such foundations are subjected to different types of loads such as lateral, vertical compression, and tension loads. This research paper will present one of the most important types of deep foundations that are aptly used in such structures and the most important factors affecting their bearing capacity and settlement in stiff clay. This type of deep foundation is called an under-reamed pile. The factors used in this study are pile length to diameter ratio L/D = 30, bulb diameter ratio (Du/D = 1.5, 2, 2.25, and 2.5), number of bulbs (N = 1, 2, and 3), and spacing ratio (S/D = 2 to 8). To investigate the effects of these parameters and obtain optimal results, the PLAXIS 3D was used. The analysis shows that the increase in bulb diameter increases the bearing load by 43%. Bulb spacing controls the failure mechanisms, whether cylindrical shear failure or individual failure and increases the capacity by 66% and 99%, respectively, for two and three bulbs when the bulb spacing becomes S/D = 8. When the number of bulbs increases to three, the capacity increases by 90%. If each bulb works individually, the bearing capacity doubles.

Keywords: Under-reamed pile; Bulb number; Bulb diameter; Bulb spacing; Bearing capacity

1. Introduction

Under-reamed piles have been constructed in Texas since the 1930s. These piles were initially constructed in loose soil. Jenkins and Henkel also conducted the first research on under-reamed piles in South Africa in 1949. Under-reamed piles are a type of bored pile that can have one or more bulbs based

*CORRESPONDING AUTHOR:
Ibrahim S. Harran, Faculty of Engineering, Tanta University, Tanta, Egypt; Email: Ibrahim_sabryh@f-eng.tanta.edu.eg

ARTICLE INFO
Received: 24 November 2022 | Revised: 14 December 2022 | Accepted: 19 December 2022 | Published Online: 31 January 2023
DOI: https://doi.org/10.30564/agger.v5i1.5276

CITATION
Nasr, A.M., Azzam, W.R., Harran, I.S., 2023. Geometrical Effect of Under-reamed Pile in Clay under Compression Load Numerical-Study. Advances in Geological and Geotechnical Engineering Research. 5(1): 1-9. DOI: https://doi.org/10.30564/agger.v5i1.5276

on a variety of parameters such as soil type, pile length, pile diameter, bulb number, bulb spacing, and bulb diameter. When two bulbs were used to study the influence of bulb number on a bearing load, the compression load increased by about 80% [1]. The bearing load of under-reamed piles in multi-layered soil is determined by pile length. The pile lengths used in the study were 3.5 m, 4.3 m, 5 m, 5.5 m, and 6 m, with the ANSYS program. According to the study, the bearing load of an under-reamed pile increases slightly as the pile length increases from 3.5 m to 6 m. According to a study on the bearing load's relationship with bulb diameter, the bearing load increased by 228.57% as the diameter of the bulb pile increased from 0.60 m to 1.20 m [2]. As bulb diameter increases, the area of soil sliding spreads up and beneath the bulb, influencing the pile's valid length of side friction. Consequently, the load of the pile's side friction is reduced [3]. PLAXIS 3D was used to investigate the effect of adding one or more bulbs to a stem pile on the bearing load and found that the bearing compression load was raised twice. According to studies for different pile lengths (6 m, 8 m, 10 m, and 12 m), as the pile length was increased, the bearing load of tapered piles increased dramatically, but the bearing load of under-reamed piles only increased marginally [4]. To numerically analyze under-reamed piles, use ANSYS piles exposed to axial load in tension and compression with changing geometrical factors such as bulb diameter, number, spacing, and position. They discovered that geometrical parameters had a considerable impact on the bearing load of under-reamed piles under tension and compression loads [5]. Bulb piles are regarded to have the most advantages over other piles since they can work successfully with smaller diameters and lengths. Instead of long, high-diameter piles, under-reamed loads and loads with several bulbs can be used to transfer large loads. Furthermore, soil conditions have a significant impact on the performance of under-reamed piles. under-reamed piles can also be installed in clay and sand soil to increase the bearing load of the pile foundation [6,7]. For determining the ultimate capacity of under-reamed piles, two techniques based on center-to-center bulb spacing were proposed [8]. Two methods for determining the ultimate carrying load were proposed. The first method considers shear resistance mobilized along the surface of the pile shaft further than the bulbs, shear resistance mobilized on the cylindrical surface circumscribing the bulbs, and end bearing at the pile toe. The second method considers the individual bearing resistance of each base as well as the frictional resistance mobilized along the pile shaft. The shearing resistance formed on the cylindrical surface around the bulb of many under-reamed drilled shafts has been considered [9]. The load transmission begins at the pile tip with bearings and then fails to owe to cylindrical shear failure [10]. To investigate the influence of the concrete casting method on under-reamed piles subjected to stress and compression, two groups of three under-reamed piles are used. The first group used self-compacting concrete, while the second group used conventionally vibrated cement concrete. under-reamed piles made of self-compacting concrete were proven to be more uniform and durable than piles made of regular concrete. The load-deformation behaviors of conventional concrete piles and self-compacting concrete piles were remarkably equivalent under tension and compression [11]. The under-reamed piles that have been constructed in Taihang Mountain, China, the project have a stem diameter of 0.7 m, a pile length of 32 m, a bulb diameter of 1.4 m, and two numbers of bulbs. The concrete grade used in the design is C40 for all piles [12]. under-reamed piles were used in the Eastern Expressway project in Ningbo, China. And they found that under-reamed piles can save over 30% in construction materials when compared to traditional straight piles with the same compressive bearing capacity [13].

2. Goals and objectives

The primary objective of this research is to investigate the effect of changes in the geotechnical properties and geometrical features of the under-reamed pile, such as pile length, bulb diameter, bulb spacing, and the number of bulbs, particularly bulb spacing, because previous studies focused on bulb diameter

and the number of bulbs, on bearing capacity and settlement in stiff clay. However, when the under-reamed pile was subjected to compression force, the bulb spacing had a significant role in defining the failure mechanism mode, whether cylindrical shear failure or individual shear failure. The finite element analysis approach (PLAXIS 3D) was utilized to determine the best parameters for high bearing capacity.

3. Numerical modeling and analyses

3.1 Numerical modeling

The finite element model of the under-reamed pile and the surrounding soil was constructed by the Plaxis 3D program. The under-reamed pile was simulated as a concrete volume element, and the linear elastic constitutive model was used to represent the pile. To describe the soil, the Mohr-Coulomb model (MC) was used. The main five input parameters for simulating clay soil by the Mohr-Coulomb model are the unit weight (γ); Young's modulus (Es); Poisson's ratio (u); Cohesion (c); and the interface ratio between the soil and the concrete surface of the pile (RInterface). To avoid any significant boundary effects, the overall dimensions of the model boundaries are a width of 40 times the pile's diameter and the model depth is equal to twice the pile length [14].

3.2 Model validation and verification

The PLAXIS 3D was used to validate the Tian et al. under-reamed pile experimental test. The experimental model was used to explore the bearing capacity and failure mechanisms around the pile, as well as to validate the use of half and whole steel pile cross-sections in future experiments. The Mohr-Column constitutive model was used to represent clay soil. For the pile, however, a linear elastic model was adopted. The following pile geometric attributes were used in the experimental model: 210 mm under-reamed pile length (L), 10 mm stem pile diameter (D), 30 mm bulb diameter (Du), and two bulbs (N). **Table 1** shows the pile and soil parameters (1). The numerical model dimensions used are equal to the tank dimensions, the width, length, and height of 400 mm × 400 mm × 400 mm [15]. The comparison of the results of the experimental model published by Tian et al. (2016) and the numerical model in the present study analyzed by PLAXIS 3D is shown in **Figure 1**.

Table 1. Properties of pile and clay soil, Tian et al. (2016).

Parameter	Clay	Steel pile	Unit
Model type	MC	LE	-
Drainage type	Undrained	-	-
Soil saturated unit weight (γ_{sat})	18.6	78.5	kN/m^3
Young's modulus (E)	2.5E + 05	21E + 07	kN/m^2
Poisson's ratio (υ)	0.35	0.2	-
Cohesion (c)	59	-	kN/m²
Interface reduction factor (R)	0.5	-	-

The load settlement relationships of the numerical model match well with those of the experimental model. The differences in results between experimental and numerical analysis (using PLAXIS 3D) range from 2.5% to 10%. As a result, the outcomes of the numerical models were used to match the trend of the lab data, achieving good conformity. Its results showed that the Plaxis 3D version is capable of predicting the actions of the under-reamed pile under axial load in clay led to the proposal to use the computer program for the analyses suggested in this technical article.

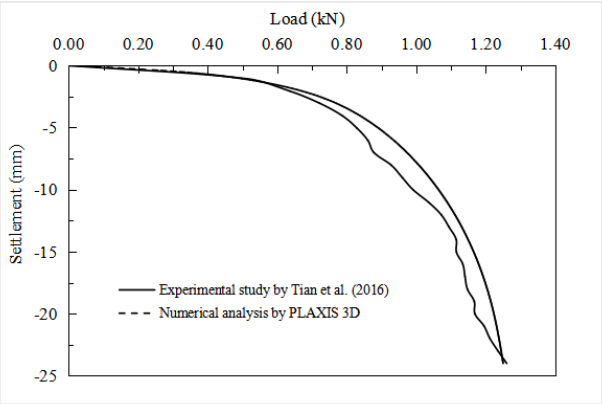

Figure 1. Comparison of the model test result by Tian et al. (2016) and the numerical analysis by PLAXIS 3D.

3.3 Characteristics and meshes of the numerical model

PLAXIS 3D uses a full-scale numerical model to investigate the effect of various geotechnical and geometrical parameters on the bearing load of an under-reamed pile. The first bulb was regarded by all groups at a bucket distance of one meter from the bottom of the under-reamed pile. The global coarseness of meshing was set to fine to provide decent results without compromising analysis time. **Figure 2** illustrates the mesh form of the under-reamed pile after meshing. The under-reamed pile was modeled in two stages. First, the gravity load was applied to the soil block to account for the initial in-situ stress states. After the specified displacement has been applied to the pile head, the pile geometry and properties are defined in the second stage. Given the geometry of the load-displacement curve, a proper point of ultimate shear failure is possibly not the best choice. They calculated the ultimate bearing load of under-reamed piles using the Indian Standards settlement criterion [5,16]. They advocated the adoption of settlement criteria in such cases [3,17].

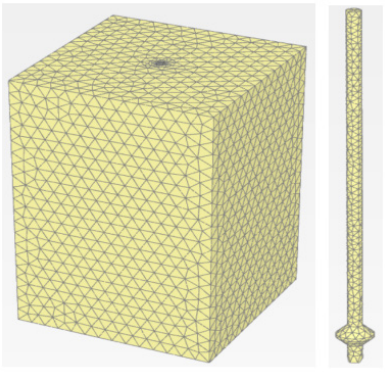

Figure 2. Meshing of under-reamed pile, (a) soil block, (b) under-reamed pile with one bulb.

3.4 Geometry and material properties

The typical under-reamed pile details are shown in **Figure 3**. The soil condition used in this study was stiff clay as shown in **Table 2**, and the groundwater table was 1 m below the ground surface. The characteristics of the under-reamed pile include the pile length (L), the stem pile diameter (D), the bulb diameter (Du), the bulb number (N), the bucket length (B) and the bulb spacing (S) as shown in **Figure 3**. **Table 3** shows the parameters used in the study.

Table 2. Properties of pile and clay soil.

Identification	Stiff clay	Concrete pile	Units
Model type	MC	LE	-
Drainage type	Undrained	-	-
Soil saturated unit weight (γ_{sat})	16	24	kN/m^3
Young's modulus (E)	12.8×10^3	2.6×10^7	kN/m²
Poisson's ratio (ν)	0.35	0.2	nu
Cohesion (c_u)	75	-	kN/m²
Interface reduction factor (R)	0.7	-	-

Table 3. Variables and ranges used in the parametric study.

Case	Variable	Studied parameters
Pile length	L/D	30
Bulb diameter ratio	Du/D	1.5, 2, 2.25 and 2.5
Number of bulbs	N	1, 2 and 3
Bulbs spacing	S/D	2, 3, 4, 5, 6, 7, and 8

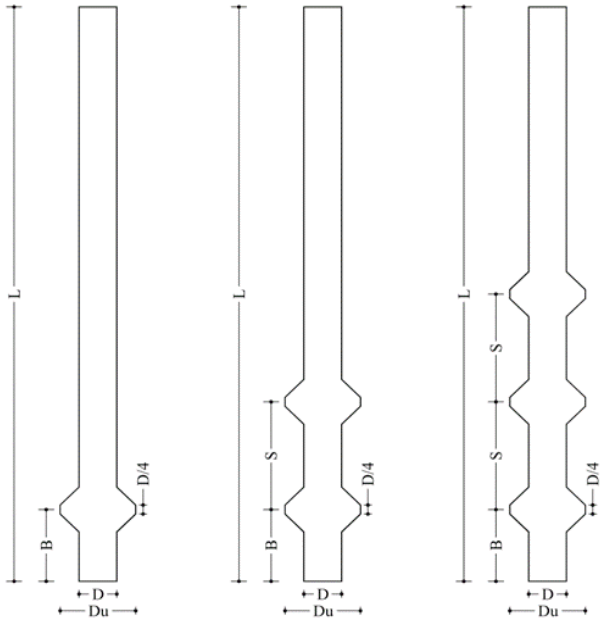

Figure 3. Typical under-reamed pile geometrical features.

3.5 Results and discussion

Figure 4 presents the load-settlement relation-

ship for an under-reamed pile with a single bulb in stiff clay, pile length to diameter ratio L/D = 30 and bulb diameter ratios (D_u/D = 1.5, 2, 2.25, and 2.5). As the bulb diameter increases, the under-reamed pile load capacity increases significantly, resulting in reduced settlement. The corresponding capacities are (1901, 2166, 2498, and 2530) kN for single bulb under-reamed pile at (D_u/D) ratios of (1.5, 2, 2.25 and 2.5) respectively. While the bearing capacity is reduced to 1775 kN for a pile without a bulb. It is noticed that the load-settlement curve is improved and modified according to bulb diameter. For the single bulb under-reamed pile with different bulb diameter ratios (D_u/D) and (L/D = 30) at the same bearing load of 1700 kN, the settlement values are (28 mm, 21 mm, 17 mm, and 17 mm) for (Du/D) ratios (1.5, 2, 2.25, and 2.5) respectively, while the settlement of the pile without a bulb at this load is 40 mm. This indicates that the bearing capacity of an under-reamed pile with a large bulb diameter provides slight displacements and could be more acceptable for a supporting structure. It was also observed that the initial linear slope of the load-displacement curves of the under-reamed pile with different bulb diameters was almost the same with an increase in bulb diameter. It is obvious that the carrying capacity increases by (7%, 22%, 41%, and 43%) for (Du/D) ratios (1.5, 2, 2.25, and 2.5). The presence of a bulb alters and enhances the load-settling behavior of an under-reamed pile, as well as the bearing capacity in relation to pile depth of embedment and clay soil cohesiveness. The increase in bearing load occurs due to adding a bulb to the shaft which leads to an increase in the projected bearing area [12].

While, **Figure 5** presents the load-settlement relationship for an under-reamed pile with one, two, and three bulbs in stiff clay, pile length to diameter ratio (L/D) = 30, and bulb diameter ratio (Du/D = 2.5), the corresponding capacities are (2452, 3013 and 3370) kN for bulbs number (N = 1, 2, and 3) respectively. While the bearing capacity is reduced to 1775 kN for a pile without a bulb. As the bulb number increases, the under-reamed pile load capacity increases, resulting in reduced settlement. For the under-reamed pile with different bulb numbers (N) and (L/D = 30) at the same bearing load of 1700 kN, the settlement values are (16 mm, 13 mm, and 13 mm) for bulbs number (N) (1, 2, and 3) respectively, while the settlement of the pile without a bulb at this load is 40 mm. It is obvious that the carrying capacity increases by (38%, 70%, and 90%) for (N) ratios (1, 2, and 3). It can be seen that the existence of such a bulb with a sufficient number can significantly improve the pile capacity and decrease the settlement. The increase in bearing load occurs due to adding a bulb to the shaft, which leads to an increase in the projected bearing area [12].

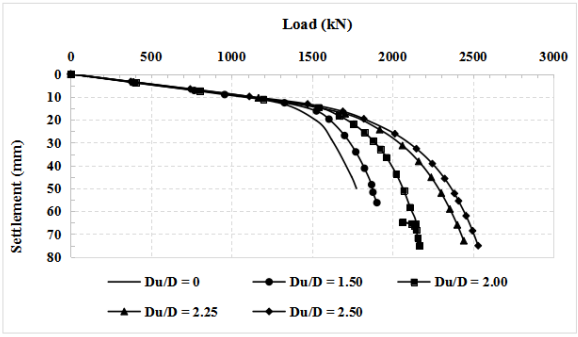

Figure 4. Load settlement relationship for under-reamed pile for (N = 1), in stiff clay, pile length to diameter ratio (L/D = 30), in different bulb diameter ratios.

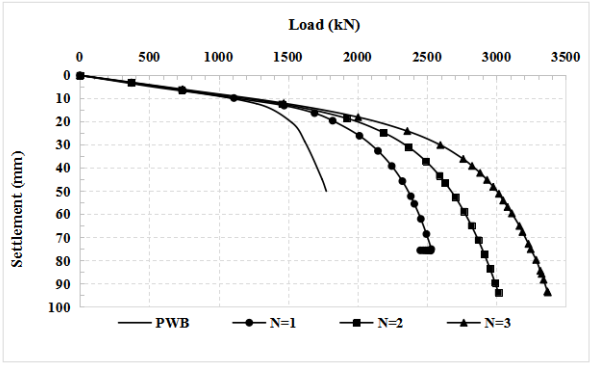

Figure 5. Load settlement relationship for under-reamed pile for (D_u/D = 2.5), in stiff clay, pile length to diameter ratio (L/D = 30), in different bulb numbers.

However, **Figure 6** presents the load-settlement relationship for an under-reamed pile with a number of bulbs (N = 2) in stiff clay, pile length to diameter ratio L/D = 30 and bulb diameter ratios (Du/D = 2). It is noticed that Increased soil cohesion leads to increased under-reamed pile-bearing capacity

due to increased shaft frictional resistance and total bull-bearing load. With the increase in bulb spacing, the ultimate bearing load significantly increases and the settlement is reduced. The corresponding capacities are (2470, 2455, 2687, 2731, 2804, 2824, and 2945) kN for bulb spacing (S/D) ratios of (2, 3, 4, 5, 6, 7, and 8) respectively. While the bearing capacity is reduced to 1775 kN for a pile without a bulb. For the bulb spacings of the under-reamed pile (S/D) and (L/D = 30) at the same bearing load of 1700 kN, gives the same settlement value (18 mm) for (S/D) ratios (2, 3, 4, 5, 6, 7, and 8) respectively, while the settlement of the pile without a bulb at this load is 39 mm, it demonstrates that the settlement value is the same for under-reamed piles with various spacing ratios under compression loading. The previous analysis shows that the bulb spacing ratio of the under-reamed pile had no influence on the initial linearly elastic slope of the load-displacement curves [14]. It is obvious that the carrying capacity increases by (39%, 38%, 51%, 54%, 58%, 59%, and 66%) for (S/D) ratios (2, 3, 4, 5, 6, 7, and 8). It can be seen that the increased soil cohesion and change of bulb spacing improve the pile capacity and decrease the settlement, but failure occurs at spacing S/D = 3 before reaching the proposed settlement. When the spacing between bulbs becomes small, the confined volume of soil between the bulbs is mobilized, and the bulbs work together and act as a semi-rigid body that develops a cylindrical shear surface [15]. But when the spacing between the bulbs is large, the overall bearing load of under-reamed pile under vertical load is the combination of individual bulb capacities and the side friction resistance along the pile length [18].

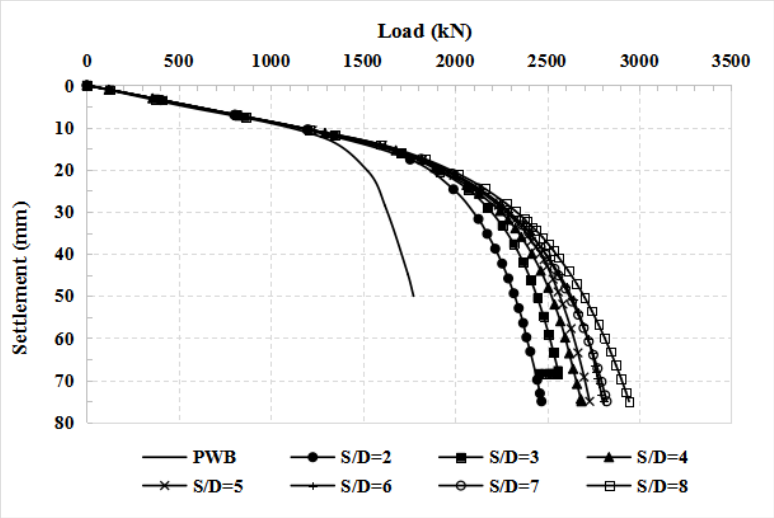

Figure 6. Load settlement relationship for under-reamed pile for (N = 2), in stiff clay, (L/D = 30) and (Du/D = 2), in different bulb spacings (S/D).

However, **Figure 7** presents the load-settlement relationship for an under-reamed pile with a number of bulbs (N = 3) in stiff clay, pile length to diameter ratio L/D = 30 and bulb diameter ratios (Du/D = 2). Increases the number of bulbs, increase soil cohesion and increases bulb spacing, the ultimate bearing load significantly increases and the settlement is reduced. The corresponding capacities are (2791, 2975, 3128, 3294, 3427, 3506, and 3535) kN for bulb spacing (S/D) ratios of (2, 3, 4, 5, 6, 7, and 8) respectively. While the bearing capacity is reduced to 1775 kN for a pile without a bulb. It is noticed that with the increase of bulb spacing, the ultimate bearing capacity improves and the settlement is reduced. For the bulb spacings of the under-reamed pile (S/D) and (L/D = 30) at the same bearing load of 1700 kN, gives the same settlement value (17 mm) for (S/D) ratios (2, 3, 4, 5, 6, 7, and 8) respectively, while the settlement of the pile without a bulb at this load is 39 mm, it demonstrates that the settlement value is the

same regardless of the under-reamed pile's bearing capability at various spacing ratios under compression force. According to the earlier investigation, the under-reamed pile's bulb spacing ratio had no impact on the load-displacement curves' initial linearly elastic slope [14]. It is obvious that the carrying capacity increases by (57%, 68%, 76%, 86%, 93%, 98%, and 99%) for (S/D) ratios (2, 3, 4, 5, 6, 7, and 8). It can be seen that the change of bulb spacing with spacing can significantly improve the pile capacity and decrease the settlement but failure occurs at spacing (S/D = 3, 4, 6, and 7) before reaching the proposed settlement.

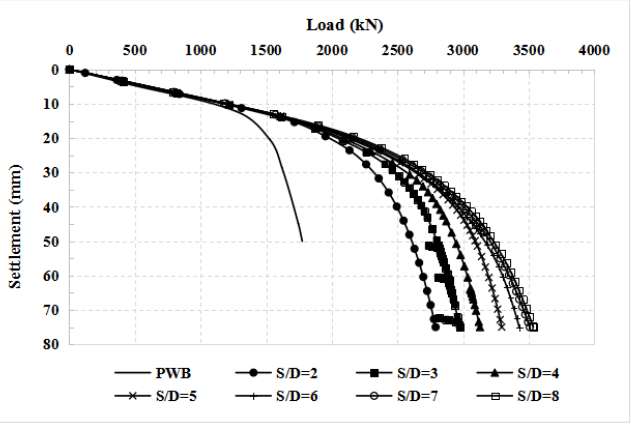

Figure 7. Load settlement relationship for under-reamed pile for (N = 3), in stiff clay, (L/D = 30) and (Du/D = 2), in different bulb spacings (S/D).

4. Conclusions

• As bulb diameter increases, the increase in bearing load occurs due to adding a bulb to the pile shaft that leads to an increase in the projected bearing area.

• As a bulb number increases, the under-reamed pile load capacity increases significantly and the settlement is reduced.

• It's important to study the effect of bulb spacing on the bearing capacity of an under-reamed pile with different bulb spacings (S/D), because the bulb spacing determines the mode of failure mechanism under compression loading.

Conflict of Interest

There is no conflict of interest.

References

[1] George, B.E., Hari, G. (editors), 2015. Numerical investigation of under-reamed piles finite element analysis was carried out using. Sixth International Geotechnical Symposium 6 IGS Chennai, India. p. 4-7.

[2] Pakrashi, S., 2017. A comparative study on safe pile capacity as shown in table 1 of IS 2911 (Part III): 1980. Journal of The Institution of Engineers (India): Series A. 98(1-2), 185-199. DOI: https://doi.org/10.1007/s40030-017-0189-z

[3] Terzaghi, K., 1942. Discussion of the progress report of the committee on the bearing value of pile foundations. Proceedings of the American Society of Civil Engineers. 68, 311-323.

[4] Vali, R., Mehrinejad-Khotbehsara, E., Saberian, M., et al., 2019. A three-dimensional numerical comparison of bearing capacity and settlement of tapered and under-reamed piles. International Journal of Geotechnical Engineering. 13(3), 236-248. DOI: https://doi.org/10.1080/19386362.2017.1336586

[5] Kurian, N.P., Srilakshmi, G. (editors), 2004. Studies on the geometrical features of under-reamed piles by the finite element method. Proceedings of International e-Conference on 'Modern Trends in Foundation engineering: Geotechnical Challenges and Solutions, Madras; 2004 Jan. p. 14.

[6] Golait, Y.S., Satyanarayana, V., Raju, S. (editors), 2009. Concept of under-reamed cemented stone columns for soft clay ground improvement. GeoTide. Guntur, Indian Geotechnical Society, IGC. New Delhi: Allied Publishers New Delhi. p. 356-360.

[7] Alielahi, H., Mardani, Z., Daneshvar, S., 2014.

Arrangement optimization of asymmetric under-reamed pile groups in order to evaluate tensile bearing capacity using numerical model. 8th National Congress on Civil Engineering; 2014 May 7-8; Babol, Iran. Babol: Babol Noshirvani University of Technology.

[8] Mohan, D., Murthy, V.N.S., Jain, G.S., 1969. Design and construction of multi-under-reamed piles. Proceedings the Seventh International Conference on Soil Mechanics and Foundation Engineering, Session 2, Mexico. Mexico: Mexico City. pp. 183.

[9] Martin, R.E., DeStephen, R.A., 2019. Large diameter double under-reamed drilled shafts. Journal of Geotechnical Engineering. 109(8), 1082-1098. DOI: https://doi.org/10.1061/(ASCE)0733-9410(1983)109:8(1082)

[10] Jain, G.S., Gupta, S.P., 1972. Deformation of soil around a multi under-reamed pile. Indian Concrete Journal. 46(6), 239-241.

[11] Peter, J.A., Lakshmanan, N., Manoharan, P.D., 2006. Investigation on static behavior of self compacting concrete under-reamed piles. Journal of Materials in Civil Engineering. 18(3), 408-414. DOI: https://doi.org/10.1061/(ASCE)0899-156118:3(408)

[12] Majumder, M., Chakraborty, D., Kumawat, V., 2022. Model test study on single and group under-reamed piles in sand under compression and tension. Innovative Infrastructure Solutions. 7, 129. DOI: https://doi.org/10.1007/s41062-021-00725-4

[13] Yuan, L., Dai, G., Gong, W., 2014. Experimental investigation, calculation and analysis of compressive bearing capacity of squeezed branch piles. Hans Journal of Civil Engineering. 3, 103e9.

[14] Tian, W., Qian, Y., Lu, T., et al., 2016. The undisturbed soil experiment of the comparison about the failure of the half and whole cross-section piles under the resistance compression. International Forum on Energy, Environment & Sustainable Development. 75, 296-300. DOI: https://doi.org/10.2991/ifeesd-16.2016.51

[15] Zhang, M., Xu, P., Cui, W., et al., 2018. Bearing behavior and failure mechanism of squeezed branch piles. Journal of Rock Mechanics and Geotechnical Engineering. 10(5), 935-946. DOI: https://doi.org/ 10.1016/j.jrmge.2017.12.010

[16] IS:2911, 1980. Indian standard code of practice for design and construction of pile foundations. Part III: Under-reamed piles (first revision). Soil and Foundation Engineering. New Delhi: Bureau of Indian Standards.

[17] No, P., 1990. Drilled shafts: Construction procedures and design methods. Tunnelling & Underground Space Technology. 5(1-2), 156-157. DOI: https://doi.org/10.1016/0886-7798(90)90101-o

[18] Qian, Y., Yi, Y., Wang, R., 2013. Research on influence factors of the ultimate bearing capacity of the soil of push-extend multi-under-reamed pile under compression. Advances in Materials Research. 671-674, 538-541. DOI: https://doi.org/10.4028/www.scientific.net/AMR.671-674.538

[19] Xie, X., Yin, X., 2012. The finite element analysis of plate's distance on push-extend multi-under-reamed pile. Advances in Materials Research. 468-471, 2517-2520. DOI: https://doi.org/10.4028/www.scientific.net/AMR.468-471.2517

[20] Qian, Y.M., Shan, L.J., Xu, G.H., 2014. Testing research on the shape of the bearing push-extend reamed affecting the bearing capability of the pile of push-extend multi-under-reamed pile. Advances in Materials Research. 962-965, 1091-1094. DOI: https://doi.org/10.4028/www.scientific.net/AMR.962-965.1091

[21] George, B., Hari, G., Alexander, C., 2022. Investigation on multi under-reamed piles with small bulb diameter in clay. International Journal of Geotechnical Engineering. 16(4), 462-470. DOI: https://doi.org/10.1080/19386362.2021.1959010

[22] Peter, J.A., Lakshmanan, N., Devadas Manoha-

ran, P., 2006. Investigations on the Static Behavior of Self-Compacting Concrete Under-Reamed Piles. Journal of Materials in Civil Engineering. 18(3), 408-414.
DOI: https://doi.org/10.1061/(asce)0899-156118:3(408)

[23] Qian, Y.M., Liu, X.L., Wang, R.Z., 2013. Research on the formula of the height of bearing push-extend under-reamed of the push-extend multi-under-reamed pile. Advances in Materials Research. 694(697), 883-886.
DOI: https://doi.org/10.4028/www.scientific.net/AMR.694-697.883

[24] Qian, Y.M., Zhai, R.Z., Liu, X.L., 2014. Testing research is about the influence of the diameter of the bearing push-extend reamed to the bearing capability of the pile of push-extend multi-under-reamed pile. Applied Mechanics and Materials. 578-579, 192-195.
DOI: https://doi.org/10.4028/www.scientific.net/AMM.578-579.192

[25] Qian, Y.M., Zhao, D.P., Xie, X.W., 2014. The research on the ultimate bearing capacity of soil around the push-extend multi-under-reamed pile at sliding failure state. Applied Mechanics and Materials. 578-579, 232-235.
DOI: https://doi.org/10.4028/www.scientific.net/AMM.578-579.232

[26] Qian, Y., Chen, X., Xie, X., 2014. Determine the stress calculating mode of sliding failure of soil mass under the push-extend multi-under-reamed pile. Engineering. 6(5), 254-259.
DOI: https://doi.org/10.4236/Eng.2014.65029

[27] Qian, Y., Xu, G., Wang, R., 2013. Experimental research on failure behavior of soil around pile under compression. Telkomnika Indonesian Journal of Electrical Engineering. 11(4), 23-77.
DOI: https://doi.org/10.11591/telkomnika

[28] Qian, Y.M., Yu, H., Wang, R.Z., 2013. Analyzing bearing capacity influence due to location of bearing push-extend reamed of the push-extend multi-under-reamed pile. Advanced Materials Research. 690(693), 1891-1894.
DOI: https://doi.org/10.4028/www.scientific.net/AMR.690-693.1891

[29] Shrivastava, N., Bhatia, N., 2008. Ultimate bearing capacity of under-reamed pile—Finite element approach. 12th International Conference on Computer Methods and Advances in Geomechanics. 5, 3490-3497.

[30] Liu, Y., Liu, H., Lin, D., 2011. Based on FEM in analysis of the performance of under-reamed pile expansion of the bottom. PACCS 2011 2011 3rd Pacific-Asia Conference Circuits, Communications & System; 2011 Jul 17-18; Wuhan,China. USA: IEEE. p. 5-8.
DOI: https://doi.org/10.1109/PACCS.2011.5990151

BILINGUAL PUBLISHING GROUP
Pioneer of Global Academics Since 1984

Advances in Geological and Geotechnical Engineering Research
https://journals.bilpubgroup.com/index.php/agger

ARTICLE

Study on Epithermal Gold Mineralization System at Shwebontha Prospect, Monywa Copper-Gold Ore Field, Central Myanmar

***Toe Naing Oo*[1,2*], *Agung Harijoko*[1], *Lucas Donny Setijadji*[1]**

[1] *Department of Geological Engineering, Faculty of Engineering, Gadjah Mada University, Yogyakarta, 55281, Indonesia*

[2] *Department of Geology, West Yangon University, Yangon, 11181, Myanmar*

ABSTRACT

The Shwebontha prospect area is situated in the Central Volcanic Belt, central Myanmar, where the well-known Sagaing Fault serves as its eastern boundary. This study aims to document key the mineralogy, host rock geochemistry and ore mineralizing fluids. The mineralization, hosted by Upper Oligocene to Middle Miocene rhyolites, displays a strong lithological control. Mineralization is characterized by gold-bearing silicified massive ore and chalcedonic quartz veins in which sulfides are clustered and disseminated not only in quartz gangue but also in rhyolite host rocks. The significant ore minerals in the mineralized veins include pyrite, sphalerite, galena, chalcopyrite, and gold. Common hydrothermal alterations such as silicic, argillic and propylitic alteration types are recognized. According to the fluid inclusion data and interpretation, ore mineralizing fluids in the research area are characterized by formation temperatures of 260-280 °C and salinity of 0.35-2.41 % wt. NaCl eq. respectively. Mixing of hydrothermal fluids was generally considered to be an effective mechanism for ore transport and deposition.

Keywords: Geochemistry; Alteration; Fluid inclusions; Ore mineralization; Central Volcanic Belt; Shwebontha

1. Introduction

The Monywa copper-gold ore field is one of the largest endowed areas in entire Southeast Asia. It is located within the western part of the well-known

*CORRESPONDING AUTHOR:
Toe Naing Oo, Department of Geological Engineering, Faculty of Engineering, Gadjah Mada University, Yogyakarta, 55281, Indonesia; Department of Geology, West Yangon University, Yangon, 11181, Myanmar; Email: toenaingoo.geol84@gmail.com

ARTICLE INFO
Received: 2 November 2022 | Revised: 30 December 2022 | Accepted: 6 January 2023 | Published Online: 9 February 2023
DOI: https://doi.org/10.30564/agger.v5i1.5230

CITATION
Oo, T.N., Harijoko, A., Setijadji, L.D., 2023. Study on Epithermal Gold Mineralization System at Shwebontha Prospect, Monywa Copper-Gold Ore Field, Central Myanmar. Advances in Geological and Geotechnical Engineering Research. 5(1): 10-23. DOI: https://doi.org/10.30564/agger.v5i1.5230

Sagaing Fault in the Central Volcanic Belt, Central Myanmar (**Figure 1**) [1-3]. The field hosts four distinct high sulfidation copper ore deposits including Letpadaung taung, Kyisintaung, Sebataung, Sebetaung South and other small gold prospects Kyaukmyet, Shwebontha, Taungzone, Myeik respectively. The Shwebontha prospect is located about one kilometre ENE of the Letpadaung taung Cu-Au deposit in which operating mining [3]. Tectonically, this research area is a part of Central Volcanic Belt (**Figure 1**), which is one of the prominent geological aspects and multistage metallogeny in Myanmar. Generally, the belt hosts several porphyry-related skarn deposits and epithermal gold-copper deposits, epithermal gold-silver deposits, base metal deposits and mesothermal gold deposits. Mineral exploration especially targeting precious and base metal deposits in the research area, Monywa copper-gold ore field was carried out by Ivan Hold Copper Company Limited in 1995. Based on a resource estimate by Htet [4] (unpublished data), the maximum gold grade contains 3 g/t to 10.4 g/t. In addition, the concentration of base metals containing Cu (12.45 ppm), Pb (105.43 ppm), Zn (392.96 ppm), As (115.92 ppm), and Sb (5.299 ppm) in the drill core analysis [4] (unpublished data). This paper aims to document the geological, alteration, and mineralization characteristics of the Shwebontha prospect, Monywa copper-gold ore field, one of the well-known epithermal deposits in the Monywa copper-gold ore field. This presents a description of the associated host rocks and hydrothermal alteration mineral assemblages, the ore mineral assemblages, mineralization characteristics and the characteristics and ore-forming processes of the hydrothermal system. This research also reveals the conceptual model for the development of the epithermal system in the Shwebontha prospect, Monywa copper-gold ore field.

2. Geological background and setting

Myanmar lies in a tectonic setting covering several metallogenic belts, with a high prospective for the occurrence of economic gold-copper deposits. Several ore deposits have been generated as world-class mines in the last decades [5,6]. In general, there are numerous metallogenic belts in Myanmar that have great potential for economic gold and copper mineralization, tin-tungsten and lead zinc silver deposit (**Figure 1**). These many metallogenic belts were formed during specific metallogenic epochs during the Phanerozoic [7] and related to long-lived subduction that formed during Late Mesozoic and Cenozoic [8,9]. Most of the copper and gold deposits are occurred within the Central Volcanic Belt (CVB) also known as Wuntho Popa Magmatic Arc (WPMA) at the western portion of the renowned Sagaing Fault [10] (**Figure 1**) in Myanmar and are concentrated in the Monywa copper-gold ore field, Kyaukpahto, and Wuntho-Massif regions. Accordingly, the major Sagaing Fault [11] is still an energetic, deep-seated, N-S trending, right-lateral strike-slip fault, which extends over 1500 km across the country (**Figure 1**). As a result of this structural constraint, the right-lateral strike-slip fault is considered to be critical geologic control of the ore mineralization in the Central Volcanic Belt.

According to the geological background, the Central Volcanic Belt is recognized by the presence of Mesozoic age intrusive and volcanic rocks and Cretaceous-Pliocene sedimentary formations. Meanwhile, the Central Volcanic Belt is composed mainly of Upper Cretaceous to Tertiary granodioritic intrusive rocks, and with a minor part of volcanic rocks of Upper Cretaceous to Quaternary ages [1,5,9]. The Monywa copper-gold ore field is located in the Central Volcanic Belt, within the middle portion of Myanmar [1,5,8] (**Figure 1**). In the Monywa copper-gold ore field, Mesozoic volcanic rocks are mainly intruded by the Upper Cretaceous age of granodiorites [1]. Based on the previous research [1,2,4] the Monywa copper-gold ore field of high-sulfidation (HS) copper-gold deposit and low-sulfidation (LS) gold-silver deposit and base metal deposits in the Monywa copper-gold ore field are intimately related to basement rocks and granitic intrusions. Generally, the basement rocks are extensively distributed by volcanic rocks such as andesite, quartz andesite porphyry, dacite, and rhyolite in the Magyigon Formation (**Figure 2**). Most copper-gold (high-sulfidation type) and gold-silver (low-sulfidation type) and base metal deposits between the Chindwin River and Powintaung are mainly formed by the Upper Oligocene to Middle Miocene Magyigon Formation (**Figure 2**).

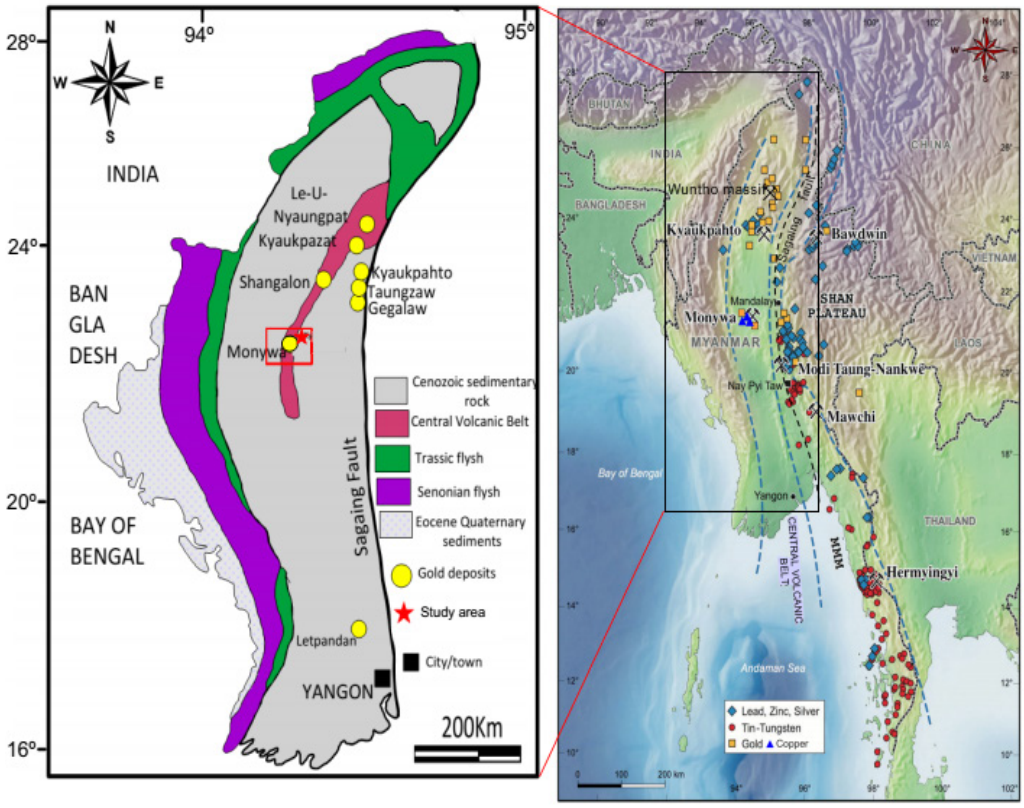

Figure 1. Map showing Central Volcanic Belt (CVB) with major gold deposits of copper-gold and lead-zin, tin-tungsten (right side). Map illustrating the generalized distribution of primary gold deposits from sub-units of CVB (left side) [7,13].

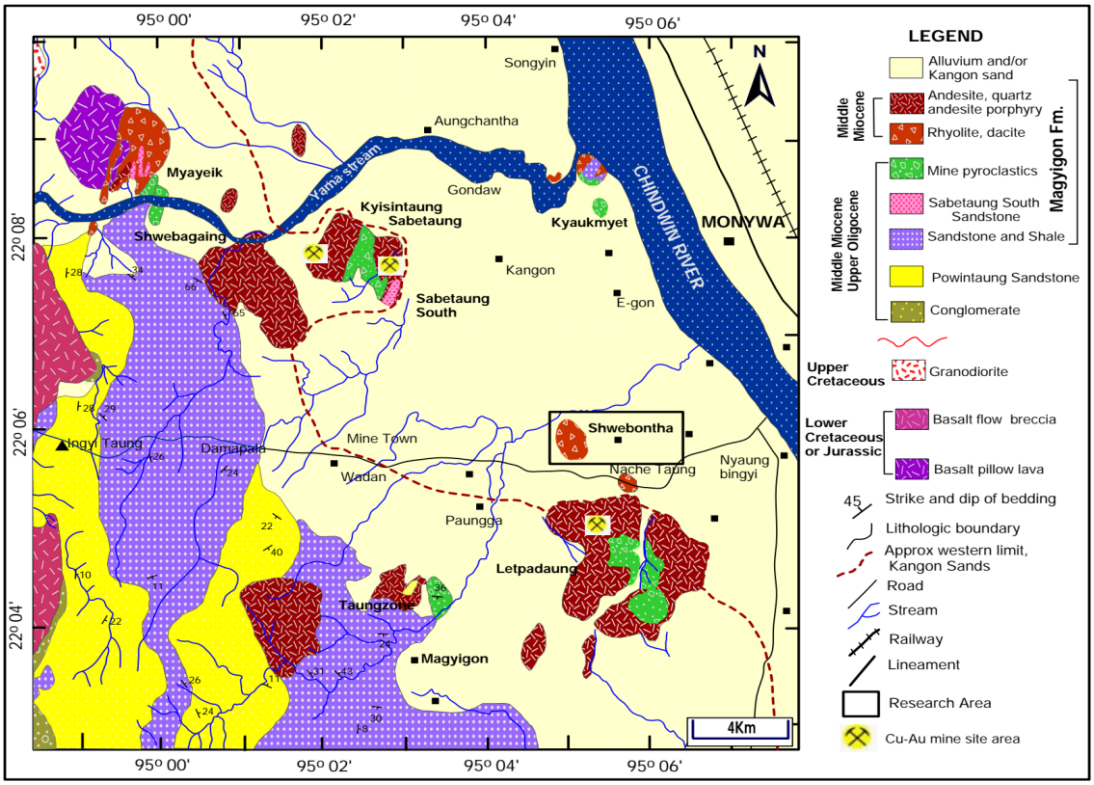

Figure 2. Regional geological map of Monywa copper-gold ore field (Modified after [1]).

3. Local geology

The Shwebontha prospect belongs to the epithermal gold-based metal mineralization [3]. It is located about one-kilometer ENE of the Letpadaung Cu-Au deposit in which active mining (**Figure 2**). The geology of the prospect area (Monywa copper-gold ore field) is described by Oo, T.N., Harijoko. A., Setijadji, L.D, 2021 and Htet, 2008. It is dominated by Upper Oligocene to Middle Miocene stratigraphic unit, named the Magyigon Formation, which consists mainly of rhyolite, hydrothermal breccia, tuff breccia, tuff, tuffaceous sandstone and alluvium deposit (**Figure 3**). In the prospect area, a simplified geological map points out the presence of rhyolite as the major rock unit at the eastern and northern parts of the Shwebontha prospect. Stratigraphically, hydrothermal breccia is the oldest rock unit. Gold-based metal mineralization mainly occurs in the rhyolite belonging to the Central Volcanic Belt in the study area. Mineralization is recognized by gold-bearing silicified massive ore and chalcedonic quartz veins in which sulfides are clustered and disseminated in the rhyolite host rocks. This mineralization vein is intimately associated with a silicic alteration zone characterized by the presence of pyrite, galena, sphalerite, chalcopyrite and gold. Their vein trends generally followed the regional structural trend, which might be related to NE-ENE trending in a direction that is probably considered to be responsible for the formation of epithermal gold-base metal mineralization in the Shwebontha prospect [3].

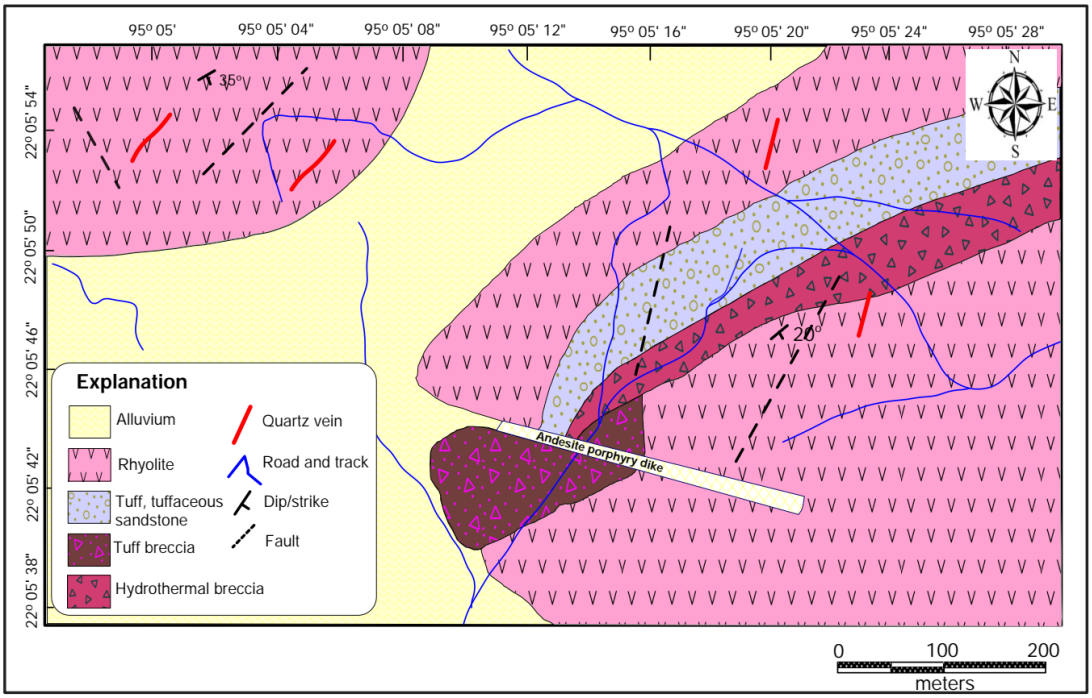

Figure 3. Simplified geological map of the Shwebontha prospect (modified after [4]).

4. Research methods

Methods employed in this study were petrography, X-ray Fluorescence (XRF) and fluid inclusion micro thermometry. A total of twenty-five (25) samples were collected from the surface outcrops in the Shwebontha prospect area, Monywa copper-gold ore field: hydrothermally altered rock (15 samples) and mineralized quartz vein (10 samples). Fifteen samples were prepared for thin sections, doubly-polished thin sections, or polished sections. Thin sections and polished sections were determined petrographically to identify the primary and secondary (alteration) mineral assemblages. A detailed study on ore microscopy of polished thin sections using both transmitted and reflected light was done to observe

ore mineral assemblages and textural relationships. Subsequently, a total of 12 representative rock samples were selected for whole-rock geochemistry. The concentrations of major and minor elements of 12 rhyolite rocks were analyzed by X-ray Fluorescence (XRF). On the contrary, five mineralized quartz vein samples were further analyzed by fluid inclusion analysis. The fluid inclusion mico thermometry was performed to obtain information data regarding the temperatures of ore formation and the salinities of mineralizing fluids. Salinities, which are expressed in wt.% NaCl equivalent, were examined from the last ice-melting temperatures using the equation of Bodnar (1993) [14]. All laboratory analyses were undertaken at Kyushu University, Japan.

5. Results and discussion

5.1 Geochemistry of volcanic rock

The volcanic rocks from the Shwebontha prospect mainly constitute rhyolite. The concentration of major (wt%), trace and rare earth elements (ppm) of the rhyolite rocks from the Shwebontha prospect are displayed in (See **Appendix A**). The rhyolite rocks show the SiO_2 contents ranged between (75.1%-79.98%), Al_2O_3 (9.11%-12.75%), FeO*(tot) (0.08%-1.22%), TiO_2 (0.8%-0.10%), MnO (0%-0.1%), MgO (0.44%-0.7%), CaO (0.14%-0.21%), Na_2O (0.50%-0.88%), and K_2O (6.43%-9.73%) (See **Appendix A**). Based on the plotting result in the TAS (Total Alkali versus Silica) diagram of [15] **(Figure 3**) can be confirmed that this unit consists of rhyolite. Volcanic rock compositions were also confirmed by an immobile trace elemental plot (**Figure 4**) by applying Zr/Ti and Nb/Y diagram [16].

Based on the binary plot diagram of SiO_2 versus Na_2O+K_2O [17], volcanic rocks (rhyolites) of the Shwebontha prospect area have displayed the nature of sub-alkaline to alkaline affinity (**Figure 5**). AFM diagram is classified between tholeiitic and calc alkaline differentiation trends in the sub-alkaline magma series. Volcanic rocks (rhyolite) from the Shwebontha prospect are plotted on the AFM diagrams [17]. Triangular AFM plot shows that the rocks are located in the field of the calc-alkaline series (**Figure 5**). The triangular AFM plot shows that the rocks are located in the field of the calc-alkaline series (**Figure 5**). The SiO_2 and some of the major oxide elements cannot be applied because of alteration product in the magmatic evolution processes. For this reason, the incompatible element 'Zr' is used as a replacement for SiO_2. The trace element variation diagram in this study exhibits that Rb, Nb, Ba, Sr and Y versus Zr display positive correlation (**Figure 6**) which are recognized to be mobile with altered volcanic (rhyolite) rock during hydrothermal alteration.

5.2 Hydrothermal Alteration

Mineralization and hydrothermal alteration are observed in the rhyolite host rock unit. Alteration developed around open space mineralized veins at breccia zones. In the research area, three principal kinds of hydrothermal alteration zones have evolved including silicic, argillic and propylitic alteration types. They are examined by optical petrographic observations (**Figure 7**).

Silicification is also a common type of hydrothermal alteration in the Shwebontha propsect, and is closely related to ore mineralization. Silicified rock is characterized by equigranular microcrystalline quartz, hematite and sulfide minerals (**Figure 7**). This alteration is represented by chalcedony, disseminated pyrite with medium to coarse-grained quartz and quartz veinlets in the brecciated sulfide quartz vein and chalcedonic quartz vein (**Figure 7**). And, it also occurs as mineralized veins and is associated with breccias blocks of cement, vein-veinlet and stockwork (up to 2-3 cm width) quartz veins (**Figure 7**). Argillic alteration is characterized by a variable amount of quartz, plagioclase, opaque minerals and clay minerals (sericite, illite, illite/smeciite, and kaolinite). Anhedral to subhedral quartz is found as a phenocryst and fine-grained groundmass (**Figure 7**). Opaque minerals (pyrite) have occurred dissemination (**Figure 7**) which is associated with clay minerals (illite, smectite and quartz). Altered plagioclase was replaced by the yellowish-brown colour

of sericite and kaolinite (**Figure 7**). In addition, plagioclase phenocrysts and groundmass were partially replaced by illite, illite/smectite mixed layer mineral, pyrite and quartz minerals. Secondary quartz mainly replaced the groundmass or matrix of the rhyolites (**Figure 7**). According to the microscopic study, the common propylitic alteration minerals are quartz, chlorite, epidote and pyrite (**Figure 7**). The presence of chlorite and epidote can be recorded in the alteration type as propylitic alteration. Altered plagioclase was replaced by quartz, chlorite, epidote, and some clay minerals (**Figure 7**).

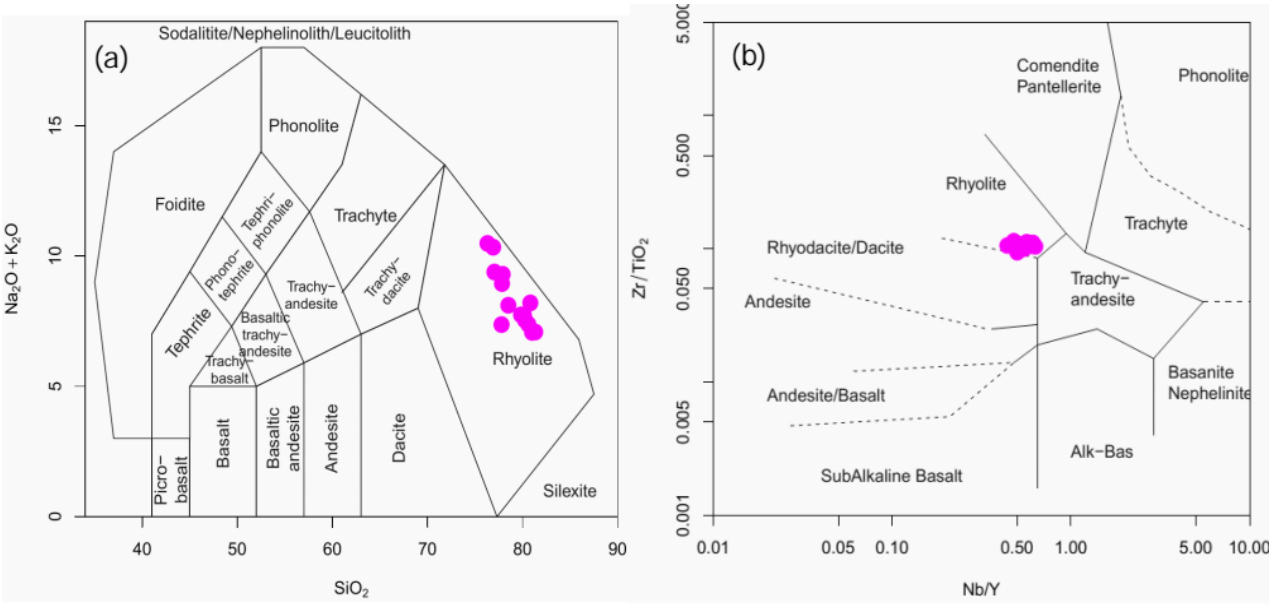

Figure 4. (a) TAS (total alkalis versus silica) classification diagram for volcanic rocks of the Shwebontha prospect [15], (b) Nb/Y vs Zr/TiO_2 plot of volcanic rocks from the Shwebontha prospect [16].

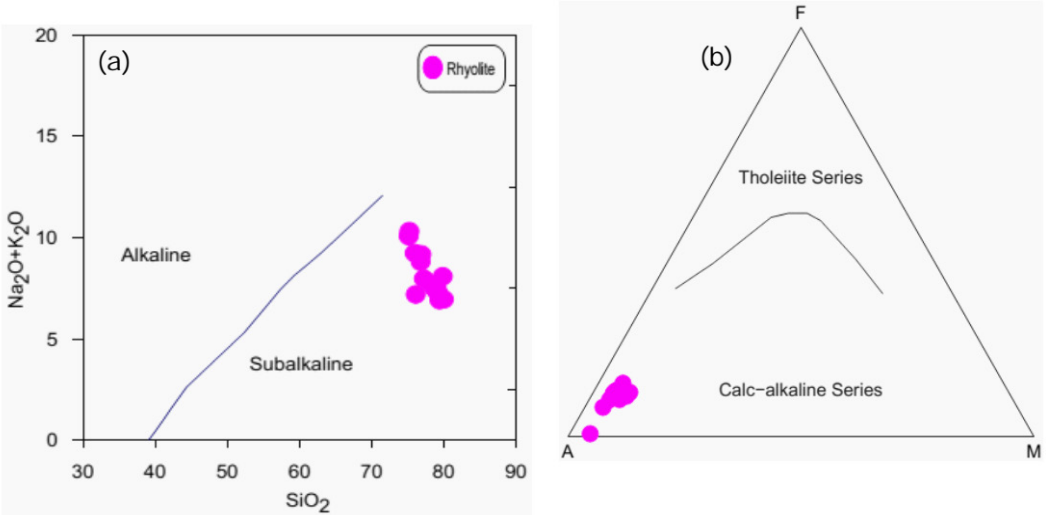

Figure 5. Subalkaline and alkaline classification plot diagram (SiO_2 vs Na_2O+K_2O) [17], AFM classification diagram [17] for volcanic rocks of the Shwebontha prospect.

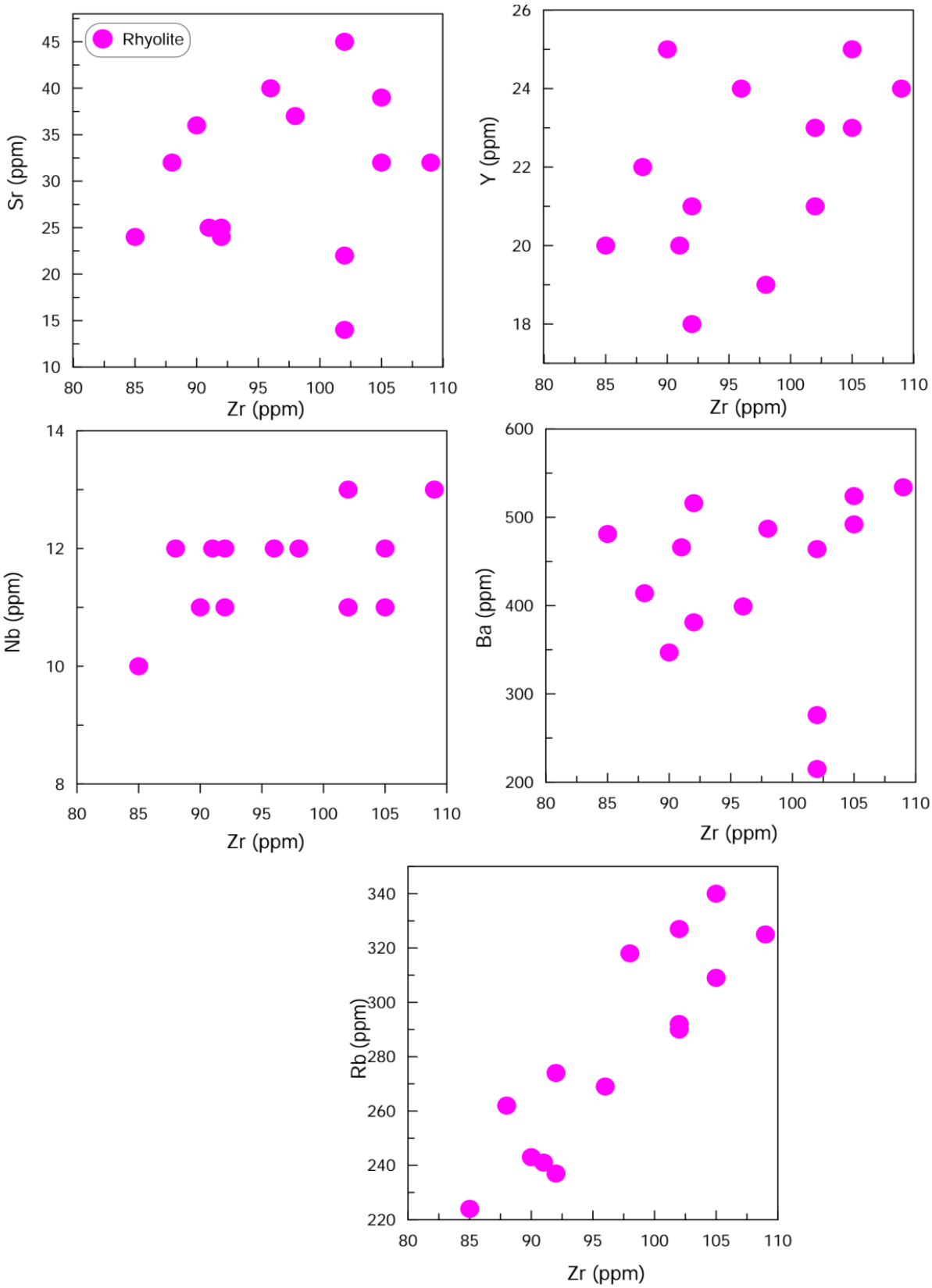

Figure 6. Binary plot diagrams of Rb, Nb, Sr, Ba, Y, and Zr (all in ppm) for rhyolite host rocks at Shwebontha prospect.

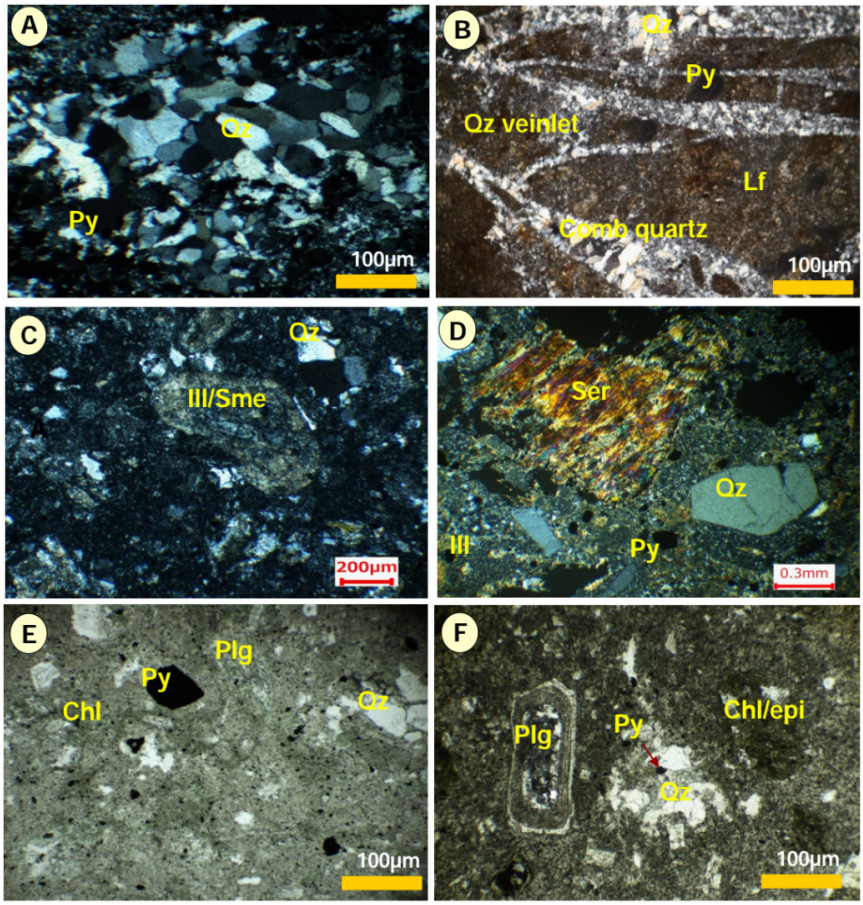

Figure 7. Photomicrographs showing hydrothermal alteration minerals at the Shwebontha prospect. (Qz-quartz, Ill-illite, Sme-smectite, Chl-Chlorite, Epi-Epidote, Py-Pyrite, Plg-Plagioclase, Lf-Lithic fragment).

5.3 Mineralization characteristics

Gold-based metal mineralization is principally hosted by rhyolite rock units in the Shwebontha prospect. Massive orebody of brecciated gold-bearing quartz veins is concentrated on the foremost veins and in zones of argillic altered wall-rocks and oxidized zones (**Figure 8**). The veins belonged to open-space filling and occasionally disseminated nature. Sulfide minerals are also occurred as in the chalcedonic quartz veins alternating with strongly silicified zones cut by cherty or sugary quartz veins in the rhyolite host rock as dissemination (**Figure 8**). Pyrite is the most common sulfide mineral. It observes either as fine-grained disseminations and aggregates in quartz or as infillings in vugs. Primary (hypogene) minerals are pyrite, sphalerite, galena, chalcopyrite, and gold. Secondary (supergene) minerals include covellite whereas gangue minerals are mainly composed of quartz.

Pyrite is distributed and is the most abundant sulfide in the mineralized veins and host rocks. It shows anhedral to euhedral (**Figure 9**), pale yellow to yellowish white. On the other hand, irregular cracks and cataclastic deformation of pyrite are observed in the gangue matrix. Most of the pyrite was replaced by anhedral grains of galena, sphalerite, and chalcopyrite (**Figure 9**). Galena exhibits light grey color and anhedral form. It occurs as a mineral that replaced pyrite (**Figure 9**). Sphalerite is observed as anhedral grain. It is grey and displays internal reflection. Sphalerite appears to have replaced pyrite (**Figure 9**). Gold is significant and occur as native gold or electrum granular grains in euhedral pyrite crystal. It is very fine-grained (1-2 μm), occasionally up to 200 μm. Covellite occurs as a secondary mineral and is generally found as fine-grained disseminated crystals replacing pyrite.

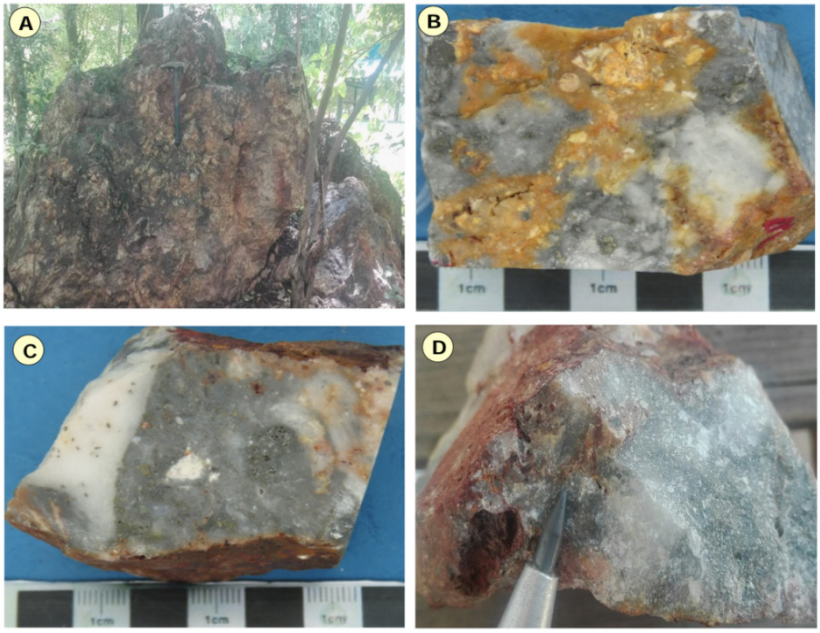

Figure 8. Outcrops and hand specimens showing (a) gold- base metal bearing silicified massive ore, (b,c) gold-bearing brecciated quartz veins and (d) chalcedonic quartz vein in the rhyolite host rock.

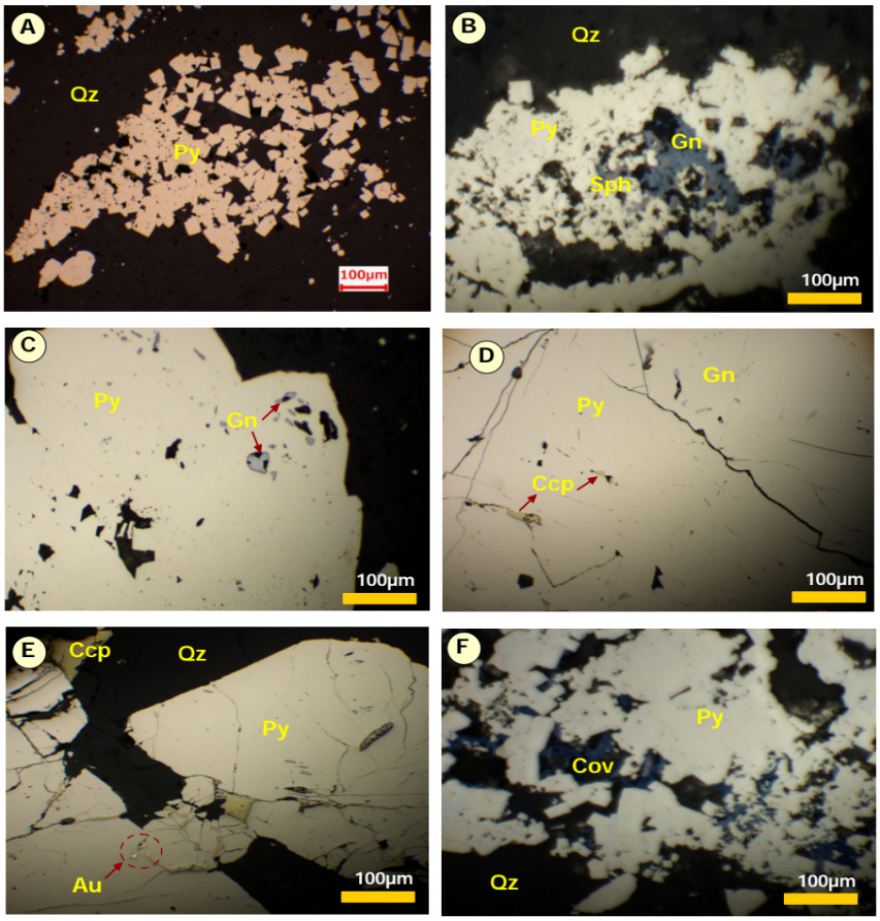

Figure 9. Reflected light photomicrographs of ore mineral assemblages from the Shwebontha prospect. (Py-Pyrite, Gn-Galena, Sph-Sphalerite, Au-Gold, Ccp-Chalcopyrite, Cov-Covellite, Qz-quartz).

5.4 Ore mineralizing fluids

Fluid inclusion micro thermometry was carried out for primary fluid inclusions in quartz from the mineralized quartz veins. The salinity and homogenization temperature resulting from primary fluid inclusions from quartz-hosted inclusions range from 0.35 wt.% to 2.41 wt.% NaCl equivalent and 158 °C to 310 °C respectively (**Figure 10**). The relationship between the salinities and homogenization temperatures of fluid inclusions probably reflects a complex sequence of fluid events, such as isothermal mixing, boiling, simple cooling, mixing of fluids with different homogenization temperatures and salinities and leakage. The data distribution diagram of homogenization temperature and salinity [18] points out that the ore mineralization within the Shwebontha prospect is a result of fluid mixing from various homogenization temperatures and salinities (**Figure 11**). On the other hand, magmatic fluids are thought to be genetically related to fluid salinities of 5-10 wt% NaCl equivalent [19-21]. In comparison, the values of low salinity fluids (less than 3.0 wt% NaCl equivalent) from the Shwebontha prospect suggests that the low salinity fluids of the study area belonged to a dominant origin of meteoric. The salinity from the sample in this study ranges from 0.35-2.41 wt% NaCl equivalent while those of the magmatic fluids range from 5-10 wt% NaCl equivalent. The numbers in magmatic systems are very higher than the results in this study [18]. On the other hand, previous research on fluid inclusions has recognized a close relationship between the salinity and homogenization temperature that is suggestive of the source of the fluid [18,22]. This reveals that the low-salinity ore mineralizing fluids of the Shwebontha prospect were generated by the mixing of a dominant meteoric water phase with small or trace amounts of magmatic fluid. The relationship between salinities and homogenization temperatures of fluid inclusions. The relationship between salinities and homogenization temperature of fluid inclusions is displayed in **Figure 11**.

5.5 Conceptual model of Shwebontha prospect

The conceptual model for the development of the epithermal system in the Shwebontha prospect was based on the emplacement of a reduced, near neutral pH, and dilute fluids formed by the input of magmatic components into deep circulating ground waters level and are typically associated with calc-alkaline to alkaline magmatism, in volcanic arcs low-intermediate and high-sulfidation epithermal system (**Figure 12**). At the initial stage of mineralization, the hydrothermal fluid phase exsolved and concentrated ore-forming metals and volatiles during the ascending, followed by crystallization, and cooling of magma [20]. Along the mineralized ore zones, rising fluids (as a result of pressure release) are heading to a higher elevation where they can be boiling fluid as well as mixing fluid with circulating meteoritic fluids.

In the first stage of epithermal gold mineralization, gold-bearing silicified massive ore as well as chalcedonic quartz vein for the Shwebontha prospect were precipitated at a shallow level by fluid mixing processes of the hydrothermal system. Those mineralized veins are formed by changing fluid conditions where the mixing of fluids is the principal mechanism of the gold and base metals deposition process in this epithermal system. Successive changing of the fluid conditions by fluid mixing resulted in repetitive layers in mineral assemblages such as quartz, carbonate, chalcedony and sulfides. At this phase, gold is precipitated as an electrum. In addition, hydrothermal alteration zones are also occupied as silicification as well as argillic alteration and propylitic alteration zone by interaction with wall rocks and the nature of hydrothermal fluids.

At the second stage of mineralization, as the fluid mixing continued under hydrostatic conditions, the releases of carbon dioxide and hydrogen sulfide gasses increased the pH of the fluid, which could have been derived by the precipitation of gold-bearing silicified massive ore as well as chalcedonic quartz vein for the Shwebontha prospect. In places, gold is deposited as native gold or electrum. This transition is related to a progressive decrease in sulphur fugacity, oxidation state, and acidity [23]. The former represents the high-sulfidation state (e.g., at Letpadaung taung, Kyinsintaung and Sabetaung) and the latter indicates the intermediate to low-sulfidation state

of ore-forming fluids (Shwebontha). Here, it does not mean that mineralizations have been generated without having a break; instead, some un-renowned processes can be interrupted the precipitation and ore depositional process. Fluid mixing is believed to be the major cause of gold and base metals deposition in the Shwebontha prospect. Fluid mixing between hot, acidic and saline-bearing ore fluid and cooler meteoric water might be also responsible for gold and base-metals deposition. Based on the geochemical characteristic, ore textures, hydrothermal alteration mineral assemblages and mineralization styles and natures of the hydrothermal fluids, allow interpretation of the low to intermediate sulfidation epithermal system (**Figure 12**).

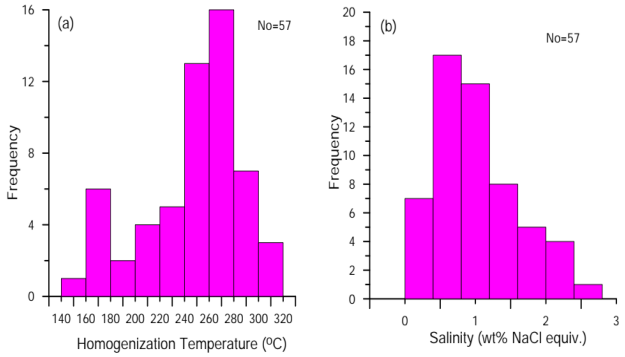

Figure 10. Data distribution of homogenization temperature and salinity histograms of the fluid inclusions from the Shwebontha prospect.

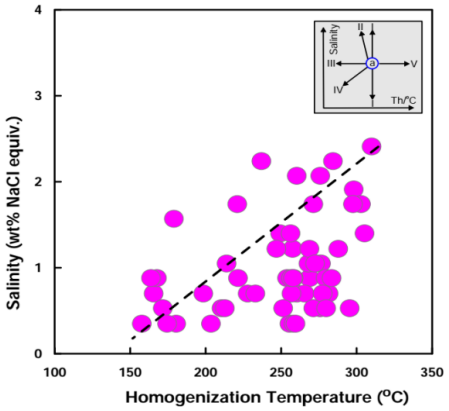

Figure 11. Mixing trend based on homogenization temperatures vs. salinities plot at Shwebontha prospect (modified after [18]). The supplement figure displays salinity and homogenization temperature trends or fluid evolution processes (modified from [22]). (I) isothermal mixing; (II) boiling; (III) simple cooling; (IV) mixing of fluids with different homogenization temperatures and salinities; (V) leakage.

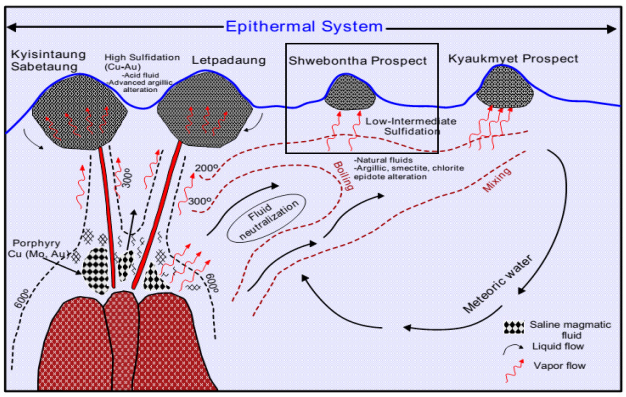

Figure 12. A conceptual model for the development of an epithermal at the Shwebontha prospect area, Monywa copper-gold ore field, central Myanmar (Modified after [4]).

6. Conclusions

The regional tectonic setting of the Shwebontha prospect is characterized by a subduction-related Central Volcanic Belt which plays an important role in the formation of an epithermal system. Alteration/mineralization in the research area is hosted by a sequence of Upper Oligocene to Middle Miocene Magyigon Formation calc-alkaline volcanic rocks (rhyolite). The calc-alkaline host rocks are consistent with magmatic rock associations that are commonly associated with the epithermal deposit. The alteration zones consist of silicic, argillic, and propylitic. The silicic alteration is represented by chalcedony, disseminated pyrite with medium to coarse-grained quartz and quartz veinlets in the brecciated sulfide quartz vein and chalcedonic quartz vein. Argillic alteration is mainly characterized by a variable amount of quartz, plagioclase, opaque minerals and clay minerals (sericite, illite, illite/smectite, and kaolinite. The propylitic is characterized by the selective alteration with dominant mineral assemblages of quartz, chlorite, epidote and pyrite. The mineralization is recognized by gold-bearing silicified massive ore and chalcedonic quartz veins. The principal ore mineral includes pyrite, sphalerite, galena, and gold. In addition, gangue minerals, including quartz, illite, illite/smectite, sericite, chlorite, and epidote have been recorded. The fluid inclusions data and interpretation revealed that mineralization was driven by

the mixing of ore mineralizing fluid at an originated temperature of 158-310 °C. The fluid salinity is 0.35-2.41 wt.% NaCl equivalent. Our study suggests that the mineralization style at the Shwebontha prospect is considered to be under an epithermal environment.

Author Contributions

T.N.O and K.Z.O carried out the fieldworks and developed the concepts, designed on this research. T.N.O. collected the data and samples as well as conducted the laboratory analysis and wrote this manuscript with contribution on discussion from K.Z. All authors were contributed in reading, comments and giving the annotations on this manuscript.

Conflicts of Interest

The authors declare no conflict of interest.

Funding

This study was supported by AUN/SEED-Net and JICA program.

Acknowledgment

This study is part of Ph.D dissertation of the first author who has been funded by AUN/SEED-Net (JICA program) in the fiscal year 2017–2021. The authors would like to acknowledge Rector Dr Khin Thidar, Rector of West Yangon University for her encouragement to submit this manuscript to the Journal of Geological Research. The authors are immensely grateful to Prof. Dr. Akira Imai, Assoc. Prof. Dr. Kotaro Yonezu, and laboratory members of Kyushu University, Japan for their massive support and valuable suggestions on data analysis and interpretation. The authors also thank to Prof. Dr. Khin Zaw of CODES, University of Tasmania his kind help and insightful suggestions into the geological information of Monywa copper-gold field.

References

[1] Mitchell, A.H.G., Myint, W., Lynn, K., et al., 2011. Geology of the high sulfidation copper deposits, Monywa mine, Myanmar. Resource Geology. 61, 1-29.

[2] Knight, J., Zaw, K. (editors), 2015. The geochemical and geochronological framework of the Monywa high sulfidation Cu and low sulfidation Au-epithermal deposits, Myanmar. Poster No. 104 presented at the SEG, Conference; Hobart, Tasmania, Australia.

[3] Oo, T.N., Harijoko, A., Setijadji, L.D., 2021. Fluid inclusion study of epithermal gold-base metal mineralization in the shwebontha prospect, Monywa Mining District, Central Myanmar. Journal of Applied Geology. 6(1), 1-16.

[4] Htet, W.T., 2008. Volcanic-hosted gold-silver mineralization in the Monywa mining district, central Myanmar [PhD thesis]. Myanmar: Mandalay University.

[5] Zaw, K., Swe, Y.M., Myint, T.A., et al., 2017. Copper deposits of Myanmar. Geological Society Memoir. 48, 573-588.

[6] Mitchell, A.H.G., Myint, T.H., 2013. The Magmatic Arc and Slate Belt: Copper–gold and tin–tungsten and gold metallotects in Myanmar. East Asia: Geology, exploration technologies and Mines extended abstracts. Bulletin (Australian Institute of Geoscientists). 57.

[7] Gardiner, N.J., Robb, L.J., Searle, M.P., 2014. The metallogenic provinces of Myanmar. Applied Earth Science. 123, 25-38.

[8] Zaw, K., 1990. Geological, petrological and geochemical characteristics of granitoid rocks in Burma: With special reference to the associated W-Sn mineralization and their tectonic setting. Journal of Southeast Asian Earth Sciences. 4, 293-335.

[9] Mitchell, A., Chung, S.L., Oo, T., et al., 2012. Zircon U-Pb ages in Myanmar: Magmatic-metamorphic events and the closure of a neo-Tethys ocean? Journal of Asian Earth Science. 56, 1-23.

[10] Searle, M.P., Noble, S.R., Cottle, J.M., et al., 2007. Tectonic evolution of the mogok metamorphic belt, Burma (Myanmar) constrained by U-Th-Pb dating of metamorphic and magmatic rocks. Tec-

tonics. 26(3).
DOI: https://doi.org/10.1029/2006TC002083

[11] Swe, W. (editor), 1972. A Strike-slip faulting in central belt of Burma [abstr.]. Regional Conference on the Geology of SE Asia, Kuala Lumpur. Kuala Lumpur; Geological society of Malaysia Kuala Lumpur.p. 34, 59.

[12] Naing, M.M., 2003. Petrology and mineralization of Sabe, Kyisin and Letpadaung copper deposits, Monywa District, Central Myanmar [PhD thesis]. Mandalay: University of Mandalay.

[13] Mitchell, A.H.G., Asua, C., Deiparine, L. (editors), et al., 1999. Geological settings of gold districts in Myanmar. PACRIM 99 Congress; Bali, Indonesia. Australia: AusIMM.

[14] Bodnar, R.J., 1993. Revised equation and table for determining the freezing point depression of H_2O NaCl solutions. Geochimica et Cosmochimica Acta. 57(3), 683-684.

[15] Middlemost, E.A.K., 1994. Naming materials in the magma/igneous rock system. Earth Science Reviews. 37(1), 19-26.

[16] Winchester, J.A., Floyd, P.A., 1977. Geochemical discrimination of different magma series and their differentiation products using immobile elements. Chemical Geology. 20, 325-343.

[17] Irvine, T.N., Baraga, W.R.A., 1971. A guide to the chemical classification of the common volcanic rocks. Canadian Journal of Earth Sciences. 8, 523-548.

[18] Wilkinson, J.J., 2001. Fluid inclusions in hydrothermal ore deposits. Lithos. 55, 229-272.

[19] Burnham, C.W., 1979. Chapter 3: Magmas and hydrothermal fluids. Barnes, H.L. (editor), Geochemistry of hydrothermal ore deposits, 2nd edition. John Wiley & Sons Inc: New York. pp. 71-136.

[20] Hedenquist, J.W., Lowenstern, J.B., 1994. The role of magmas in the formation of hydrothermal ore deposits. Nature. 370, 519-527.

[21] Simmons, S.F., Brown, K.L., 2006. Gold in magmatic hydrothermal solutions and the rapid formation of a giant ore deposit. Science. 314, 288-291.

[22] Shepherd, T.J., Rankin, A.H., Alderton, D.H.M., 1985. A Practical Guide to Fluid Inclusion Studies. Blacie & Son Press: London.

[23] Hayba, D.O., Bethke, P.M., Heald, P., et al., 1985. Geologic, mineralogic, and geochemical characteristics of volcanic-hosted epithermal precious metal deposits. Reviews in Economic Geology. 2, 129-167.

Appendix

Appendix A. Result of XRF whole rock chemical analyses of volcanic rocks from the Shwebontha prospect.

Sample ID	SR1	SR15	SR14	SR10	SR7	SR20	SR11	SR13	SR5	SR2	SR6	SR17	SR22	R8
Major elements (in wt%)														
SiO_2	76.1	77.1	75.2	79.2	78.9	78.4	79.9	78.9	75.9	76.8	79.8	79.4	75.1	76.8
TiO_2	0.10	0.10	0.10	0.09	0.09	0.10	0.09	0.08	0.09	0.09	0.09	0.08	0.10	0.09
Al_2O_3	12.8	11.3	11.5	10.2	10.4	10.3	9.56	10.0	11.5	10.9	9.11	10.0	11.7	11.08
FeO	0.99	1.12	0.84	0.86	0.80	0.92	0.93	1.22	1.16	0.96	1.07	0.82	0.08	1.19
MnO	0.01	n.d	n.d	n.d	n.d	n.d	n.d	n.d	n.d	n.d	n.d	n.d	n.d	n.d
MgO	0.54	0.53	0.45	0.55	0.57	0.70	0.67	0.49	0.48	0.46	0.44	0.58	0.47	0.50
CaO	0.14	0.17	0.14	0.17	0.17	0.17	0.16	0.16	0.19	0.21	0.16	0.18	0.14	0.19
Na_2O	0.52	0.56	0.60	0.51	0.52	0.52	0.51	0.64	0.80	0.88	0.62	0.50	0.58	0.77
K_2O	6.69	7.42	9.73	6.75	6.90	7.09	6.46	6.98	8.45	8.30	7.48	6.43	9.51	8.05
P_2O_5	n.d	n.d	n.d	n.d	n.d	0.01	0.01	n.d	0.01	0.01	n.d	n.d	0.01	0.01
H_2O	2.10	1.55	1.27	1.61	1.57	1.62	1.54	1.37	1.31	1.22	1.07	1.88	1.46	1.25
Total	99.9	99.8	99.8	99.9	99.9	99.9	99.9	99.9	99.9	99.9	99.85	99.9	99.1	99.9

Appendix A continued

Sample ID	SR1	SR15	SR14	SR10	SR7	SR20	SR11	SR13	SR5	SR2	SR6	SR17	SR22	R8
Trace elements (in ppm)														
V	17	18	14	3	10	14	7	5	13	10	6	0	5	6
Cr	n.d	n.d	n.d	n.d	n.d	n.d	n.d	n.d	n.d	n.d	n.d	n.d	n.d	n.d
Co	30	36	42	45	50	27	30	55	50	40	34	36	23	25
Ni	11	13	8	8	8	7	12	9	8	9	13	7	6	11
Cu	2.01	23	31	22	41	24	30	78	49	25	19	31	5	3
Zn	46	50	n.d	26	9	3	n.d	47	18	33	7	12	10	20
Pb	5	9	8	11	22	17	6	n.d	6	23	31	41	23	45
As	13	7	8	6	8	31	43	9	10	12	19	9	7	11
Mo	13	11	11	11	9	11	7	7	10	10	9	8	9	10
Rb	292	290	340	237	241	269	243	274	318	327	262	224	325	309
Sr	14	22	32	24	25	40	36	25	37	45	32	24	32	39
Ba	215	276	524	516	466	399	347	381	487	464	414	481	534	492
Y	21	23	25	21	20	24	25	18	19	23	22	20	24	23
Zr	102	102	105	92	91	96	90	92	98	102	88	85	109	105
Ta	n.d	n.d	n.d	n.d	n.d	n.d	n.d	n.d	n.d	n.d	n.d	n.d	n.d	n.d
Nb	11	11	12	12	12	12	11	11	12	13	12	10	13	11

BILINGUAL PUBLISHING GROUP
Pioneer of Global Academics Since 1984

Advances in Geological and Geotechnical Engineering Research
https://journals.bilpubgroup.com/index.php/agger

ARTICLE

The Effect of Jet Grouting on Enhancing the Lateral Behavior of Piled Raft Foundation in Soft Clay (Numerical Investigation)

Mostafa Elsawwaf, Wasiem Azzam, Nahla Elghrouby*

Faculty of Engineering, Tanta University, Tanta, 31511, Egypt

ABSTRACT

Soft clay soils cannot usually support large lateral loads, so clay soils must be improved to increase lateral resistance. The jet grouting method is one of the methods used to improve weak soils. In this paper, a series of 3D finite element studies were conducted using Plaxis 3D software to investigate the lateral behavior of piled rafts in improved soft clay utilizing the jet grouting method. Parametric models were analyzed to explore the influence of the width, depth, and location of the grouted clay on the lateral resistance. Additionally, the effect of vertical loads on the lateral behavior of piled rafts in grouted clay was also investigated. The numerical results indicate that the lateral resistance increases by increasing the dimensions of the jet grouting beneath and around the piled raft. Typical increases in lateral resistance are 11.2%, 65%, 177%, and 35% for applying jet grouting beside the raft, below the raft, below and around the raft, and grouted strips parallel to lateral loads, respectively. It was also found that increasing the depth of grouted clay enhances lateral resistance up to a certain depth, about 6 to 10 times the pile diameter (6 to 10D). In contrast, the improvement ratio is limited beyond 10D. Furthermore, the results demonstrate that the presence of vertical loads has a significant impact on sideward resistance.

Keywords: Finite element analysis; Plaxis 3D; Lateral bearing capacity; Jet grouting; Piled raft; Soil improvement

1. Introduction

Piled rafts are currently the most widely used foundations to support high buildings, tall wind turbines, highway bridges, and marine structures. Generally, the piled raft system is intended to withstand vertical and sideward loads. The lateral loads can

*CORRESPONDING AUTHOR:
Nahla Elghrouby, Faculty of Engineering, Tanta University, Tanta, 31511, Egypt; Email: nahla.mofreh@gmail.com

ARTICLE INFO
Received: 23 December 2022 | Revised: 14 January 2023 | Accepted: 24 January 2023 | Published Online: 13 February 2023
DOI: https://doi.org/10.30564/agger.v5i1.5347

CITATION
Elsawwaf, M., Azzam, W., Elghrouby, N., 2023. The Effect of Jet Grouting on Enhancing the Lateral Behavior of Piled Raft Foundation in Soft Clay (Numerical Investigation). Advances in Geological and Geotechnical Engineering Research. 5(1): 24-39. DOI: https://doi.org/10.30564/agger.v5i1.5347

be induced by earthquakes, wind forces, landslides, ice flows, wave forces on offshore structures, and also lateral earth forces on the retaining structures. The lateral demeanor of pile rafts is a fundamental and critical consideration in the design. Therefore, the essential purpose of this paper is to evaluate the viability of soil enhancement using the jet grouting technique for boosting the lateral demeanor of rafts over piles buried in soft clays.

There are several factors that influence the lateral behavior of piled foundations, particularly those related to the geometrical design of the piles, such as extending the pile length [1-3], augmenting the piles' number [2,4], increasing central spacing between piles [1-4], using fin piles [5,6], using helical piles [7], and expanding the pile diameter [8].

Alternatively, a less costly and more effective method is employed to enhance the sideward pile resistance. This method involves using soil enhancement techniques. Because the sideward resistance of the piles is frequently influenced by the top stratum of soils (5-10D times the pile diameter), the enhanced soil could be somewhat shallow [9-12]. The soil enhancement techniques include replacing the upper weak clay soil with a compacted sand backfill [12,13], compacting the top layer of sands [14,15], utilizing gravel compaction to enhance the sideward behavior of piles buried in a coal ash deposit [16], employing cement deep soil mixing method (CDSM) [11,17], using cement-treated soil around the piles [12,18,19], applying vertical sheets of geotextile in a single layer and double layers in the sand [2], and utilizing the jet grouting technique [8,13,20,21].

Since the constructions are subjected to both sideward and vertical loads, some researchers have discovered that applying vertical loads has a substantial influence on the lateral demeanor of single piles [22-29], pile groups [30], and piled rafts [31,32]. Therefore, this paper investigates the lateral behavior of piled rafts subjected to compound loads in enhanced and unenhanced clays.

Although soil improvement using the jet grouting technique has the potential to reduce construction costs and time, there have been few studies on utilizing jet grouting in soft clay. Furthermore, most previous papers investigated the lateral response of single piles or pile caps that used a limited number of piles or small-scale models, but there have been very few evaluations on a full-scale piled raft. As a result, in this study, a full-scale raft over piles is numerically studied using PLAXIS 3D software to discover the effect of using jet grouting on the lateral response of piled rafts and help design engineers evaluate the effectiveness of this approach.

2. Numerical modeling

The finite element analysis method is one of the most used methods to eliminate the cost of field testing by getting approximate solutions for the different problems in several engineering fields. Many programs are used for numerical analysis. The Plaxis 3D program is adopted in this study to simulate the piled raft foundation subjected to lateral loads in improved and unimproved soft clay.

2.1 Soil modeling

In this study, the soil profile consists of a layer of soft clay with a thickness of 17 m, and below this layer is a layer of dense sand with a thickness of 23 m as shown in **Figure 1**. The soil is modeled by Hardening Soil Model (HS). In the HS model, soil stiffness is more accurate because of the use of the following inputs: triaxial secant stiffness (E_{50}), oedometer tangent stiffness (E_{oed}), and unloading reloading stiffness (E_{ur}). The values for stiffness are set in the default settings of the program as follows: ($E_{oed} = E_{50}$) and ($E_{ur} = 3\ E_{50}$) as average values for different types of soil. **Table 1** shows the properties of the used soil [33,34].

2.2 The jet grouting

The main effect of jet grouting is to increase the mechanical properties of the soil, such as compression strength, shear resistance, and elastic modulus. In this study, the unconfined compressive strength of grouted clay soil (q_u) is chosen to be equal to

3000 KPa according to previous studies [13,35-40] as shown in **Table 2**. Young's modulus is estimated to be equal to 100 q_u [41,42]. The cohesion (C) and friction angle (φ) were calculated based on Equations (1) & (2) [42,43].

$$c = \frac{q_u\, q_t}{2[q_t\,(q_u - 3q_t)]^{0.5}} \quad (1)$$

$$\mathrm{Tan}(\phi) = \frac{q_u{}^2 - 4c^2}{4q_u * c} \quad (2)$$

where (q_u) is the unconfined compressive strength, and (q_t) is the tensile strength (q_t) is taken as 14% of compressive strength [44]. The unit weight of the grouted clay (ɣ) was assumed to be the same as the unimproved clay soil. In this analysis, the jet grouting is modeled using the Hardening Soil Model (HS). The material properties of jet-grouted soil are summarized in **Table 1**.

Table 1. Details of material parameters used in 3D finite element analysis [33,34].

Parameter	Symbol	Soft clay	Dense sand	Jet grouting	Unit
Material model	-	Hardening soil	Hardening soil	Hardening soil	-
Drainage type	-	Undrained A	Drained	Undrained A	-
Saturated unit weight	γ_{sat}	17.9	20	17.9	KN/m^3
Dry unit weight	γ_{unsat}	12.5	17	12.5	KN/m^3
Cohesion	c`	25	0	737	KN/m^2
Friction angle	ϕ`	0	40	38	degree
Dilatancy angle	ψ	0	10	8	degree
Poisson's ratio	$v`_{ur}$	0.2	0.2	0.2	-
Secant stiffness	E_{50}^{ref}	2800	50×10^3	300×10^3	KPa
Tangent stiffness	E_{oed}^{ref}	2800	50×10^3	300×10^3	KPa
Unloading reloading stiffness	E_{ur}^{ref}	8400	150×10^3	900×10^3	KPa
power	m	1	0.5	1	-

Table 2. The ranges of unconfined compression strength for grouted clay according to previous studies.

Unconfined compression Strength for grouted clay (KPa)	References
3100-4500	Rollins et al. [13]
< 5000	Miki [35]
2000-14000	Fang and Liao [36]
1800-3000	Melegari and Garassino [37]
3000-14000	Stoel and Ree [38]
1000-5000	Ökmen [39]
1700-3400	Burke [40]

2.3 Piled raft modeling

The piled raft model consists of a raft with a cross-section (14 m × 12 m) and a 0.7 m thickness over a group of piles (7 × 6). The piles are 20 meters in length (L_{pile}). The piles embed in 17 m of clay and extend to 3 m of sand. The diameter of the piles is equal to 0.5 m (D). The central distance between the piles is four times the pile diameter (4D = 2 m), as shown in **Figure 1**. In this analysis, the piles are modeled using embedded piles as massive circular piles and the raft is modeled using plate elements. The unit weight of the reinforced concrete for rafts and piles is chosen as an average value to be equal to 25 KPa. The young's modulus of the raft and the piles is taken as 22 Gpa which is calculated from equation E_c= 4400 $\sqrt{F_{cu}}$ (MPa) [45], where (F_{cu}) is the compressive strength of the concrete which is taken as 25 MPa.

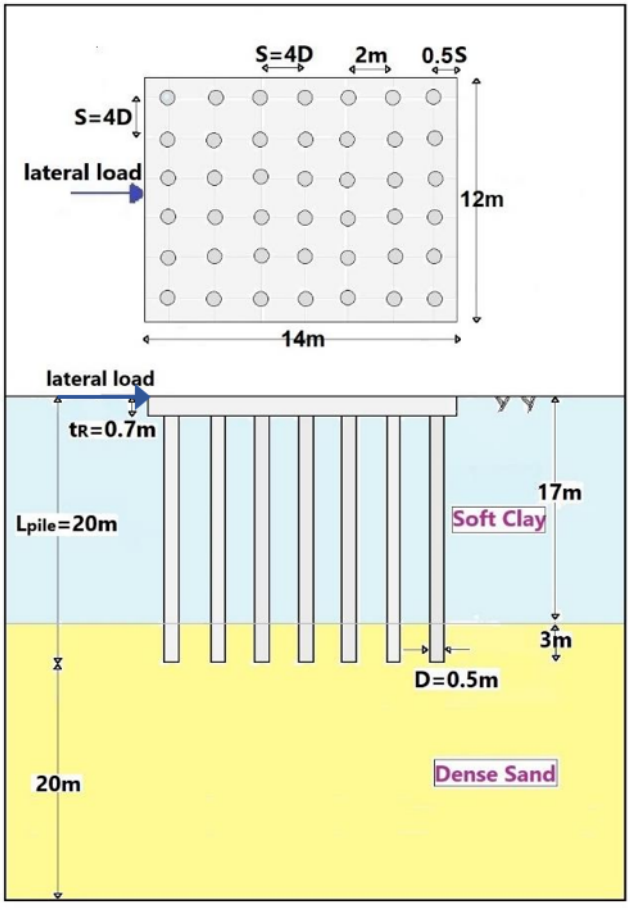

Figure 1. The model of the piled raft with constant parameters.

2.4 Mesh generation and model boundaries

To generate 3D meshes in the tridimensional Plaxis software package, the full geometric model must first be defined, and then the finite element mesh can be generated. A medium mesh is adopted for the model in this study because using fine meshes will lead to a huge increase in calculation times but the zone around the piled raft was refined as shown in **Figure 2**.

The dimensions of the soil mass model were chosen to avoid deformation near the model boundary and to prevent any effect on the numerical results. In the horizontal plane, the model boundaries are measured from the edge of the raft foundation to all directions at a distance equal to three times the raft width (3B), and the model depth is measured at a distance equal to two times the pile length (2 L_{pile}), as depicted in **Figure 2**.

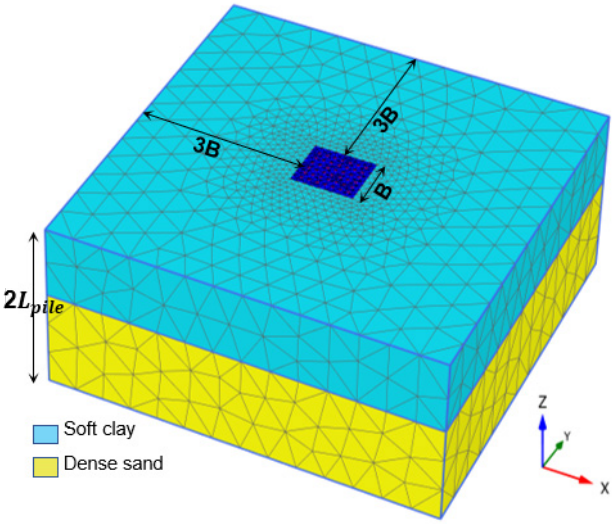

Figure 2. Finite element mesh and model boundaries for piled raft using Plaxis 3D.

3. Model verification

The finite element model is verified in this study by comparing the field results obtained by Rollins and Brown [9] and the experimental results obtained by Bahloul [15] with the current results of the numerical model to ensure that the PLAXIS 3D software is capable of achieving the objectives of the study.

3.1 Case study (1) Rollins and Brown

This validation is conducted by PLAXIS 3D on lateral load field tests that were carried out by Rollins and Brown [9] on full-scale pile groups (3 × 3) in clay layers improved by jet grouting below and around the pile cap. The pipe piles were 13.4 m long and had a wall thickness of 0.0095 m. The outer diameter of the piles was 0.324 m. The spacing between piles was 0.9 m. The pile cap had dimensions of 2.84 m × 2.75 m and a thickness of 0.76 m. The unconfined compressive strength of improved clay (q_u) was equal to 480 psi (3300 KPa), the elastic modulus of grouted soil is estimated to be equal to 100 qu (330 MPa) [41,42]. In this verification, the piles are modeled using embedded piles, the pile cap is modeled using plates and the soil is modeled by hardening soil. The average unit weight of the raft and piles is chosen to be equal to 25 KPa. The young's modulus of the raft and piles is assumed to be 22 Gpa. The empirical formula (E_s = 200-500 C_u) [46] was used to calculate the soil's young's modulus. The stiffness values are set as follows: (E_{oed} = E_{50}) and (E_{ur} = 3 E_{50}). The improved clay has dimensions of (4.57 m × 3.2 m) in the horizontal plane and a depth of 3 m from the bottom of the pile cap. The properties of the soil used in validation are given in **Table 3**. The comparison between load-displacement results of laterally loaded pile groups in improved soft clay for field test and numerical analysis is presented in **Figure 3**. From this comparison, it was found that the numerical results are very close to the results obtained from the field-test data.

Table 3. Details of material parameters used by Rollins and Brown [9].

Parameter for undrained B	Symbol	Lean clay	Fat clay	Lean clay with silt lenses	Sandy silt	Sandy lean clay	Lean clay	Interbedded lean clay and sandy silt	Unit
Level	-	0-1.2	1.2-2.5	2.5-4.5	4.5-7.5	7.5-10	10-13	13-15	
Saturated unit weight	γ_{sat}	18.5	17	18.3	19.2	19	18.5	18	KN/m^3
Dry unit weight	γ_{unsat}	18.5	17	18.3	19.2	19	18.5	18	KN/m^3
Cohesion	c`	25	16.7	19.8	27	35	43	50	KN/m^2
Friction angle	ϕ`	0	0	0	0	0	0	0	degree
Poisson's ratio	$v`_{ur}$	0.2	0.2	0.2	0.2	0.2	0.2	0.2	-
Secant stiffness	E_{50}^{ref}	5000	3300	4000	5400	7000	8600	10000	KPa
Tangent stiffness	E_{oed}^{ref}	5000	3300	4000	5400	7000	8600	10000	KPa
Unloading reloading stiffness	E_{ur}^{ref}	15000	9900	12000	16200	21000	25800	30000	KPa

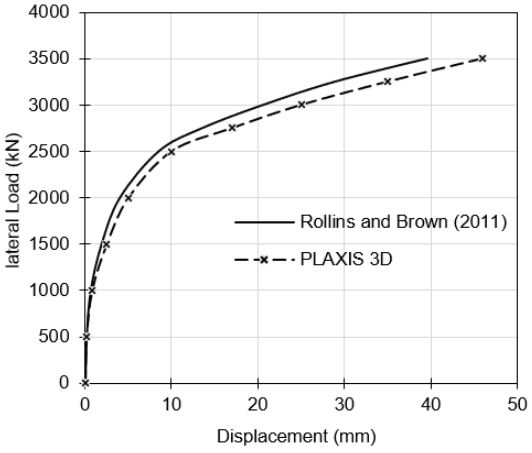

Figure 3. Comparison of the results for Plaxis 3D with the field test [9].

3.2 Case study (2) Bahloul

Bahloul [15] performed experimental loading tests on laterally loaded piles (2 × 3) in the sand. This study is validated by comparing the numerical results to the laboratory data. In this validation, the piles are steel pipes with a diameter of 0.01 m and have a length of 0.45 m. The spacing between piles is equal to 3D. The steel rigid cap has dimensions of (0.09 × 0.06) m and a thickness of 0.02 m. The unit weight and the elastic modulus of pile cap and steel pipes are taken as an average value to be equal to 78.5 KPa and 200 GPa, respectively. The piles, the rigid cap, and the soils are modeled using embedded piles, plates, and hardening soil, respectively. Bahloul [15] improved pile lateral behavior by compacting the top layer of sand to a depth equal to one-third of the pile's length. The soil's young's modulus was estimated using the equation for sand (E_{50} = 7000 $\sqrt{N}$) [46], where (N) is a value number from a standard penetration test (SPT), and N was estimated [47] using the relationship between (N) value, friction angle (φ), and relative density for sand. The stiffness values are set as follows in the program's default settings: ($E_{oed} = E_{50}$) and ($E_{ur} = 3\ E_{50}$). **Table 4** illustrates the properties of the materials used in this verification. **Figure 4** shows the lateral load–displacement relationships of numerical current results and experimental results for pile groups in the sand. The comparison revealed that the numerical analysis results are in good agreement with the data obtained from the experimental tests.

Table 4. Details of material parameters used by Bahloul [15].

Parameter for drained	Symbol	Dense sand	Loose sand	Unit
Saturated unit weight	γ_{sat}	17	15.5	KN/m^3
Dry unit weight	γ_{unsat}	16	14.5	KN/m^3
Cohesion	c`	5	5	KN/m^2
Friction angle	ϕ`	36	30	degree
Dilatancy angle	ψ	6	0	degree
Poisson's ratio	$v`_{ur}$	0.2	0.2	-
Secant stiffness	E_{50}^{ref}	38×10^3	22×10^3	KPa
Tangent stiffness	E_{oed}^{ref}	38×10^3	22×10^3	KPa
Unloading reloading stiffness	E_{ur}^{ref}	114×10^3	66×10^3	KPa
Power	m	0.5	0.5	-

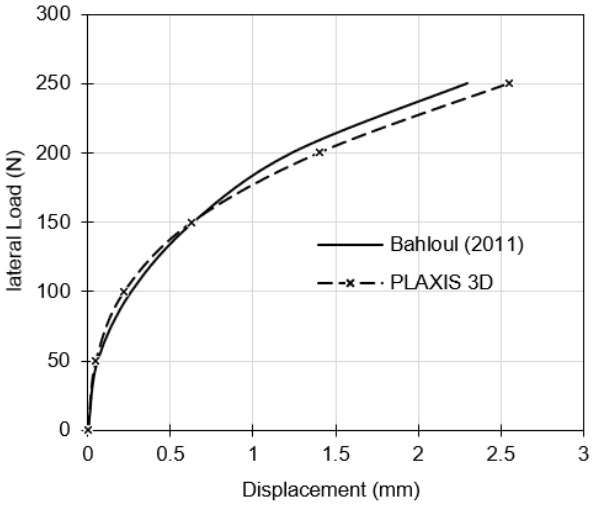

Figure 4. Comparison of the results for Plaxis 3D with the experimental test [15].

4. Parametric studies

A series of 3D finite-element analyses have been done on a raft over piles in soft clays and improved soft clays by using jet grouting to explore the lateral response of the piled raft under pure lateral loads. The studied parameters include the length (L), width (w), depth (d), and location of the improved clay as shown in **Table 5**. In addition, the lateral response of rafts over piles under combined lateral and vertical loads was investigated in grouted clay soil. **Figure 5** shows the geometric parameters used in the analysis. It should be noted that the pile diameter (D = 0.5 m), the pile length (L_{pile} = 20 m), no of piles (N_{pile} = 42), the raft cross-section (14 m × 12 m), and the raft thickness (t = 0.7 m) are always constant values in the analysis as illustrated in **Figure 1**.

The load control method is adopted in this analysis, in which the applied loads are gradually increased while iterative analysis is performed until failure occurs. The ultimate lateral loads were determined using the tangent intersection method [48-50], which is based on the intersection of two tangents of the load-displacement curve, where the intersection point gives the ultimate bearing capacity.

Table 5. Analysis parameters of the jet grouting.

Series	Constant parameters	Variable parameters	Grout location
1	L = 14 m, w = 12 m	d/D = 0, 2, 4, 6, 8,10,12,14,16	Below the piled raft
2	L = 12 m, w = 2 m (4D)	d/D = 0, 2, 4, 6, 8, 10	Beside the piled raft
3	d = 5 m (10D)	w/D = 0, 2, 4, 6, 8, 10	Below and around the piled raft
4	L = 14 m, d = 3 m (6D)	w/D = 0, 0.5, 1, 1.5, 2	Strips between the piles (Parallel to the lateral load)
5	L = 12 m, d = 3 m (6D)	w/D = 0, 0.5, 1, 1.5, 2	Strips between the piles (perpendicular to the lateral load)

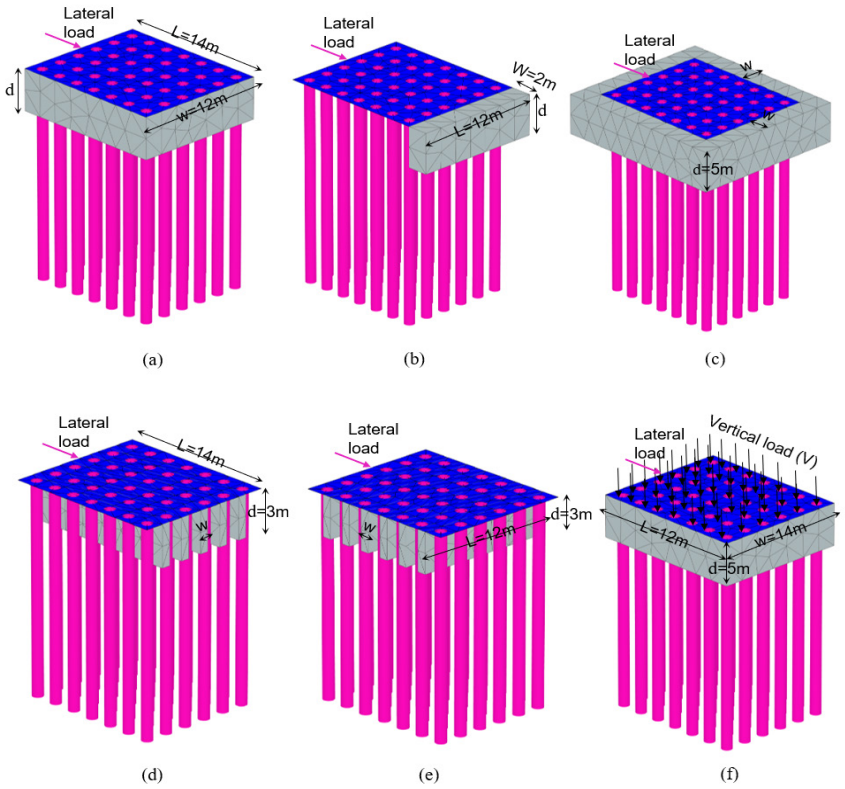

Figure 5. Different geometric parameters studied by PLAXIS 3D: (a) jet grout below the piled raft, (b) jet grout beside the piled raft, (c) jet grout below and around the piled raft, (d) jet grout strips parallel to lateral load, (e) jet grout strips perpendicular to lateral load, and (f) combined loads on the piled raft in grouted clay.

5. Results and discussion

5.1 The effect of the jet grouting depth below the piled raft

A series of numerical analyses were carried out to study the effect of grouted clayey soil beneath the piled raft on the lateral loading performance at different depths (d). The jet grouting has the same dimensions as the raft, where the length (L) is equal to 14 m in the direction of lateral loading and the width is equal to 12 m in the direction perpendicular to the lateral loading while the grouted depth is increased. The bottom of the jet-grouted soil is at depths ranging from 2 to 16D (1 m to 8 m), where (D) represents the pile's diameter, which is equal to 0.5 m as shown in **Figure 5a**. The lateral load-displacement curves for different grouted depths are presented in **Figure 6a**. The ultimate lateral loads were specified using the tangent intersection method for load-displacement curves [48-50], as previously explained. In the case of unimproved clay, the ultimate lateral load was found to be equal to 3750 KN. The ultimate lateral loads for improved clay were 4200 KN, 4700 KN, 5200 KN, 5700 KN, 6200 KN, 6500 KN, 6750 KN, and 7050 KN at depths of 2D, 4D, 6D, 8D, 10D, 12D, 14D, and 16D, respectively. To determine the increase in the lateral resistance, a ratio is defined as the improvement ratio (IR), which is the ultimate lateral load in the case of improved clay divided by the ultimate lateral load in the case of unimproved clay.

$$IR = \frac{L_{ui} \quad (\text{improved clay})}{L_{uu} \ (\text{unimproved clay})} \tag{3}$$

Figure 6b provides the relation between the improvement ratio (IR) versus d/D (the ratio of the improved depth to the pile diameter). The curves show that the lateral resistance of the piled raft increased by about 12%, 25%, 39%, 52%, and 65% for grouted depths of 2D, 4D, 6D, 8D, and 10D, respectively. However, at depths greater than 10D, lateral resistance increased slightly. According to the results, it can be seen that the jet grouting below the piled raft will greatly increase the lateral capacity compared to original clay, but when the grouted depth reaches a depth greater than 10 times the diameter of the pile (10D), the increase in lateral resistance is limited. This means that the jet grouting layer with a depth equal to (10D) is sufficient to improve passive resistance, and no additional jet grouting depth is required. These numerical results are consistent with the results published by Eltaweila et al. [12] & Rollins and Brown [9] who conducted that the improved depths close to the ground surface have a significant effect on the lateral resistance until a certain depth equal to about 10D and after that, the effect is not significant.

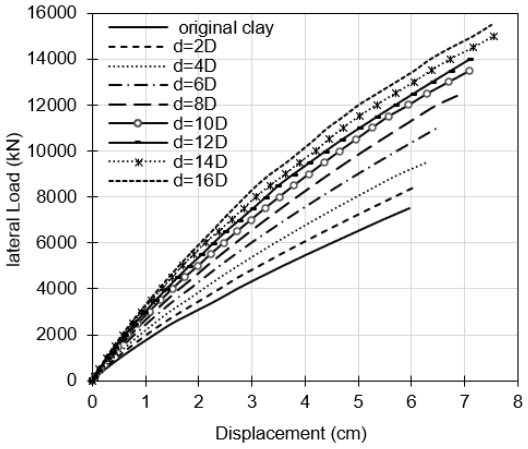

(a)

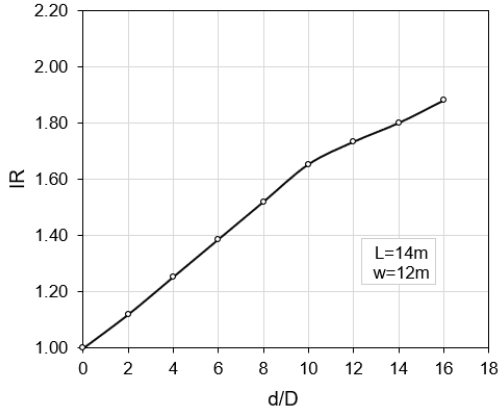

(b)

Figure 6. Jet grouting at different depths below the piled raft: (a) Lateral load-displacement curves, and (b) improvement ratio versus d/D ratio.

5.2 The effect of the jet grouting depth beside the piled raft

The numerical analyses were performed on the

piled raft before and after applying the jet grouting next to the piled raft. As shown in **Figure 5b**, the length of the jet grouting is the same as the width of the raft, where the grouted length (L) is equal to 12 m in the direction perpendicular to the loading and the grouting width (w) is constant to be equal to 2 m (4D) beside the piled raft in the same direction of the loading. The different values for jet grouting depth range from 2 to 10D (1 m to 5 m) and are measured from the ground surface. The lateral failure loads were estimated from load-displacement results, and the improvement ratio curve was plotted, as can be seen in **Figure 7**. The curves show that the lateral resistance enhanced by about 7%, 9%, 11%, 11.1%, and 11.2% for grouted depths of 2D, 4D, 6D, 8D, and 10D, respectively. According to these results, it is clear that the lateral resistance increases by increasing the jet grouting depth beside the piled raft to a certain depth equal to 3 m (6D), but after that, no increase occurs and the lateral resistance seems to become constant. These findings are consistent with the previous research, which found that the upper layers of soil 5 to 10 times the pile diameters (5-10D) have higher lateral resistance [9-11].

It's worth noting that the improvement ratio generated by applying the jet grouting beneath the piled raft is much greater than that generated by applying the jet grouting beside the piled raft for the same depths. Whereas, the improvement ratio (IR) increases from (1.1 to 1.65) at (d/D = 5) as illustrated in **Figure 9**. The explanation for this is due to the grout beneath the piled raft having a larger cross-sectional area than the grout adjacent to the piled raft, as well as the interaction between the piles and the improved clay based on Adsero [21], who found that about 35% of the enhancement in the lateral resistance is due to the interaction of the piles with the strengthened clay soil by jet grouting. These findings indicate that the jet grouting beneath the foundations is more cost-effective than applying the jet grouting beside the foundations. It must be taken into account that the directions of the lateral loads affected on the foundations are very random, so the jet grouting must be applied beside the piled raft from all sides but in contrast, applying the jet grouting below the piled raft will resist the lateral loads at any direction.

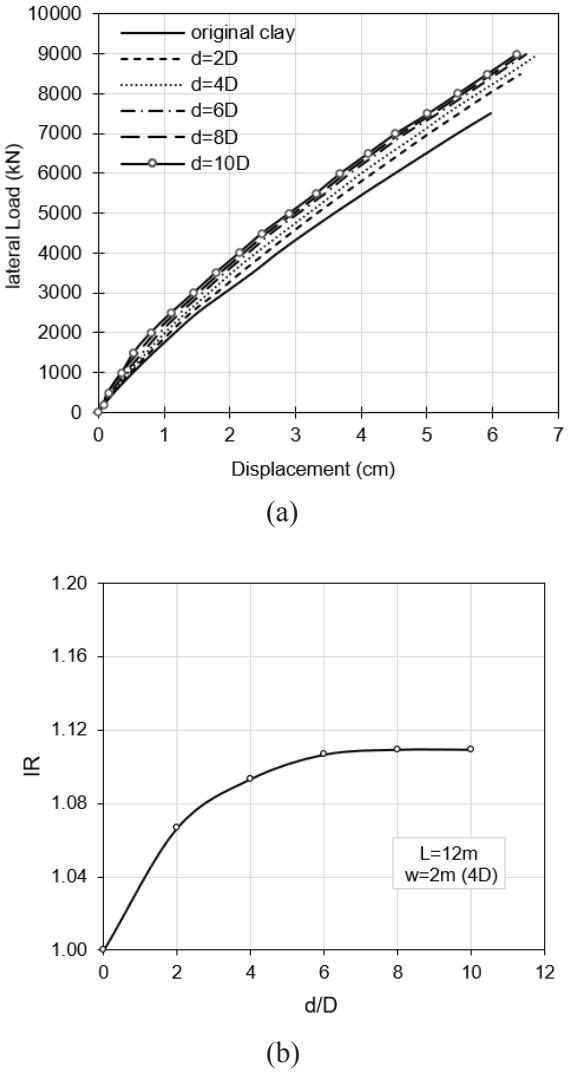

Figure 7. Jet grouting at different depths beside the piled raft: (a) Lateral load-displacement curves, and (b) improvement ratio versus d/D ratio.

5.3 The effect of jet grouting below and around the piled raft

In this parametric study, the grouted clay beneath and around the piled raft has a constant depth of 5 m (10D) measured from the ground surface and different widths around the piled raft to investigate the effect of increasing the width of the grout (w) on the lateral resistance as shown in **Figure 5c.** The jet grouting width values range from 2 to 10D (1 m to 5 m) measured from the edge of the piled raft from

all sides. The tangent intersection method was used to estimate the ultimate lateral loads using the lateral load and displacement curves shown in **Figure 8a**. The relation between the improvement ratio (IR) versus W/D (the ratio of grout width around the piled raft to pile diameter) was plotted as presented in **Figure 8b**. Based on the results, it was found that the lateral resistance improved by about 85.5%, 108%, 129.5%, 152%, and 177% for grouted width of 2D, 4D, 6D, 8D, and 10D, respectively. This means that as the width (w) of the jet grouting increases around the piled raft, the lateral resistance will increase regularly. These findings are in good agreement with those produced by Rollins and Brown [9]. It is important to note that the improvement ratio (IR) increases linearly with the increase in the grouting width in contrast to the nonlinear curves produced from the parametric studies related to the jet grouting depth.

Undoubtedly, utilizing grouting under and around the foundation gives much more lateral resistance than utilizing grouting only under or around the foundation as shown in **Figure 9**, but it must be borne in mind that applying the jet grouting maybe not be possible in all cases like if there are already buildings around the new foundation, in which case the grouting cannot be applied, and the grouting should be applied just below the foundation. As a result, determining the best location and dimensions for the jet grouting necessitates striking a balance between engineering capability and economic efficiency.

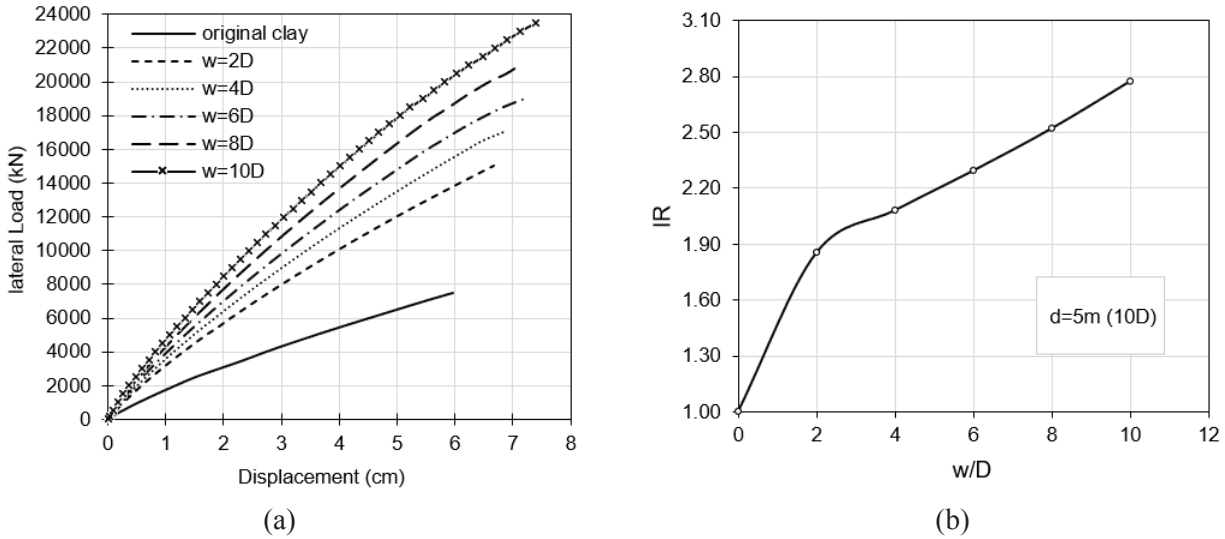

Figure 8. Jet grouting below and around the piled raft with different widths around the piled raft: (a) Lateral load-displacement curves, and (b) improvement ratio versus w/D ratio.

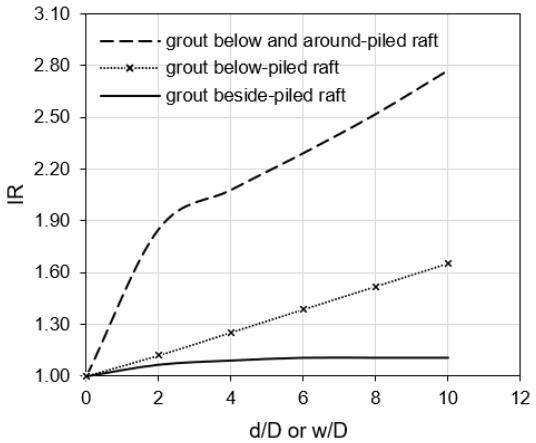

Figure 9. Comparison between different parameters for the jet grouting.

5.4 The effect of jet grouting strips width parallel to the load and perpendicular to the load direction

Jet grouting strips with different widths (w) were used between the piles in this analysis. The strips were applied parallel to the lateral load, as shown in **Figure 5d**, and then perpendicular to the lateral load, as shown in **Figure 5e**. The strips parallel to the load have a length of 14 m, while the strips perpendicular to the load have a length of 12 m. The depth of jet grouting strips (d) has a constant value equal to 3 m (6D). The strips have various widths of 0.5D, D, 1.5D, and 2D (0.25 m, 0.5 m, 0.75 m, and 1 m). The ultimate lateral loads were calculated using load-displacement curves (see **Figure 10**). The relation between the improvement ratio (IR) versus w/D (the ratio between the jet grouting strip width and the pile diameter) is presented in **Figure 11**. The curves show that the lateral resistance enhanced by about 17.5%, 25.5%, 31%, and 35% for strips widths of 0.5D, D, 1.5D, and 2D, respectively in the case of the strips parallel to the load. The lateral resistance was enhanced by about 13.5%, 21.5%, 27.5%, and 30% in the case of the strips perpendicular to the load. According to the results, it can be seen that the lateral resistance of the piled raft increases with increasing the width of the jet grouting strips between the piles. It should also be noted that the strips parallel to the load provide more lateral resistance than the strips perpendicular to the load, as the improvement ratio reaches 1.35 for the grout strips parallel to the load and 1.3 for the grout strips perpendicular to the load at (w/D = 2), as shown in **Figure 11**. This means that, depending on the required lateral resistance, jet grouting strips can be applied between the piles rather than under the entire area of the piled raft.

5.5 The effect of vertical loads on the lateral behavior of piled raft in grouted clay

The piled raft is designed to carry both vertical and horizontal loads, so the lateral response of piled raft must be studied in the presence of vertical loads to represent reality. Numerical analysis was performed on the piled raft subjected to combined loads. In this analysis, the jet grouting was applied at a depth of 5 m (10D) below the piled raft as presented in **Figure 5f**. A separate numerical analysis was performed on the piled raft subjected to pure vertical loads to estimate the ultimate vertical load (V_u). The tangent intersection method [48-50] was used to estimate the ultimate vertical load (V_u). The combined axial and lateral loads were applied in two phases. The vertical loads were applied in the first phase, and then the lateral loads were added in the second phase, while the vertical load remained constant. This loading simulates reality, in which the piles are subjected to vertical loading caused by the weight of the superstructure, followed by the lateral loads that may be caused by wind forces, ship impact, landslides, etc. The values of the applied vertical loads were equal to zero, 0.25 V_u, 0.5 V_u, and 0.75 V_u. The lateral load-displacement curves were plotted as presented in **Figure 12a**. The improvement ratio for lateral resistance of piled raft in the presence of the vertical loads is determined as:

$$IR = \frac{L_{uc} \quad (\text{combined loads})}{L_u \quad (\text{pure lateral loads})} \tag{4}$$

where, (L_{uc}) is the ultimate lateral load when vertical loads are applied and (L_u) is the ultimate lateral load when pure lateral loads are applied. As presented in **Figure 12b**, the relation between (IR) and V/V_u (the ratio of applied vertical loads to ultimate vertical loads) shows that the lateral resistance increased by about 6%, 11%, and 14% at applied vertical loads equal to 0.25 V_u, 0.5 V_u, and 0.75 V_u respectively. This increase is due to the increase in confining stresses in the soil under the raft when the vertical loads are applied, which causes lateral stresses to increase in the soil around the piles. This implies that the presence of vertical loads has a significant effect on the lateral response of the piled raft in grouted clay, whereas the presence of vertical loads increases the lateral load capacity.

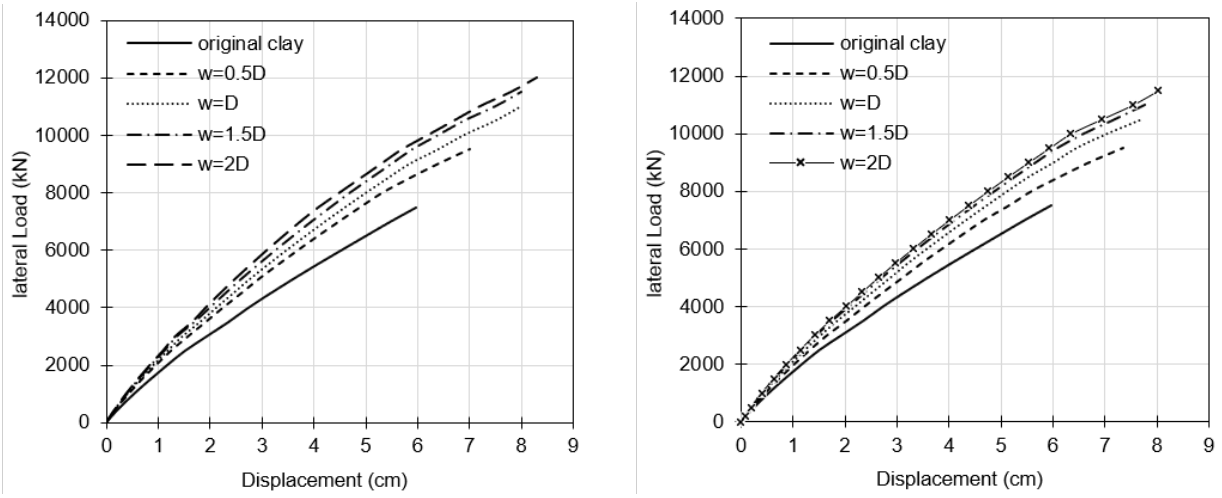

Figure 10. Lateral load-displacement curves for jet grouting strips between the piles: (a) strips parallel to the lateral load, and (b) strips perpendicular to the lateral load.

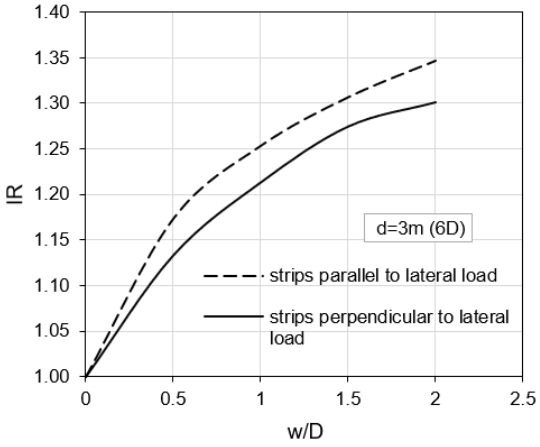

Figure 11. Improvement ratio versus w/D ratio for jet grouting strips.

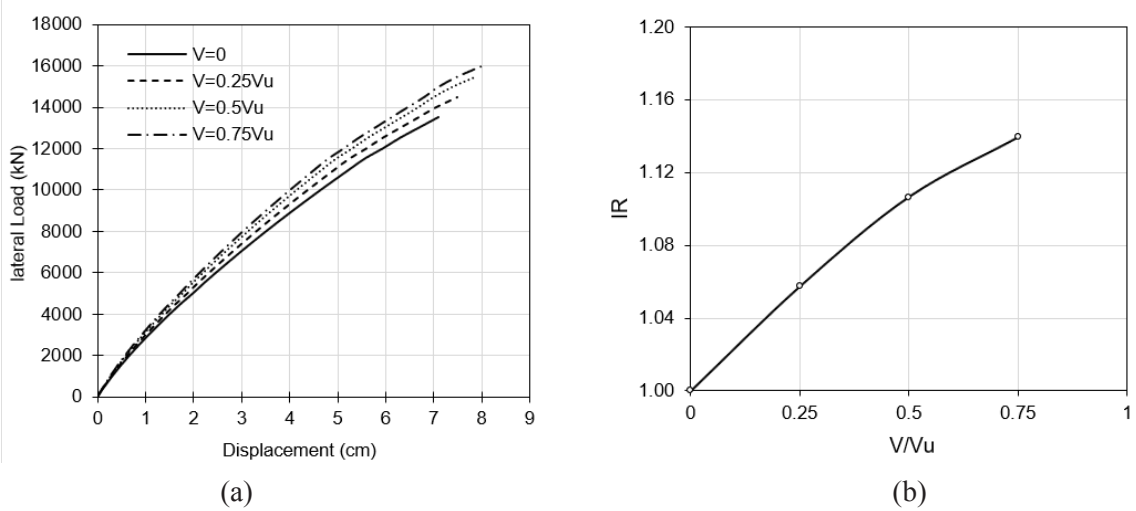

Figure 12. piled raft subjected to combined vertical and horizontal loads in grouted clay soil: (a) Lateral load-displacement curves, and (b) improvement ratio versus V/Vu ratio.

6. Conclusions

In this paper, numerical studies were conducted using PLAXIS 3D software to investigate the lateral behavior of the piled raft in grouted clay soil. The effect of some parameters, such as the width, depth, and location of the jet grouting, as well as the effect of vertical loads, was studied in this analysis. Based on the obtained results from the numerical analysis, the following chief conclusions can be drawn:

1) The upper grouted clay layers (6 to 10 times the diameter of the pile) provide much more lateral resistance relative to the deeper layers.

2) The jet grouting depth below the piled raft foundation has a great effect on increasing the lateral performance, whereas the lateral resistance enhanced by about 65% at a grouted depth of 10 times the diameter of the pile (10D), through the increase in the lateral resistance is limited at grouted depths greater than 10D.

3) Increasing the jet grouting depth adjacent to the piled raft improves the lateral resistance to a depth equal to 6 times the pile's diameter (6D), but the lateral resistance remains constant for grouted depths greater than 6D.

4) Applying the jet grouting below the piled raft gives a much more improvement ratio than applying the jet grouting beside the raft, making it more cost-effective to use jet grouting beneath the foundations.

5) As the grouted width around the piled raft expands, the lateral behavior of the piled raft gradually improves, i.e., the improvement ratio increases linearly, as opposed to the nonlinear curves produced by the related studies to the grouted depth.

6) Utilizing the grout beneath and around the piled raft significantly improves the lateral resistance compared to the grout only under or around the foundations.

7) The greater the width of the jet grouting strips between the piles, the greater the lateral resistance of the piled raft, as the improvement ratio increased by 17.5% to 35% for strips widths of 0.5D to 2D in the case of the strips parallel to the lateral load direction and by 13.5% to 30% for strips width of 0.5D to 2D in the case of the strips perpendicular to the load direction.

8) Using jet grouting strips parallel to the lateral load direction gives more lateral resistance than using jet grouting strips perpendicular to the load direction.

9) The presence of vertical loads has a remarkable effect on improving the lateral performance of the piled raft in improved clay soil, whereas the lateral load capacity increases by about 14% at a vertical load equal to 0.75 V_u.

Conflict of Interest

The authors declare that they have no conflicts of interest.

Funding

There was no funding received to help with the preparation of this manuscript.

References

[1] Rahman, M.M., Karim, M.R., Baki, A.L., et al., 2008. Ultimate lateral load resistance of laterally loaded pile. Deep Foundations on Bored and Auger Piles—BAP V. CRC Press: USA. pp. 167-172.

[2] Sayeed, A., Pk, S., Rahaman, A. (editors), 2012. Model study to improve lateral load resistance of piles in sand using geotextile. Proceedings of the 1st International Conference on Civil Engineering for Sustainable Development; 2021Mar 2-3; Khulna, Bangladesh; p. 6.

[3] Sureshkumar, R., Bharathkumar, R., Mohankumar, L., et al., 2017. Static behaviour of 3×3 pile group in sand under lateral loading. IOP Conference Series: Materials Science and Engineering. 263(3), 032035.

[4] Paulus, P., RahardjoBigman, M., Hutapea. (editors), 2017. Effects of pile lateral movement, pile spacing and pile numbers on laterally loaded group piles. International Conference on Advancement of Pile Technology and Pile Case

Histories; 2017 Sep 25-27; Bali, Indonesia.

[5] Peng, J.R., Rouainia, M., Clarke, B.G., 2010. Finite element analysis of laterally loaded fin piles. Computers & Structures. 88, 1239-1247. DOI: https://doi.org/10.1016/j.compstruc.2010.07.002

[6] Sakr, M., Azzam, W., Wahba, M., 2018. Performance of laterally loaded model finned piles in clay soil. Journal of Engineering Research. 2, 28-36. DOI: https://doi.org/10.21608/erjeng.2018.126015

[7] Abdrabbo, F.M., El Wakil, A.Z., 2016. Laterally loaded helical piles in sand. Alexandria Engineering Journal. 55, 3239-3245. DOI: https://doi.org/10.1016/j.aej.2016.08.020

[8] Abdrabbo, F.M., Gaaver, K.E., Elwakil, A.Z., et al., 2019. Improving lateral capacity of single vertical piles embedded in choesionless soil. International Conference on Advances in Structural and Geotechnical Engineering ICASGE 19; 2019 Mar 25-28; Hurghada, Egypt.

[9] Rollins, K., Brown, D., 2011. Design Guidelines for Increasing the Lateral Resistance of Highway-bridge Pile Foundations by Improving Weak Soils [Internet]. Transportation Research Board. Available from: https://nap.nationalacademies.org/catalog/14574/design-guidelines-for-increasing-the-lateral-resistance-of-highway-bridge-pile-foundations-by-improving-weak-soils

[10] Brown, B.D.A., Morrison, C., Reese, L.C., 1988. Lateral load behaviour of pile group in sand. Journal of Geotechnical Engineering. 114, 1261-1276.

[11] Taghavi, A., Muraleetharan, K.K., Miller, G.A., et al., 2016. Centrifuge modeling of laterally loaded pile groups in improved soft clay. Journal of Geotechnical & Geoenvironmental Engineering. 142, 04015099. DOI: https://doi.org/10.1061/(asce)gt.1943-5606.0001443

[12] Eltaweila, S., Shahien, M.M., Nasr, A.M., et al., 2021. Effect of soil improvement techniques on increasing the lateral resistance of single piles in soft clay (numerical investigation). Geotechnical and Geological Engineering. 39, 4059-4070. DOI: https://doi.org/10.1007/s10706-020-01534-9

[13] Rollins, K.M., Adsero, M.E., Herbst, M.A. (editors), 2010. Ground improvement for increasing lateral pile group resistance. International Conferences on Recent Advances in Geotechnical Earthquake Engineering and Soil Dynamics; 2010 May 26; Missouri University of Science and Technology. Geotechnical Engineering Commons.

[14] Raj, D., Gandhi, S.R., 2004. Improvement of lateral capacity of pile due to compaction of surrounding soil. International Geological Congress: Beijing, China. pp. 382-385.

[15] Bahloul, M.M.M., 2011. Improvement of the behaviour of laterally loaded piles and pile groups in sand. Mathematical Modelling in Civil Engineering. 95-109.

[16] Chiou, J.S., You, T.R., Tsai, C.C., et al., 2017. Performance of laterally loaded piles in improved coal ash deposit. Soils and Foundations. 57, 872-881. DOI: https://doi.org/10.1016/j.sandf.2017.08.019

[17] Kirupakaran, K., Cerato, A.B., Liu, C., et al., 2010. Simulation of a centrifuge model test of pile foundations in CDSM improved soft clays. Geoflorida 2010 Advances in Analysis, Modeling & Design. 41095, 1583-1591. DOI: https://doi.org/10.1061/41095(365)160

[18] Faro, V.P., Consoli, N.C., Schnaid, F., et al., 2015. Field tests on laterally loaded rigid piles in cement treated soils. Journal of Geotechnical & Geoenvironmental Engineering. 141, 06015003. DOI: https://doi.org/10.1061/(asce)gt.1943-5606.0001296

[19] Tariq, K.A., Maki, T., 2019. Use of cement-treated sand to enhance the lateral capacity of pile foundations. International Journal of Physical Modelling in Geotechnics. 19, 221-233. DOI: https://doi.org/10.1680/jphmg.17.00020

[20] He, B., Wang, L.Z., Hong, Y., 2016. Capacity and failure mechanism of laterally loaded jet-grouting reinforced piles: Field and numerical investigation. Science China Technological

Sciences. 59, 763-776.
DOI: https://doi.org/10.1007/s11431-016-6014-5

[21] Adsero, M.E., 2008. Impact of jet grouting on the lateral strength of soil surrounding driven pile foundations [Master's thesis]. Provo: Brigham Young University.

[22] Duan, N., Cheng, Y.P., 2014. A 2D DEM mono-pile model under combined loading condition. Geomechanics from Micro to Macro-tc105 Issmge International Symposium on Geomechanics from Micro to Macro. 1(2), 577-582.

[23] Karthigeyan, S., Ramakrishna, V.V.G.S.T., Rajagopal, K., 2005. Interaction between vertical and lateral loads on the response of piles in soft clays. Proceedings of the 16th International Conference on Soil Mechanics and Geotechnical Engineering: Geotechnology in Harmony with the Global Environment. 4, 1997-2000.

[24] Lu, W., Zhang, G., 2018. Influence mechanism of vertical-horizontal combined loads on the response of a single pile in sand. Soils & Foundations. 58, 1228-1239.
DOI: https://doi.org/10.1016/j.sandf.2018.07.002

[25] Chatterjee, K., Choudhury, D. (editors), 2015. Analytical and numerical approaches to compute the influence of vertical load on lateral response of single pile. The 15th Asian Regional Conference on Soil Mechanics and Geotechnical Engineer ARC 2015 New Innovation Sustainment; 2015 Nov 15; Fukuoka. Fukuoka International Congress Center: Japan. p. 1319-1322.
DOI: https://doi.org/10.3208/jgssp.IND-11

[26] Zhao, C.F., Liu, F.M., Qiu, Z.X., et al., 2015. Study on bearing behavior of a single pile under combined vertical and lateral loads in sand. Yantu Gongcheng Xuebao/Chinese Journal of Geotechnical Engineering. 37(1).
DOI: https://doi.org/10.11779/CJGE201501023

[27] Liang, F., Chen, H., Chen, S., 2012. Influences of axial load on the lateral response of single pile with integral equation method. International Journal for Numerical & Analytical Methods in Geomechanics. 36, 1831-1845.
DOI: https://doi.org/10.1002/nag.1090

[28] Karthigeyan, S., Ramakrishna, V.V.G.S.T., Rajagopal, K., 2006. Influence of vertical load on the lateral response of piles in sand. Computers & Geotechnics. 33, 121-131.
DOI: https://doi.org/10.1016/j.compgeo.2005.12.002

[29] Karthigeyan, S., Ramakrishna, V.V.G.S.T., Rajagopal, K., 2007. Numerical investigation of the effect of vertical load on the lateral response of piles. Journal of Geotechnical & Geoenvironmental Engineering. 133, 512-521.

[30] Hussien, M.N., Tobita, T., Iai, S., et al., 2014. On the influence of vertical loads on the lateral response of pile foundation. Computers & Geotechnics. 55, 392-403.
DOI: https://doi.org/10.1016/j.compgeo.2013.09.022

[31] Deb, P., Pal, S.K., 2019. Numerical analysis of piled raft foundation under combined vertical and lateral loading. Ocean Engineering. 190, 106431.
DOI: https://doi.org/10.1016/j.oceaneng.2019.106431

[32] Deb, P., Pal, S.K., 2021. Influence of combined vertical and lateral loading on lateral response of piled raft foundation. Proceedings of the Indian Geotechnical Conference 2019. Springer: Berlin, Germany. pp. 395-406.
DOI: https://doi.org/10.1007/978-981-33-6346-5_35

[33] Youssef, A.A., Abdel-galil, A.M., Emam, E.A., 2017. Behavior of Soft Clay Soil Reinforced by Floating Granular Piles with Different Materials. Journal of Engineering Research. 4, 25-40.

[34] Galil, A.M.A., Youssef, T.A., Elsalhy, M.I., 2019. Performance of rigid raft foundation resting on soft clay improved by granular piles. International Journal of Scientific & Engineering Research. 10, 992-999.

[35] Miki, G., 1985. Soil improvement by jet grouting. Third International Geotechnical Seminar, Soil Improvement Methods, Singapore, 45-52.

[36] Fang, Y.S., Liao, J.J., Lin, T.K., 1994. Mechanical properties of jet grouted soilcrete. Quarterly Journal of Engineering Geology. 27(3), 257-265.

[37] Melegari, C., Garassino, A., 1997. Seminar on

jet grouting. THL Foundation Equipment Pte Ltd. Singapore.

[38] Stoel, A.E.C. van der Ree, H.J. (editors), 2000. Strength & stiffness parameters of jet grouting columns: Full scale test amsterdam. Proceedings of the International Conference GeoEng2000; 2000 Nov 14-19; Lancaster, USA. Technomic Publishing Company: USA. p.1-6.

[39] Ökmen, Ö., 2003. A study on strength and deformation behavior of soilcrete in jet grout applications. [Master's thesis]. Middle East Technical University: Turkey.

[40] Burke, G.K. (editor), 2004. Jet grouting systems: Advantages and disadvantages. GeoSupport 2004: Innovation and Cooperation in the Geo-Industry; 2004 Jan 29-31; Orlando Florida, US. p. 875-886.

[41] JSG Association, 1986. JSG Method: Technical Information. Tokyo, Japan, 89.

[42] Sönmez, E., 2010. An investigation on the contribution of jet grout strutting to the stability of deep retaining systems by finite element method [Master's thesis]. Turkey: Dokuz Eylül University.

[43] Nishimatsu, Y., 1972. The mechanics of rock cutting. International Journal of Rock Mechanics and Mining Sciences & Geomechanics Abstracts. 9, 261-270.
DOI: https://doi.org/10.1016/b978-0-08-042067-7.50014-3

[44] Bruce, D.A., Bruce, M.E.C. (editors), 2003. The practitioner's guide to deep mixing. Third International Conference on Grouting and Ground Treatment; 2003 Feb 10-12; New Orleans, Louisiana, United States. p. 474-488.

[45] ECP-203, 2007. Egyptian Code of Practice for design and construction of Concrete Structures. Research Center for Housing and Construction, Ministry of Housing, Utilities, cairo.

[46] Bowles, J.E., 1997. Foundation analysis and design international fifth edition. McGraw Hill: New York.

[47] Carter, M., Bentley, S.P., 1991. Correlations of soil properties carter. Pentech: London.

[48] Mansur, C.I., Kaufman, R.I., 1956. Pile tests, low-sill structure, Old River, Louisiana.Transactions of the American Society of Civil Engineers. 82, 1-33.

[49] Trautmann, C.H., Kulhawy, F.H., 1988. Uplift load-displacement behavior of spread foundations. Journal of Geotechnical Engineering. 114, 168-184.

[50] Hung, L.C., Kim, S.R., 2014. Evaluation of undrained bearing capacities of bucket foundations under combined loads. Marine Georesources & Geotechnology. 32, 76-92.
DOI: https://doi.org/10.1080/1064119X.2012.735346

BILINGUAL PUBLISHING GROUP
Pioneer of Global Academics Since 1984

Advances in Geological and Geotechnical Engineering Research
https://journals.bilpubgroup.com/index.php/agger

ARTICLE

Cambrian Explosion: A Complex Analysis of Facts

Narima Kazhenovna Ospanova

Institute of Geology, Earthquake Engineering and Seismology, the National Academy of Tajikistan, 73406, Tajikistan

ABSTRACT

Most researchers attribute the appearance of skeletons to some arbitrarily chosen factors. Many aspects of the phenomenon (the diversity of the composition of the remains, the mass nature of the phenomenon, geological immediacy, the role of geological and biotic factors, etc.) remain unexplained in this case. A comprehensive analysis of facts from different branches of science (lithology, tectonics, chemistry, biology, paleontology) allows us to explain (in addition to the listed) the smallness of Cambrian organisms, the replacement of chemical precipitation by biological, as well as the widespread development of bilaterality, the emergence of new taxa of high rank, and the morphological gap between the Ediacaran and Cambrian faunas. Both abiotic and biotic factors were important: Without the active participation of the living in the precipitation of salts, the formation of skeletons would not have been possible.

Keywords: Biominerагenesis; Skeletonization; Phosphates; Carbonates; Upwelling

1. Introduction

The Vendian-Cambrian boundary is the object of close attention of geologists of various profiles (magmatists, tectonists, metamorphists, geochemists, lithologists, stratigraphers, paleontologists), as well as biologists and astronomers, since one of the greatest events on a biospheric scale is associated with it—the emergence in organisms of the ability to build skeletons. The author first addressed this topic in 1989 [1,2]. Over the past, a lot of new factual data has appeared, which not only can be used as a more extensive and more evidence base to substantiate our point of view, but also allow us to understand such features of the phenomenon as its geological immediacy, the absence of true bilateral symmetry in the Precambrian and the wide its development since the Cambrian, the emergence of new taxa of high rank,

*CORRESPONDING AUTHOR:
Narima Kazhenovna Ospanova, Institute of Geology, Earthquake Engineering and Seismology, the National Academy of Tajikistan, 734063, Tajikistan; Email: ospanova2005@mail.ru

ARTICLE INFO
Received: 1 December 2022 | Revised: 11 January 2023 | Accepted: 13 January 2023 | Published Online: 16 February 2023
DOI: https://doi.org/10.30564/agger.v5i1.5292

CITATION
Ospanova, N.K., 2023. Cambrian Explosion: A Complex Analysis of Facts. Journal of Atmospheric Science Research. 5(1): 40-56. DOI: https://doi.org/10.30564/agger.v5i1.5292

and the presence of a morphological gap between the Ediacaran and Cambrian faunas. In addition, the introduction of the term "biomineragenesis" [3] allows us to consider non-skeletal and skeletal biomineral formation from a broader position—as types of biomineragenesis. Recall that biomineragenesis is *the formation of minerals, carried out in the hydro—and stratisphere with the direct and indirect participation of organisms*. It covers any processes in which mineral compounds are formed because of interaction with the environment of organisms or their metabolic products and decomposition [3]. Below we display the features of biomineragenesis associated with the formation of organic remains, the most widely represented in the geological record—phosphate, carbonate, siliceous and iron. Examples of both skeletal and non-skeletal mineralization are considered.

2. Methodological foundations of the study

Many processes that took place in the past, we cannot observe in the present. Therefore, in such cases, modeling methods are used, the consequences of these processes are studied for recreating the primary situation, and also numerous indirect data are taken into account. To find out the reasons for the appearance of the skeleton at the Vendian-Cambrian boundary, we used the method of complex analysis of facts: we took into account the data of lithology, chemistry, biology and paleontology; analyzed the geological situation, typical for that period of time; the results of laboratory studies on the precipitation of salts by organisms and data on skeletal and non-skeletal biomineral precipitation are involved. The Karatau phosphorite-bearing basin is considered a model for reconstructing the geological situation. The author believes that only a comprehensive accounting of facts can help in solving this problem, while most researchers focus their attention on any single factor, which is methodologically incorrect.

3. Phosphate residues

The first appearance of organogenic formations in the form of stromatolitic phosphate buildups is known from the Lower Proterozoic [4], while the first appearance of skeletons (anabaritids and conodontomorphs) is indicated [5] from the Vendian (Nemakit–Daldyn time). With the beginning of the Cambrian, the number and diversity of organisms with the phosphate skeleton increased dramatically. This is primarily due to the appearance of free (mobile) phosphorus in the water. Ilyin [6] points out that in the Precambrian the mechanism of separating phosphorus from iron and carbon in the sedimentary process did not yet function. He considered upwelling as such a mechanism, in the absence of which the transport of dissolved phosphate to the shelf could not be carried out due to the density stratification of seawater. As a result, phosphorites in the Precambrian are irregularly distributed over different geological formations, dispersed chronologically and not differentiated from iron ores of high-carbon rocks.

In addition, Fedonkin [7] pointed out the stratification of the waters of the Precambrian oceans. He wrote that during most of the Precambrian, the ocean was turbid, the photic zone was narrow, and the thermal gradient was sharp, which contributed to the stratification of the waters. Chaloner and Cocks [8] believed that the progressive increase in oxygen concentration during the Precambrian contributed to the increase in its consumption for the oxidation of iron and manganese, which entered the ocean from hydrothermal systems and fixed phosphorus. Modern chemogenic co-precipitation of phosphorus with ferruginous suspension entering the water column as a part of high-temperature hydrothermal fluids from rift zones (to which points Baturin [9]) can probably be considered as an analog of the named process. He also emphasizes the role of upwellings in the accumulation of phosphorus in shallow water (weak upwelling corresponds to weak phosphate accumulation!). Researchers believe that the upwellings were formed, probably, by the Vendian—Early Cambrian [6], although the first large-scale appearance of upwellings is associated with the Middle Proterozoic—the time of the formation of the continental crust [10]. Kholodov [11] also pointed out that in the early

Proterozoic time the phase differentiation of ore material has extremely weakened. However, "at the beginning of the Paleozoic, the vast, but extremely shallow water bodies of the Proterozoic were replaced by much deeper strait-like seas..., the role of the processes of multiple redeposition and "ripening" of sedimentary material noticeably increased"... [11, p. 21]. Many scientists point out the specificity of the ancient seas, which occupied vast areas, but are characterized by exceptional shallow water. It contributed to their colonization by microorganisms, especially cyanobacterial mats, and the areas in which they functioned, could reach thousands of square kilometers [12].

Thus, the deepening of the seas, hydrodynamic (upwellings and repeated washing of sediments) and tectonic activity contributed to the formation of deposits of phosphate ores proper at the end of the Precambrian—the beginning of the Paleozoic.

The effect of these factors can be seen in the example of the Small Karatau basin, which can be considered a model for recreating the situation on the Vendian-Cambrian boundary [3,13]. Here, tectonic processes and the development of sedimentary faults created a system of uplifts and deflections in the Vendian-Tommot time, and a huge area of shallow water was divided by a series of shoals, bay-bars, and cofferdams into shallow baths-depressions that served as sediment traps [14]. These traps periodically received denser waters containing hydrogen sulfide and increased amounts of silica, phosphorus, and manganese, which precipitated after the oxidation of hydrogen sulfide and diffusion of carbon dioxide into the atmosphere. Upwellings played a transporting role. Their depth of conceiving was 100-250 meters [9]. The disruption (at that time) of the Paleopangea (Rodinia) supercontinent could also contribute to the development of upwellings. The deepening of significant areas of the seabed, which, along with the development of sedimentary faults, could have been facilitated by the Vendian transgression, and the development of anoxic environments there, had an adverse effect on the biota adapted to the conditions of well-aerated shallow water (reduction of the ecological niche), and contributed to the concentration of life in shallow water and increased colonization of shallow areas of the bottom. The indications [15] that the most extensive (Australian-Asian) phosphorite-bearing province was formed in the Vendian-Cambrian epoch can testify to the global nature of the events taking place.

With the advent of organisms with a phosphate skeleton, the latter began to play a leading role in phosphate accumulation. In the accumulation of Vendian-Lower Cambrian phosphorites, bacterial-algal formations still occupy a significant place, but already in the Middle Cambrian phosphorites, grains belong to brachiopods, trilobites, chiolites, and echinoids [6]. Biogenic shell phosphorites of the Ordovician, whose formation epoch was also considered to be global [15], contain shells of lingulids, pteropods, and conodonts [16]. In the Permian Phosphoria Formation, bioclastic varieties are composed mainly of bones, scales, and teeth of fish, as well as foraminifers. In the Cretaceous-Paleogene, there are many grains of foraminifers, coccolithophorids, pteropods, dinoflagellates, and shark teeth are very characteristic. Neogene phosphorites abound in diatom remains [6].

The above review shows that, starting from the end of the Precambrian, organogenic remains played a dominant role in phosphate accumulation. The appearance of phosphate skeletons is associated with the appearance of free (mobile) phosphorus in water, but the onset of phosphatization implies rather high concentrations of it. Upwellings, i.e., flow of deeper waters that rose to the shelf and compensated for the outflow of surface waters caused by offshore winds [17], threw onto the shelf portions of water containing increased amounts of certain elements, and thereby changed the balance of elements in shallow water areas of the seas and contributed to biomineragenesis.

4. Carbonate residues (magnesium and calcium salts)

Calcium and magnesium have always been brought into seawaters in significant quantities [17];

therefore, the significant scale of their utilization by living organisms is not accidental.

Stromatolites are considered to be the oldest carbonate formations of biogenic origin; they appeared on Earth 2.5-3.0 billion years ago and had a predominantly dolomitic composition [18]. Stromatolite structures are layered formations of various shapes attached to the substrate and are the waste products of lower algae with the participation of bacteria, that is, not organic remains proper, but organogenic-sedimentary formations [19]. Thus, the most ancient stromatolites of the Anabar Shield were formed to a large extent by terrigenous material, that is, "mucus films only retained sediment, distributing it in space" [20, p. 280]. The young buildings are composed of carbonates in the form of peculiar columnar-radiant formations, which is evidence of the assimilation of carbonates from the aquatic environment. In addition, the total amount of carbonates in stromatolites is significantly higher than in the surrounding area [21], which indicates not only the capture and binding of sediment, but the active participation of organisms in sedimentation. Previously, the dolomite composition of these formations was considered secondary by most researchers, but then it was proved [20] that dolomite was primary. At present, many researchers are inclined to talk about the purely bacterial nature of stromatolite-forming organisms because blue-greens are classified as bacteria, but others believe [22] that the question of their status remains open. In most cases, scientists prefer to talk about cyanobacterial communities (mats). When referring to the works of the authors, we will adhere to their views on the nature of the organisms under consideration.

The maximum stromatolite formation is noted in the Proterozoic, at the beginning of the Paleozoic it sharply decreases and, fading, passes to us, remaining in rare super saline lagoons. Although part of the carbonates (carbonate rosettes) in stromatolites could be formed as a result of biomass oxidation [23], in general, the content of carbon dioxide in the atmosphere and the alkaline reserve of seawater was higher in ancient times, therefore, additional biochemical dolomite formation was developed much more strongly [17].

Simple calculations based on the MgO and CaO contents in Precambrian and Paleozoic carbonate rocks given in the work of A.B. Ronov and others [24] show that the MgO content in the Paleozoic decreased by 2.08 times compared to the Precambrian (the average value is taken for geosynclines and platforms). If we take into account that the CaO content during the same time increased by 1.26 times, then compared with magnesium oxides, it increased by an average of 2.62 times. The decrease in the amount of magnesium is associated both with the decrease in the content of carbon dioxide in the atmosphere, and with a reduction in the areas of development of igneous rocks of the basic composition, considered [25] as the main sources of income of this element in the sea basins. But it can also be assumed that the duration of the era of stromatolite formation (at least 2.0-2.5 billion years!), in which the deposition of magnesium occupied a prominent place, could affect the subsequent development of the basins.

The decrease in magnesium salts in seawater has led to a decrease in the scale of their utilization by organisms. There are no purely magnesian skeletons, and $MgCO_3$ is present only as an admixture to calcium salts in the skeletons of various representatives of the organic world—echinoderms, brachiopods, decapods, sponges, foraminifers, crimson algae and others; usually its content is 3-5-7%, reaching a maximum in Octocorallia—16.90% of the weight of the mineral part of the skeleton [17].

An even more significant decrease in the content of MgO in carbonate rocks occurred in the Mesozoic, compared with the Paleozoic, it decreased by an average of 4.47 times; against the background of the almost unchanged CaO content (an increase of 1.06 times), the decrease in MgO to CaO is 4.74 times. Fluctuations in the content of Mg/Ca in water even depend on the rate of spreading along the median ridges [26]. Therefore, the relative increase in the calcium content in the waters of the Mesozoic basins occurred not due to additional input, but due to the sharp decrease in the magnesium content in the water, which immediately affected the chemistry of the

skeletons.

Although the calcium content in the Paleozoic seas increased insignificantly on the whole, a combination of a number of factors led to a significant increase in its concentration in certain areas of water bodies. First, carbonate sedimentation is often concentrated in shallow areas of the bottom, since they are characterized by a higher temperature, and with increasing temperature, the intensification of carbonate sedimentation sharply increases [17]. Secondly, the observed general decrease in the amount of carbon dioxide in the atmosphere during this period of time [27] should have contributed to the supersaturation of water with calcium carbonate. The same—and even slightly smaller—amounts of calcium carbonate in water with a low content of CO_2 become, according to the laws of carbonate equilibrium, supersaturate the solution [17]. Thirdly, against the background of the decrease in the content of magnesium in water and the difficulty of its precipitation, the relative content of calcium increased. All this led to the dominance of calcium salts in shallow areas of the seabed on the Vendian-Cambrian boundary.

5. Ferruginous remnants

Ancient organisms (algae, bacteria) precipitated not only carbonates, but also other chemical compounds that were present in the waters of the Precambrian oceans in high concentrations. This pattern was called the rule of the maximum: *The relationship of the most ancient organisms with their surrounding aquatic environment was such that those chemical compounds were deposited, which were present in the environment at the maximum* [1,2]. The compounds that could create high concentrations in water also include iron minerals, the biochemogenic precipitation of which occurred in the form of ferruginous quartzites. Balance calculations showed that, if we proceed from the mass of organic carbon in sedimentary rocks, then this mass should correspond not only to the mass of oxygen in the atmosphere, but also to oxygen, which is part of the sulfates of oceanic waters and iron oxide ores in ferruginous quartzites [28]. Strakhov [17] wrote about the relative deepness of the sedimentation of ferruginous quartzites, but other researchers [11] insist on the extreme shallowness of the conditions for their formation.

Ideas about the shallowness, but the sufficient vastness of the Early Proterozoic seas are well linked with the many kilometers-long rhythmically alternating layers. With a thickness of microlayers of 0.2-2.0 mm, their length can reach almost three hundred kilometers [11]. Without the participation of living organisms in sedimentation, it is difficult to imagine the mechanism of such a uniform distribution of terrigenous material over the entire area. Surely, both biogenic sedimentation and (along with terrigenous input) halmyrolysis (underwater weathering) took place. Stromatolite structures in the absence of hydrogen sulfide contamination [14] or "littering" with clastic material also acquire a sheet form and stretch without interruption for tens and hundreds of meters [19]. The researchers explain the rhythmic structure of ferruginous quartzites by the periodicity of the supply of silica, carbonates, and iron components from the continent and seasonal fluctuations in biogenic phenomena [11]. Algae (Sokolov [29]—ferrobacteria) emitted oxygen waves that passed through the water and entered into chemical reactions with the compounds present in the water. Ferruginous quartzites, the formation of which is dated to the interval of 3.0-1.8 billion years ago (Kholodov [11], 2.6-2.0 billion years), are considered [30] as evidence of the periodic release of oxygen and precipitation of iron by algae. The scale and duration of the period of deposition of ferruginous quartzites indicate that significant masses of iron entered the ancient seas, like many other elements, from the continents as the result of weathering of rocks.

After the precipitation of iron minerals, the seas became largely saturated with oxygen, and the amount of free oxygen in the atmosphere increased. The formation of the Earth's ozone layer is timed to the interval of 2.0-1.8 billion years [30]. The enrichment of the atmosphere with free oxygen is confirmed by the deposition immediately after the formation of iron-bearing formations of red rocks,

which indicates that the processes of chemical weathering of iron minerals on the Earth's surface began, and the limitation of their migration ability. This means that never later could there be similar (to ferruginous quartzites) and comparable in scale iron deposits, which have no analogs in their reserves (and genesis). At present, there is no industrial accumulation of iron ores in open water bodies [31].

Since eukaryotes need an oxygen-rich environment to function, they could not have appeared before the completion of the oxygen revolution [30], that is, earlier than 2.0-1.8 billion years ago. The emergence of eukaryotes after the seas became free of excess iron is consistent with the absence of purely magnetite skeletons, the deposition of which (before the Vendian-Cambrian boundary) occurred mainly by an induced method (with the help of ferrobacteria), and magnetite is usually present in other skeletons only as impurities, for example, in the teeth of some molluscs or in the bones of the temporal region of birds.

Deposits of Precambrian iron ores that arose as a result of biochemogenic sedimentation formed over vast areas (Kursk magnetic anomaly, China, India, Australia, etc.).

6. Siliceous residues

More than 30 deposits of microbiota are known in Precambrian siliceous deposits [32], but the first skeletal remains of silicic composition belonging to *Platysolenites* appear from the end of the Vendian in the Nemakit-Daldyn time [5]. Approximately to the same time level (about 600 million years ago) the first finds of mineralized spicules of fossil sponges are dated [33]. The authors concluded that the first sponges were soft-bodied and probably without spicules. From the beginning of the Cambrian, they become active builders of the siliceous, and in the places of carbonate accumulation, of the carbonate skeleton.

In general, the diversity of siliceous skeletons is relatively small and is significantly inferior in number and variety to calcareous skeletons. The lower prevalence of siliceous skeletons compared to carbonate ones is explained by the maximum diversity of life in areas of well-heated shallow water—the zone of water saturation with calcium salts. Silica, as emphasized by Strakhov [17], is characterized by an "opposite attitude" to temperature conditions and climatic regime compared to calcium carbonate. As the temperature rises, the solubility of SiO_2 increases and the saturation point shifts upward, while the solubility of $CaCO_3$ decreases and the solution becomes saturated or even supersaturated with calcium salts. But the beginning of biomineral precipitation, as mentioned above, requires sufficiently high solution concentrations. The warm waters of shallow, where the diversity of life is maximum, are always undersaturated with silicic acid, therefore, those (probably few) benthic animals began to build the siliceous skeleton that lived at a somewhat greater depth, where the content of calcium salts falls, and the relative content of silicic acid increases. Being located on the shelf below the zones of carbonate accumulation and to a greater extent exposed to the influence of hydrogen sulfide contamination and anoxicity, which were maximally manifested in depressions and in deeper areas of the bottom, the biotopes confined to the zones of silicic accumulation in the late Vendian—early Cambrian were characterized by a naturally lower taxonomic diversity. Strakhov [17] wrote that the majority of siliceous organisms gravitate to high latitudes and cold water, and the majority of calx-producing organisms gravitate to low latitudes and warm water. Modern biogenic silica accumulation is controlled by climatic zonation, circulation of water masses, and upwelling zones [34]. It was also shown that bottom-water temperature acts as a primary control that decreases the relative degree of pore-water saturation with biogenic opal while increasing the silica concentration [35]. The amount of incoming biogenic silica, the rate of its inflow, dissolution and burial, the chemistry of bottom waters and the mineralogical nature of the sediments are also important [35].

A few words should be said about radiolarians, planktonic forms with a siliceous skeleton that appeared at the beginning of the Cambrian and existed throughout the Phanerozoic. The ancestors of

radiolarians led a sedentary lifestyle and had an unstabilized siliceous skeleton. The intensification of the development of pseudopodia contributed to the detachment of radiolarians from the substrate and the transition to free soaring water [36]. The radiolarian skeleton does not play a direct role in hovering and does not serve as an adaptation that arose for life in plankton, but is a heritage of benthic ancestors [37]. Representatives of benthic forms of radiolarians are found in marine sediments deposited in different periods of the Phanerozoic time [34].

The appearance of diatom-like organisms that precipitated silicon is also associated with the beginning of the Cambrian [38]. Their diversity and the duration of the evolutionary path they had traveled by the beginning of the Cambrian era are emphasized wherein. In addition to radiolarians and foraminifers, benthic ancestors are also known in other pelagic groups—ostracods, trilobites, and graptolites—and are also suggested for conodontophorids and nautiloids [39].

7. Chemical and biological aspects of biomineral precipitation

Both laboratory studies and observations in natural conditions have shown that the biological precipitation of salts begins earlier than the chemical one and proceeds more completely. Under laboratory conditions, at the same pH (8.0-8.5) in the control vessels and in the vessels with algae, more rapid precipitation of calcite crystals occurred in the vessels with algae [21]. In the control vessels, precipitation of calcite crystals stopped at pH 8.5-9.0 and there was no subsequent increase in the concentration of hydrogen ions, while in vessels with algae it continued to grow and further precipitation of calcium was noted. Thus, it can be seen that there was a more active and complete precipitation of salts where living organisms were present. It is very important that in vessels with algae, sedimentation began earlier and ended later than the usual precipitation, and subsequent sedimentation required the supply of new portions of the concentrated solution. This explains why the biogenic precipitation of salts accompanies the chemogenic one, and often, with large accumulations of organic matter, replaces it, leaving no place for the latter. For example, starting from the second half of the Ordovician, the volume of biogenic excretions of calcium carbonate in the skeletons of organisms rapidly increased, and starting from the second half of the Paleozoic, this method of transferring carbonate to sediment became predominant [27]. Chemogenic sedimentation of phosphorus in the Phanerozoic seas was also practically absent, and the accumulation of phosphates occurred mainly due to organogenic residues [9].

According to lithological data [27], at the end of the Vendian—beginning of the Cambrian, there was a general decrease in the content of carbon dioxide in the atmosphere and in water, and some cooling of the climate. These factors contributed to a relative increase in the oxygen content in the water, which made possible the colonization of warm-water seas by cold-loving eukaryotes. As a result, life was concentrated on the shallow shelf. With the accumulation of significant masses of living matter, the factor of collective metabolism came into play, which was expressed in a change in the acid-alcalic balance of the environment. The result was a shift in the timing of salt precipitation. The shift in the timing of sedimentation, the temporary "neutralization" of the environment gave the organisms the opportunity and time to adapt to the long-term adverse effects of the environment—a high concentration of salts delivered to shallow water. As the result, salt precipitation came under increasing biological control. According to paleontological data, each group of organisms solved the problem of controlling salt precipitation in its way. So, without the active participation of organisms in salt precipitation, the formation of skeletons would be impossible.

With similar responses, the methods of "neutralization" of the environment by prokaryotes and eukaryotes could be different to one degree or another. Prokaryotes (and algae that appeared at the end of the Proterozoic, that is, eukaryotes) changed the pH of the solution and accelerated the precipitation, releasing oxygen as a side-product, which led to a

change in the oxidative potential of the environment. Actually, the emergence of eukaryotes (presumably 2.0-1.8 billion years ago) is considered as a reaction of organisms to the toxicity of oxygen, which, being the product of metabolism, at the same time affects living systems [7]. The supply of oxygen (to water and the atmosphere) clearly demonstrates the result of the action of collective metabolism. The entry of biogenic oxygen into the hydrosphere at least 3.0 billion years ago is evidenced with sufficient certainty by geochemical studies of sulfur isotopes [29]. The accumulation of oxygen has changed the physicochemical conditions of sedimentogenesis and the evolution of the biosphere.

The result of an unprecedented concentration of eukaryotes in the Vendian-Cambrian shallow waters—zones of maximum chemogenic precipitation of a number of chemical compounds—was an increased release of carbon dioxide into the water, which led to a decrease in the pH of the solution and shifted the timing of the precipitation, which gave the organisms a temporary respite and made it possible to adapt to the increased content of these salts in shallow waters. As the result, salt precipitation came under increasing biological control, and adaptation to high salt content became more and more adjusted. As in the case of the "arthropodization of the world" described by Ponomarenko [40], this process was characterized by positive feedback: *The change of the forms captured by the process of change causes such shifts in the environment that make the change of the forms more and more adaptable.* According to Ponomarenko, the emerging "chain reaction" gives the process an explosive character. The mechanism of adaptation explains the geological immediacy of the mass appearance of skeleton-building forms and, on the other hand, some prolongation of this process over a given period of time (at least 10 million years).

Thus, it is wrong to associate skeletonization only with external factors (high concentrations of phosphorus and calcium in water), which assign a passive role to the living. Without the active participation of organisms in the precipitation of salts, the appearance of skeletons in the morphological and functional diversity known to us would hardly have been possible. The massive accumulation of living matter increased the pressure of organisms not only on the environment, but also on each other. As a result, many forms were forced to switch to sedentarity, and the relative proportion of benthos increased, and there was also a general reduction in size, noted by different researchers for different groups of animals. Former studies [41] attribute a decrease in the size of invertebrates in the Late Vendian to both the extinction of giant forms of the Vendian and the appearance of ancestors of small-sized Cambrian organisms, which intensively ate plankton and impoverished the diet of the Vendian biota. However, one cannot ignore the biological side of the process: the mass accumulation of organisms in limited spaces commonly leads to the unambiguous result – the general decrease in the size of individuals. The decrease in the size of individuals at large concentrations is a consequence of biocenotic (ecosystem) regulation and is directly related to the intensification of competition in the struggle for limited food resources.

Strakhov [42] distinguished four geochemically different groups of elements or substances according to the methods of sedimentation in the final reservoirs of runoff: biogenic, elements of the iron group, microelements, and easily soluble salts (**Figure 1**). In this series, the possibility for chemical precipitation from saturated solutions decreases from left to right; correspondingly, the ability of biological precipitation decreases. Substances of the last group (easily soluble salts) are present only in the form of solutions—they do not precipitate chemically and are not extracted biologically. Thus, those substances were involved in biomineral precipitation, which could give stable chemical components for a certain situation. Simply put, if there is chemical precipitation, then in principle a biological one is also possible.

An important feature of both skeletal and non-skeletal biomineralization is the non-selectivity of sedimentation (lack of initial affinity)—the appearance of calcareous skeletons in places of carbonate accu-

mulation, the confinement of phosphate skeletons to areas with a high content of phosphorus, and siliceous—to areas of siliceous-terrigenous accumulation. In the case of stromatolites (non-skeletal mineralization), there is also a correspondence between the composition of host rocks and the composition of chemical compounds deposited by cyanobacterial communities—dolomite structures were formed in dolomite sequences, limestone structures in rare limestone interlayers, and terrigenous structures in terrigenous sequences [20]. Phosphate buildups formed in areas of phosphate accumulation [4].

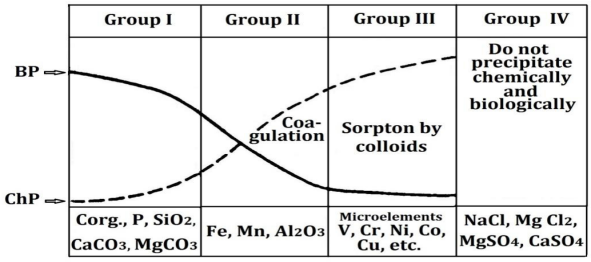

Figure 1. Scheme of sedimentation of dissolved substances in the sea: BP—biological precipitation, ChP—chemical precipitation (Strakhov [42]).

8. Discussion

According to a number of hypotheses, the boundary of the appearance of the skeleton in paleontology can only compete with the problem of the extinction of dinosaurs [43]. It is not necessary to present this extensive material here, not only because of the limited space, but also because it is not the purpose of this work. The maximum possible number of facts related to this topic and allowing to analyze of the problem from different angles objectively is involved. Therefore, we will refer below only to some hypotheses.

One of the hypotheses explains the formation of calcareous skeletons by a significant influx of calcium into the seas due to the erosion of stromatolite structures by the Vendian transgression [44]. This point of view neither takes into account (nor explains) the diversity of the composition of stromatolite structures and the composition of skeletons. For example, many buildings had a dolomite or phosphate composition. It is permissible to ask: Where did the magnesium disappear during the erosion?

Another hypothesis postulates that the reason for the appearance of the skeleton was the "remember" by organisms of the synthesis of biological structures on matrices of abiogenic minerals [43]. This genetic point of view relies on the complementarity of DNA and collagen with an apatite lattice, and amino acids with the calcite lattice. It remains unclear from this hypothesis, why "remember" took place at the Vendian-Cambrian boundary (3.5 billion years after the formation of the structural units of heredity) although there was a lot of phosphorus in the Precambrian seas. It also does not explain the mechanism of formation of the skeleton based on silicon and celestine, the presence of copper, magnetite, and magnesium salts in the skeletons of organisms, and other points. It is obvious that without taking into account the geological factors and analyzing the geological situation in which the formation of the skeletons took place, it is impossible to answer the question of why the skeleton arose precisely at this interval of geological time.

Sokolov [29] believes that oxygenation of the atmosphere and a number of other factors (temperature regime, partial pressure, pH of the environment) could easily reach the critical point at the end of the Vendian, at which the integumentary protein shells of invertebrates were capable of mineralization in various and completely unrelated phylogenetic branches. Organisms protected by hard covers had an increased survival rate in the conditions of a rapidly populated shelf—a zone of moving shallow water, and selection quite naturally fixed this physiological phenomenon. "The decisive role in the Phanerozoic "explosion" was thus the biochemical mechanisms of the Metazoa and selection itself played, and not the mysterious invasion of cryptogenic faunas" [31]. However, not all organisms had hard covers at that time. For example, radiolarians had a metastable siliceous skeleton [37]. The early representatives of this fauna were characterized by a disorderly interweaving of rod-like elements, and the normal spongy

structure was already formed in the Middle and Upper Cambrian [45]. The biochemical factor, which is put at the forefront here, does not take into account the influence of organisms on the environment and the importance of the increased concentration of life in limited spaces, that is, the criticality of the conditions that forced organisms to seek a way out of the situation.

The hypothesis, based on the galactocentric paradigm [46], states that the main epochs of salt and phosphate deposition, as well as the rapid development of life, are due to the fall of comets of the spiral arms of the Galaxy, which are characterized by an increased content of chemical elements of the "calcium peak" with average atomic weights (Na, Mg, P, S, Cl, K, Ca, etc.). These comets reach their greatest abundance in the galactic arms at a distance from the corotation radius of the galaxy (the radius of the circle within which the rotation speeds of the arms and the matter of the galaxy disk coincide) coinciding with the apogalactia (the part of the galactic year corresponding to the "summer") of the solar orbit. Therefore, the main epochs of deposition of phosphorus and salts on the Earth (V/Є, C/P, and K/p) fall on these parts of the orbit (**Figure 2**).

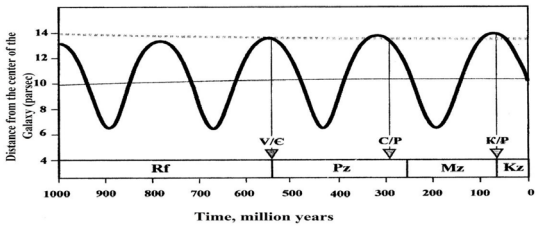

Figure 2. The main periods of accumulation of phosphates and salts [46].

As was shown earlier, the increase in the concentration of calcium salts in the shallow areas of the bottom was due to a combination of climatic and tectonic factors, and not at all to its anomalous supply. At the border of the Paleozoic and Mesozoic, an almost five-fold (in relation to calcium) decrease in the concentration of magnesium occurred, which would hardly have been possible if it had arrived on Earth with a sufficient amount of cometary matter at the beginning of the Permian. The calcium content practically did not change. As for the third main epoch, the general decrease in the carbonate content of precipitation is noted in the late Cretaceous—early Paleogene. In the areas of the outer shelf and the upper part of the continental slope, predominantly carbonate deposits were replaced by black clays [47]. Numerous data contradict this hypothesis. The influence of cosmic dust or the substance of comets and asteroids on the development of terrestrial life has not yet been studied.

Finally, there is a point of view about the extraterrestrial origin of the skeleton. So Achkasov [48] believes that initially the skeletons could have been brought to the Earth with extraterrestrial life when a planetoblem fell on it. He writes: "In the Vendian and Cambrian, out of 90 existing classes, 60 classes of marine multicellular animals suddenly appeared, because life was more developed on the Pacific planet than on Earth". Further: "The skeletal forms of life appeared on Earth suddenly, they have not found predecessors in the Precambrian, and this is a big mystery. The Cambrian is a period that began shortly after the collision of the Earth with planet A1. Therefore, I assume that there was the life of a skeletal form on planet A1" [48]. Firstly, the question arises: Could highly developed life survive in the catastrophic collision of two planetary bodies? Secondly, the correspondence of the composition of the skeletons to the composition of the salts deposited under those conditions indicates the parallel evolution of inert and living matter on our planet. Thirdly, just as the panspermia hypothesis does not solve the problem of the origin of life in the Universe, so this point of view does not answer the question: Where did the skeletal forms on other planets come from?

Many Vendian animals had glide reflection symmetry, which could have arisen from spiral growth [10], while the beginning of the Cambrian is associated with the massive development of bilaterality. Scientists write [49] that there is a significant morphological gap between the Ediacaran fauna and true bilaterians, which remains fundamentally unexplained, and that Ediacaran taxa could not gradually and without significant complications turn into true Bilateria.

The development of bilaterality can be explained by the following reasons. Mass accumulation of organisms in limited areas of shallow water forced many forms to move to sedentarity. The transition to a benthic way of life contributed to the development of various ways of moving along the bottom of the sediment or in the ground. From the pattern established by Shafranovsky [50], which we [51, 52] proposed to call "Shafranovsky's rule", as follows: *everything that moves and grows horizontally or obliquely has bilateral symmetry; anything that grows vertically has radial symmetry.* For example, bottom-crawling larvae may be bilaterally symmetrical, while vertically growing polyps that develop from these larvae are radially symmetrical. So, the low mobility of Ediacaran organisms may explain the lack of true bilateral symmetry in them. The transition to sedentarity at the boundary of the Vendian and Cambrian and the development in connection with this of various modes of the movement were carried out evolutionarily quite quickly, which is quite consistent with the explosive nature of the adaptation process at that time. This explains the lack of a gradual transition between the Vendian forms and true bilateria. As for the rest of the morphological characters, the gap between the Edicarian and Cambrian faunas can be explained by the wide development of the processes of paedomorphosis and neoteny. Earlier, it was said about the small size of the Cambrian organisms. But a decrease in size is achieved, as a rule, due to the reduction of more mature stages of growth, which results in the development of the processes of paedomorphosis and neoteny. The earlier the deviations begin, the greater the difference between the adult stages of the original and derived forms. A radical change in environmental conditions should have contributed to the emergence and development of new phenotypes because the same genotype in different environmental conditions gives different phenotypes.

The few examples given here show that, in principle, any of the factors (both biotic and abiotic), taken in isolation, can be considered as having some potential in trying to explain the causes of skeletal formation. But with this approach, many questions remain unanswered, and on closer examination, it turns out that these factors conflict with the evidence already available.

9. Conclusions

A review of the organogenic remains that are most widely represented in the fossil record, consideration of skeletal and non-skeletal mineralization as types of biominerагenesis, and a comprehensive accounting of geological-lithological, chemical, and biological-paleontological data allow us to draw the following main conclusions.

1) Skeletal formation cannot be explained by any one arbitrarily chosen (at the discretion of the researcher) factor. This approach is methodologically incorrect, so it is natural that the problem is still considered unresolved. This is evidenced by the continuous growth (as science develops) in the number of hypotheses, with which researchers try to explain the phenomenon of the appearance of the skeleton. Only a complex analysis of all available facts, primarily geological and paleontological ones, can pretend to be a conclusive explanation of the reasons for the appearance of the skeleton at the Vendian-Cambrian boundary.

2) In the formation of minerals that make up skeletal and non-skeletal organogenic remains, the most widely represented in the paleontological record, geochemically mobile compounds took part, which tends to accumulate in the final water bodies (seas and oceans) and are capable of chemical precipitation, that is, to give stable for a given environment, chemical compounds.

3) The scale of the processes of non-skeletal and skeletal biomineral deposition depended on the reserves of these substances in marine basins, accumulated over long epochs of geological time, and the degree of water saturation with them.

4) The onset of non-skeletal and skeletal mineralization was provoked by high substance concentrations in seawater. Skeletal biomineral formation, subject to greater biological control of sedimentation, starting in conditions of saturation and supersaturation of water with salts, could then continue in

conditions far from saturation, which indicates the genetic fixation of the trait. Non-skeletal biomineral formation is more dependent on environmental conditions and proceeds only in the presence of sufficiently high concentrations of substances. This explains, on the one hand, the duration of their sedimentation (billions of years), due to the duration of the entry into water bodies of certain chemical compounds, and, on the other hand, a sharp decrease in the scale of deposition with the disappearance or a sharp reduction in the corresponding environmental conditions.

5) Biological precipitation begins earlier than chemical precipitation and ends later. Therefore, in nature, it often leaves no place for chemical precipitation, as also evidenced by a review of organogenic residues. New portions of the saturated solution are required to renew biological precipitation. Respite is important for organisms because the temporary neutralization of adverse environmental influences allows organisms to adapt to them.

6) Mass skeletonization at the Vendian-Cambrian boundary was due to both abiotic and biotic factors. The differentiation of the seabed in-depth, the development of anoxic conditions in the deeper parts of the basins, and the associated reduction in the ecological niche of organisms adapted to the conditions of well-aerated Precambrian shallow waters contributed to the colonization of shallow areas of the seabed and the concentration of life on the shelf, which increased due to the mass migration of eukaryotes from cool to warm waters. But just in these areas, the concentration of some substances or salts was very high during this period of time, up to supersaturation. If the high concentration was the sufficient condition for the start of bio precipitation, then a significant accumulation of masses of living matter was the necessary condition, when the factor of collective metabolism came into action, changing the environment in the direction of adaptive favoring and significantly accelerating the biological control process over salt precipitation. However, these factors in themselves—both high concentrations of substances in water and the large accumulation of organisms in confined spaces—are not optimal for the life of organisms. Therefore, we can conclude that the appearance of skeletons was their response to adverse environmental conditions.

7) The appearance of skeletons in response to adverse environmental influences forces us to deny the goal orientation in the evolution of organisms, that is, skeletons appeared in order to protect against predators or to improve bearing-locomotor functions. These functions are secondary and formed in the process of mutual influence of organisms on each other in changing environmental conditions. Statements such as "the appearance of the skeleton were caused by the need to further increase the activity of organisms" cannot be taken seriously, because cause and consequence are reversed here.

8) The high concentration of phosphorus, silicon and calcium salts in the shallow areas of the seas in the Vendian-Tommotian time was not associated with their anomalously high input into the seas during this period of time, but is explained by a combination of a number of factors that is by the change in the conditions of their sedimentogenesis.

9) The massive nature of skeleton formation is explained by the mass accumulation of organisms in shallow water at the end of the Vendian—beginning of the Cambrian, and skeletonization acts as one of the directions in the evolution of the biosphere. The explosive nature of skeletal formation is associated both with the mass accumulation of various groups of organisms and with the mechanism of adaptation to adverse environmental factors (high salt concentration in shallow water and high density of shelf settlements), when the process of interaction between organisms and the environment acquires the character of positive feedback, multiply accelerating the development of adaptations.

10) The concentration of life on the shelf due to the reduction of shallow bottom areas (the intervention of tectonics and the invasion of cryptogenic fauna) had important and far-reaching consequences:

- an increase in the role of the biotic factor, which made it possible to take the precipitation of some substances or salts under biological control;

- a general decrease in the size of the inhabitants of shallow water, which was carried out due to the removal of more mature stages of development;

- widespread development of bilaterality due to the transition of many forms to sedentarity and the forced adaptation to movement along the bottom, in the near-bottom water layer or the upper sediment layers;

- the emergence of high-ranking taxa, the appearance of which is associated with the processes of paedomorphosis and neoteny;

- the formation of new food chains and new forms of co-evolution due to increased predation and competition.

11) The widespread development of bilaterality indicates that the process of searching for new ways to move along the bottom involved many taxa, and bilaterality was not the privilege of some single hypothetical form designed to play the role of LCBA – the Last Common Bilaterian Ancestor. The absence of true bilateral symmetry in Precambrian organisms is due to their low mobility.

12) Being a component dependent on inert matter and representing a natural product of its evolution, living things also had an impact on the environment on a scale comparable to geological processes.

The analysis of a large amount of factual material allows us to explain all the characteristic features of the "Cambrian explosion". Prior to our studies, the fact that just benthic forms began to build the skeleton was ignored, but scattered data on individual groups, including planktonic ones, confirm this thesis. Benthos is more dependent on external conditions than plankton or nekton, and this also proves the forced transition to the skeletal formation, and not at all the initial readiness of living things to build skeletons. About 98% of the biota in the modern ocean (by a number of the species) is bottom organisms, most of which are inhabitants of the shelf, and only 2% belong to plankton and nekton. Many enzymes and hormones were produced in the Precambrian, and their versatility played a positive role in this critical situation. However, the genetic mechanisms responsible for the formation of the skeleton have been honed and consolidated in parallel with the changes that organisms have undergone.

Conflict of Interest

There is no conflict of interest.

References

[1] *Оспанова, Н.К.,* 1989. К вопросу о минеральной гипотезе происхождения жизни (Russian) [To the question of the mineral hypothesis of the origin of life]. Люберцы. Депонировано в ВИНИТИ. 1-31.

[2] *Оспанова, Н.К.,* 1989. Возникновение скелетов на вендо-кембрийском рубеже (Russian) [The origin of the skeleton at the Vendian-Cambrian boundary]. Доклады Академии наук ТаджССР. 12, 843-846.

[3] *Оспанова, Н.К.,* 1993. Скелетизация как одно из направлений эволюции биосферы (Russian) [Skeletonization as one of the types of the biomineragenesis.]. Материалы Межгосударственного минералогического семинара Минералогия и жизнь. Сыктывкар. 81-82.

[4] *Юдин, Н.И.,* 1996. Дорифейский фосфогенез (Russian) [Doryphean phosphogenesis]. Литология и полезные ископаемые. 3, 321-328.

[5] *Розанов, А.Ю.,* 1989. Эволюция биосферы и скелетизация (Russian) [Evolution of the biosphere and skeletonization]. Осадочная оболочка Земли в пространстве и времени. Стратиграфия и палеонтология: Доклады советских геологов на XXVIII сессии Международного геологического конгресса. Москва: Наука. 18-27.

[6] *Ильин, А.В.,* 1991. К эволюции фосфогенеза: эпохи фосфогенеза и их тектонические предпосылки (Russian) [On the evolution of phosphogenesis: epochs of phosphogenesis and their tectonic background]. Проблемы геологии фосфоритов. Сборник научных трудов. Москва: Наука. 20-27.

[7] *Федонкин, М.А.,* 2004. Происхождение животных в свете ископаемой летописи

и геномики, биосферные последствия экспансии метазоа в венде и кембрии (Russian) [The origin of animals in the light of the fossil record and genomics, the biospheric consequences of the expansion of the Metazoa in the Vendian and the Cambrian]. Биосферные процессы: палеонтология и стратиграфия. Тезисы докладов 50-й сессии Палеонтологического общества при РАН. Санкт-Петербург: СПбГУ. 130-133.

[8] Chaloner, W.G., Cocks, L.R.M., 1989. Biota and palaeoatmospheres. Journal of the Geological Society. (1), 145-146.

[9] *Батурин, Г.Н.,* 1999. Гипотезы фосфогенеза и океанская среда (Russian) [Phosphogenesis hypotheses and the Ocean environment.]. Литология и полезные ископаемые. 5, 451-472.

[10] Fedonkin, A.M., 2003. The Origin of Metazoa in the light of the Proterozoic fossil record. Paleontological Research. 7(1), 9-41.

[11] *Холодов, В.Н.,* 1993. Основы геохимии осадочного процесса. Сообщение 2. Типы бассейнов седиментации и источники питания как факторы дифференциации вещества (Russian) [Fundamentals of geochemistry of the sedimentary process. Message 2. Types of sedimentation basins and food sources as factors of matter differentiation]. Литология и полезные ископаемые. 6, 563-576.

[12] *Розанов, А.Ю., Астафьева, М.М.*, 2007. Бактериальная палеонтология и палеогеография (Russian) [Bacterial paleontology and paleogeography]. Палеонтология, палеобиогеография и палеоэкология: Материалы LIII сессии Палеонтологического о-ва при РАН (Санкт-Петербург, 2-6 апреля 2007 г.). Санкт-Петербург: СПбГУ. 112-113.

[13] *Оспанова, Н.К.,* 2004. Некоторые последствия колонизации дна морскими организмами на границе докембрия и кембрия (Russian) [Some consequences of seabed colonization by marine organisms at the Precambrian-Cambrian boundary]. Биосферные процессы: палеонтология и стратиграфия. Тезисы докладов 50-й сессии Палеонтологического общества при РАН. Санкт-Петербург: СПбГУ. 96-97.

[14] *Холодов, В.Н., Пауль, Р.К.,* 1999. Фации и генезис фосфоритов Каратау. Сообщение 2. Происхождение фосфатных пеллет и общая схема развития томмотского палеоводоёма (Russian) [Facies and genesis of Karatau phosphorites. Message 2. The origin of phosphate pellets and the general scheme of development of the Tommot paleo-reservoir]. Литология и полезные ископаемые. 5, 503-516.

[15] *Соколов, А.С.,* 1991. Основные проблемы фосфатной геологии (Russian) [The main problems of phosphate geology]. Проблемы геологии фосфоритов: Сборник научных трудов. Москва: Наука. 5-15.

[16] *Пауль, Р.К.,* 1999. Циклы фосфатонакопления (на примере Иркутского амфитеатра и Горной Шории) (Russian) [Cycles of phosphate accumulation (on the example of the Irkutsk amphitheater and Gornaya Shoria]. Литология и полезные ископаемые. 1, 12-26.

[17] *Страхов, Н.М.,* 1962. Основы теории литогенеза (Russian) [Fundamentals of the theory of lithogenesis]. Том 2: Закономерности состава и размещения гумидных отложений. Москва: Издательство АН СССР. 1-575.

[18] *Конюшков, К.Н.*, 1978. О строматолитах как продуктах жизнедеятельности низших водорослей (Russian) [On stromatolites as waste products of lower algae]. Вопросы тафономии и палеобиологии. Труды XX сессии Всесоюзного палеонтологического общества. Душанбе: Дониш. 88-94.

[19] *Конюшков, К.Н.*, 1988. Строматолиты докембрия как показатели среды обитания (Russian) [Precambrian stromatolites as indicators of the environment]. Следы жизнедеятельности и динамика среды в древних биотопах. Труды XXX сессии Всесоюзного палеонтологического общества, VII сессия Украинского палеонтологического общества. Киев: Наукова думка. 99-107.

[20] *Кабаньков, В.Я., Голованов, Н.П., Ильченко, Л.Н., et al.,* 1976. О некоторых особенностях эволюции позднедокембрийских водорослей (Russian) [On some features of the evolution of late Precambrian algae]. Пятидесятилетие советской палеонтологии и вопросы систематики древних организмов. Труды XIII и XIV сессий Всесоюзного палеонтологического общества. Ленинград: Наука. С. 272-281.

[21] *Крылов, И.Н., Орлеанский, В.К.,* 1986. Влияние сине-зелёных водорослей на осаждение карбоната кальция (Russian) [Influence of blue-green algae on the precipitation of calcium carbonate.]. Известия АН СССР. Серия геологическая. 5, 63-71.

[22] *Сумина, Е.Л.,* 2004. К вопросу об уровне организации строматолитообразующих цианобактериальных сообществ (Russian) [On the level of organization of stromatolite-forming cyanobacterial communities]. Биосферные процессы: палеонтология и стратиграфия. Тезисы докладов 50-й сессии Палеонтологического общества при РАН. Санкт-Петербург: СПбГУ. 125-127.

[23] Dodd, M.S., Papineau, D., Grenne, T., et al., 2017. Evidence for early life in Earth's oldest hydrothermal vent precipitates. Nature. (543), 60-64.

[24] *Ронов, А.Б., Ярошевский, А.А., Мигдисов, А.А.,* 1990. Химическое строение земной коры и геохимический баланс главных элементов (Russian) [The chemical structure of the earth's crust and the geochemical balance of the main elements]. Москва: Наука.1-182.

[25] *Ронов, А.Б.,* 1993. Стратисфера или осадочная оболочка Земли (количественное исследование) (Russian) [Stratisphere or sedimentary shell of the Earth (quantitative study)]. Москва: Наука. 1-144.

[26] Stanley, S.M., Hardie, L.A., 1998. Secular oscillations in the carbonate mineralogy of reef-building and sediment-producing organisms driven by tectonically forced shifts in seawater chemistry. Palaeogeography, Palaeoclimatology, Palaeoecology. 144(1-2), 3-19.

[27] *Кузнецов, В.Г.,* 2000. Некоторые черты эволюции карбонатонакопления в истории Земли. Сообщение 2. Эволюция доломитообразования и соотношение карбонатонакопления с глобальными геологическими обстановками (Russian) [Some features of the evolution of carbonate accumulation in the history of the Earth. Message 2. Evolution of dolomite formation and correlation of carbonate accumulation with global geological settings]. Литология и полезные ископаемые. 2, 146-156.

[28] *Поярков, Б.В.,* 2000.Основные моменты истории биосферы (Russian) [Basic moments in the history of the biosphere]. Ярославский педагогический вестник. 2. Available from: http://www.uspu.ear.ru/vestnik/uchenue_practicam/11_5/

[29] *Соколов, Б.С.,* 1976. Органический мир Земли на пути к фанерозойской дифференциации (Russian) [The organic world of the Earth on the way to the Phanerozoic differentiation]. (Russian). Вестник Академии наук СССР. 1, 126-143.

[30] *Коуэн, Р.,* 1982. История жизни (Russian) [History of life]. Киев: Наукова думка.1-220.

[31] *Точилин, М.С.,* 1960. Эволюция атмосферы Земли (Russian) [Evolution of the Earth's atmosphere]. Природа. 1, 26-32.

[32] *Головенок, В.К., Конюшков, К.Н.*, 1979. Докембрийские микробиоты в кремнях и их значение для выяснения особенностей древних биосфер (Russian) [Precambrian microbiota in flints and their significance for elucidating the features of ancient biospheres)]. Палеонтология и эволюция биосферы. Тезисы докладов XXV сессии Всесоюзного палеонтологического общества. Ленинград: ПКОП ВСЕГЕИ. 11-12.

[33] Mehl, L., Mueller, J., Mueller, W.E.G., 1998. Molecular Biological and Paleontological Evidence that Eumetazoa, including Porifera

(Sponges), are Monophyletic Origin. Sponge Sciences. Multidisciplinary Perspectives. Tokyo: Springer. 133-156.

[34] *Афанасьева, М.С., Вишневская, В.С.,* 1993. Радиолярии прошлого как индикаторы эволюции кремнисто-карбонатного осадконакопления (Russian) [Radiolarians of the past as indicators of the evolution of siliceous-carbonate sedimentation]. Литология и полезные ископаемые. 5, 52-68.

[35] Varkouhi, Sh., Wells, J., 2020. The relation between temperature and silica benthic exchange rates and implications for near-seabed formation of diagenetic opal. Results in Geophysical Sciences. 1-4, 100002.

[36] *Петрушевская, М.Г.,* 1981.Радиолярии отряда Nasselaria Мирового океана (Russain) [Radiolarians of the order Nasselaria of the World Ocean]. Определители по фауне СССР, издаваемые Зоологическим институтом АН СССР. Ленинград: Наука. 1-406.

[37] *Петрушевская, М.Г.,* 1986. Радиоляриевый анализ (Russian) [Radiolarian analysis]. Ленинград: Наука. 1-200.

[38] *Гапеев, А.П.,* 1995. Кембрийские формы диатомовых водорослей в отложениях Малого Каратау? (Russian) [Cambrian forms of diatoms in the deposits of the Small Karatau?]. Литология и полезные ископаемые. 3, 236-251.

[39] *Каныгин, А.В.,* 2001. Ордовикский феномен взрывной радиации органического мира: экологическая революция в морских экосистемах (Russian) [The Ordovician phenomenon of explosive radiation of the organic world: an ecological revolution in marine ecosystems]. Биоразнообразие в истории Земли. Тезисы докладов XLVII сессии Всесоюзного палеонтологического общества. Санкт-Петербург: СПбГУ. 37-40.

[40] *Пономаренко, А.Г.,* 2001. Артроподизация как основа формирования разнообразия биоты раннего кембрия (Russian) [Arthropodization as a basis for the formation of biota diversity in the Early Cambrian]. Биоразнообразие в истории Земли. Тезисы докладов XLVII сессии Всесоюзного палеонтологического общества. Санкт-Петербург: СПбГУ. 82-83.

[41] *Соколов, Б.С., Федонкин, М.А.,* 1984. Органический мир вендского периода (Russian) [The organic world of the Vendian period]. Палеонтология: Труды 27-го Международного геологического конгресса. Секция С.02. Москва: Наука. 3-8.

[42] *Страхов, Н.М.,* 1960. Основы теории литогенеза (Russian) [Fundamentals of the theory of lithogenesis]. Том 1: Типы литогенеза и их размещение на поверхности Земли. Москва: Издательство АН СССР. 1-212.

[43] *Голубев, С.Н.,* 1987. Минеральные кристаллы внутри организмов и их роль в происхождении жизни (Russian) [Mineral crystals inside organisms and their role in the origin of life]. Журнал общей биологии. Т. XVIII. 6, 784-806.

[44] *Колосов, П.Н.,* 1979. К вопросу о влиянии синезелёных водорослей докембрия на эволюцию раннекембрийских организмов (Russian) [On the issue of the influence of Precambrian blue-green algae on the evolution of early Cambrian organisms]. Палеонтология и эволюция биосферы. Тезисы докладов XXV сессии Всесоюзного палеонтологического общества. Ленинград: ПКОП ВСЕГЕИ. 24-25.

[45] *Обут, О.Т, Данельян, Т.,* 2016. Новые находки радиолярий хорошей сохранности из нижнего кембрия (ботом) Горного Алтая (Russian) [New finds of well-preserved radiolarians from the Lower Cambrian (Botomian) of Gorny Altai]. 100-летие Палеонтологического общества России. Проблемы и перспективы палеонтологических исследований: Материалы LXII сессии Палеонтологического общества при РАН (4-8 апреля 2016 г., Санкт-Петербург). Санкт-Петербург: Издательство ВСЕГЕИ. 127-129.

[46] *Баренбаум, А.А., Литвинова, Т.В.,* 2008. Космогеобиосферное событие на границе венда и кембрия (Russian) [Cosmogeobio-

spheric event at the Vendian-Cambrian boundary]. Геобиосферные события и история органического мира: Материалы LIV сессии Палеонтологического общества при РАН (7-11 апреля 2008 г., Санкт-Петербург). Санкт-Петербург: ООО «Элексис Принт». 18-20.

[47] *Бараш, М.С.,* 2010. Абиотические причины массовой гибели морских организмов на границе мезозоя и кайнозоя (Russian) [Abiotic causes of the mass death of marine organisms at the border of the Mesozoic and Cenozoic]. Материалы LVI сессии Палеонтологического общества при РАН (5-9 апреля 2010 г., Санкт-Петербург). Санкт-Петербург: ООО «ЭлекСис». 23-26.

[48] *Ачкасов, П.В.,* 2006. Происхождение Земли и небесных тел: Сборник статей (Russian) [Origin of the Earth and celestial bodies: Collection of articles]. Новочеркасск: Издательство ООО НПО «Темп». 1-206.

[49] Martynov, A.V., Korshunova, T.A., 2022. Renewed perspectives on the sedentary-pelagic last common bilaterian ancestor. Contributions to Zoology.

[50] *Шафрановский, И.И.,* 1985. Симметрия в природе (2 издание переработанное) (Russian) [Symmetry in the Nature (2nd revised edition)]. Ленинград: Недра. 1-168.

[51] Ospanova, N.K., 2019. The effect of gravity on coral symmetry. Abstracts of 13th International Symposium on Fossil Cnidaria and Porifera. Modena, Italia. Modena: Università di Modena e Reggio Emilia, Dipartimento di Scienze Chimiche e Geologiche. 49.

[52] Ospanova, N.K.,2020. About symmetry of paleozoic corals and its relation with the gravity. Advances in Ecological and Environmental Research. 5(8), 256-269.

BILINGUAL PUBLISHING GROUP
Pioneer of Global Academics Since 1984

Advances in Geological and Geotechnical Engineering Research
https://journals.bilpubgroup.com/index.php/agger

ARTICLE

Petrogenesis and Rb-Sr Isotopic Characteristics of Paleo-Mesoproterozoic Mirgarani Granite Sonbhadra Uttar Pradesh India: Geodynamics Implication for Supercontinent Cycle

***A.P. Dhurandhar*[1*], *Suresh Khirwal*[2], *D.V.L.N. Sastry*[3]**

[1] *Orion Geohytech India, G-10 Bramhaputra Apartment, Aakar Nagar, Katol Road, Nagpur, 440013, India*
[2] *Atomic Minerals Directorate for Exploration & Research, Jamshedpur, 831014, India*
[3] *Atomic Minerals Directorate for Exploration & Research, Hyderabad, 009140, India*

ABSTRACT

The Rb-Sr whole-rock isochron, age 1636 ± 66 Ma of Mirgarani granite, is the one of the oldest granite dated in the northwestern part of the Chhotanagpur Granite Gneiss Complex (CGGC). The initial Sr ratio is 0.715 ± 0.012 (MSWD = 0.11), showing an S-type affinity. The Mirgarani granite has intruded the migmatite complex of the Dudhi Group and forms the Mirgarani formation comparable to the granites of the Bihar Mica Belt around Hazaribagh (1590 ± 30 Ma). The present studies have established the chronostratigraphy of the Dudhi Group and adjoining areas in CGGC. Petrographic and geochemical studies revealed that the granite is enriched in Rb (271 ppm), Pb (77 ppm), Th (25 ppm), and U (33 ppm) and depleted in Sr (95 ppm), Nb (16 ppm), Ba (399 ppm) and Zr (143 ppm) contents as compared to the normal granite. The Mirgarani granite is a peraluminous (A/CNK = 1.23), high potassic (K_2O 6.42%), Calc-Alkalic to Alkali-Calcic {(Na_2O + K_2O) - CaO = 6.29} S-Type granite, a feature supported by the presence of modal garnet and normative corundum (2.68%). The Mirgarani granite is considered to have been formed by the anatexis of a crustal sedimentary protolith at a depth of approximately 30 km with temperatures ranging from 685-700 °C during the Columbian - Nuna Supercontinent.

Keywords: Miragrani granite; Petrogenesis; Isochron dating; Radiogenic heat; Dudhi group; CGGC; Palaeo-Mesoproterozoic; Supercontinents

*CORRESPONDING AUTHOR:
A.P. Dhurandhar, Orion Geohytech India, G-10 Bramhaputra Apartment, Aakar Nagar, Katol Road, Nagpur, 440013, India; Email: apdhurandhar@gmail.com

ARTICLE INFO
Received: 17 November 2022 | Revised: 15 January 2023 | Accepted: 29 January 2023 | Published Online: 21 February 2023
DOI: https://doi.org/10.30564/agger.v5i1.5261

CITATION
Dhurandhar, A.P., Khirwal, S., Sastry, D.V.L.N., 2023. Petrogenesis and Rb-Sr Isotopic Characteristics of Paleo-Mesoproterozoic Mirgarani Granite Sonbhadra Uttar Pradesh India: Geodynamics Implication for Supercontinent Cycle. Advances in Geological and Geotechnical Engineering Research. 6(1): 57-86. DOI: https://doi.org/10.30564/agger.v5i1.5261

1. Introduction

The northwestern part of Chhotanagpur Granite Gneiss Compex (CGGC) occurs in the Sonbhadra district of Uttar Pradesh (U.P.) and, the Mahakoshal group of rock occurs in the north of the CGGC and, is separated by Son Narmada South fault (SNSF). The systematic geological mapping of the rocks of the Son valley and northwestern part of CGGC in the Sonbhadra district of U.P. has been rather scanty and also a cogent account of chrono-stratigraphy is not available. This part of CGGC was named Dudhi Group by Dayal [1], who gave the first geological succession of the Mirzapur and Sonbhadra area. Subsequently, the regional stratigraphic succession based on photo-characteristics was given by Iquballuddin and Moghani [2]. The rocks of the Son valley area have been mapped as the Son Valley greenstone belt by Chaubey and Gupta [3]. The Son Valley rocks have been considered distinct and older than the Bijawars of the type of area and designated as the Mahakoshal Group [4]. The rock formations the south of the Son-Narmada South fault, locally known as the Dudhi Fault, is designated as the Dudhi Group and correlated with the Chhotanagpur Granite Gneiss Complex (CGGC) of Bihar by Yadav [5]. Later, a detailed geological succession for the north and south of the rift valley, along with the account of uranium mineralization in the area, was given by Bhattacharya et al. [6].

The CGGC is an east-west trending mobile belt that belongs to the east Indian Shield and is exposed across the states of Jharkhand, Bihar, West Bengal, and Chhattisgarh, covering an area of over 100,000 km^2 [7,8]. The northern margin of the CGGC is covered by quaternary sediments of Gangetic alluvium (**Figure 1**). Sediments of the Bengal Basin mark the eastern boundary of the terrain and the Mesozoic volcanic of Rajmahal Trap covers the northeastern fringe of the terrain. The western margin of CGGC is dominantly covered by Gondwana deposits of Permian to mid-Cretaceous age [7]. The Mirgarani granite occurs in the northwestern part of the CGGC occurs across the Rihand valley district Sonbhadra (U.P.) and hosts several uranium occurrences. The regional folding and tectonics of CGGC were given based on regional structural and petrographic studies from the central and eastern parts of the Chhotanagpur terrain. Sarkar [9-11] suggested a tentative temporal relationship between the three phases of structural deformation, metamorphism and granite emplacement. Based on reviews of petrological, geochemical, metamorphic, deformational, and geochronological data on the CGGC given as summarised as [12-15]:

M_1 metamorphic stage (around 1870 Ma and followed by the D_1 deformation, > 900 °C at 5-8 kbar pressure).

M_2 metamorphic phase between 1660 Ma and 1270 Ma, the D_2 deformation, 700-800 °C at 5-7 kbar pressure).

M_3 phase was recorded between 1200 Ma and 930 Ma, 700 ± 50 °C at 6.5±1 kbar pressure followed by a D_3-Grenvillian Orogeny.

M_4 event at 870-780 Ma around 750-600 °C and 9-12 kbars pressure, and D_4 and D_5 deformation; D_6 deformation around 850-800 to 600 Ma final cooling.

Mukherjee et al. [16] have divided CGGC into three major tectonostratigraphic classes Domain I, II, and III; Domain I is further divided into two geographic sub-domains viz. Domain IA (south) and IB (north) (**Figure 1a**). These are all based on the geochronological data from the central and eastern parts of CGGC and geomorphic features but they are not based on any tectonic lineament, etc. Present study area and adjoining parts very limited granites/granitoids have been studied so far namely around Harnakachar, Katoli granitoid, Dudhi Granite, Raspahari in CGGC, and In Mahakoshals Tumiya, Jhirgadandi granitoid, and Neruiyadamar granitoids. The present paper discusses new Rb-Sr isotopic data and petrogenesis of Mirgarani granite, regional chronostratigraphy of the area, and provides its implications in the Chhotanagpur granite gneiss complex (CGGC) by synthesizing Rb-Sr isotopic data from the western and northwestern part of CGGC.

2. Regional geology

The Son Valley greenstone belt (Mahakoshal Group) is bounded by the rocks of the Vindhyan

Supergroup in the north and south by the Dudhi and Gondwana group rocks. The northern contact along the Vindhyan is marked by a fault that is an extension of the Jamual-Markundi Fault [17] or the Great Boundary Fault [18]. The Jhirgadandi granite is emplaced along this northern fault in the phyllites of the Turbidite Group (**Figure 1b**). The southern contact of the Son Valley group of rocks (Mahakoshal Group) with the migmatites, granite gneisses, metasediments of the Dudhi group, and rocks of the Gondwana sequence are also faulted and is known as the Dudhi Fault or Son-Narmada South Fault. This contact has several intrusive granitic bodies, namely the Windhyamganj, Harnakachar, Katoli, Bagishoti, Neruiyadamar Granitoid, Tumiya Granitoid, alkali feldspar granite, and alkali epi-syenites of the Sonwani and Kundabhati areas (7, K, S in **Figure 1b**). The regional strike of the Mahakoshal Group greenstone belt is ENE-WSW, with steep dips towards the south. The presence of mesoscopic folds, faults, fractures, crenulations, and puckers of varying trends in Bijawar indicate that these formations were subjected to deformational forces over a considerable period, which caused repeated folds and faults. The Bijawar formations display tight isoclinal to overturned folds plunging at low to moderate angles towards the east and west; these appear to have been developed in the first phase of deformation, which was probably the most active. The subsequent phases of deformation were responsible for the development of subsidiary folds superposed on the first generation of folds [19]. The Mahakoshal Group has been transected by several fractures trending along and across formation trends. Faults trending ENE-WSW and E-W along the Son River north of Renusagar affect the Mahakoshal Group, Dudhi group, and Gondwana. The N-S trending faults have been recorded along the Rihand River. The trend of the Vindhyan Formation varies from NE-SW to ENE-WSW but dips at a low angle towards the north. The Gondwana occurs in a faulted basin. The major tributaries of the Son River and a few major streams follow a straight course with N-S, NW-SE, and NE-SW trends that reflect the underlying fracture trends (**Figure 1b**).

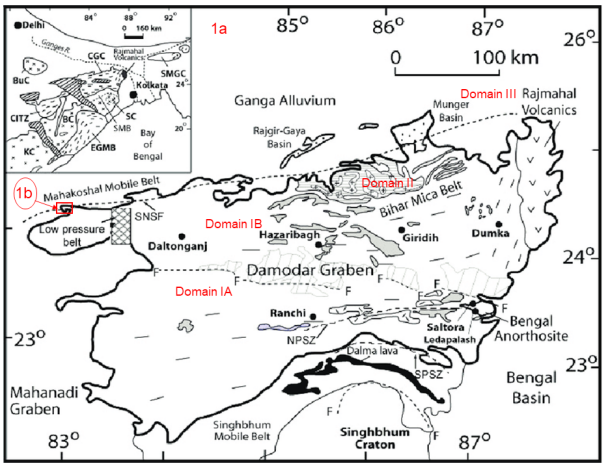

Figure 1a. Regional map showing the Chhotanagapur Granite Gneiss complex and inset India map.

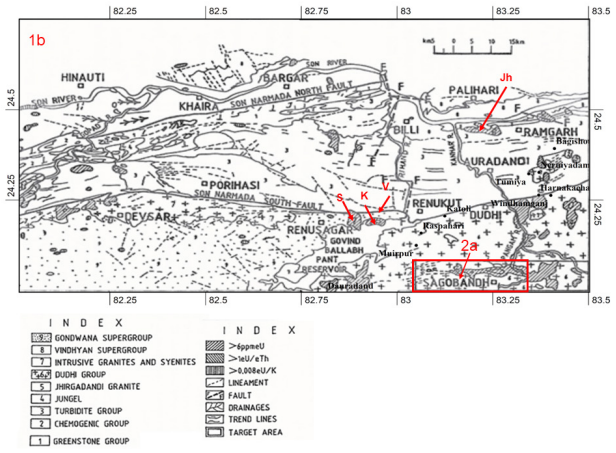

Figure 1b. Regional map of Sonbhadra District showing Mahakoshal and Northwestern part of CGGC, S: Sonwani, K: Kundabhati, V: Vikasnagar; Jh: Jhirgadandi.

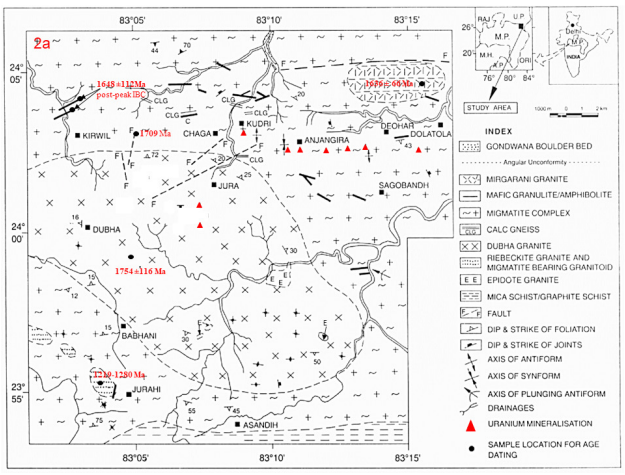

Figure 2a. Geological map of Dudhi Group Sonbhadra District U.P. modified after Dayal 1979 [1].

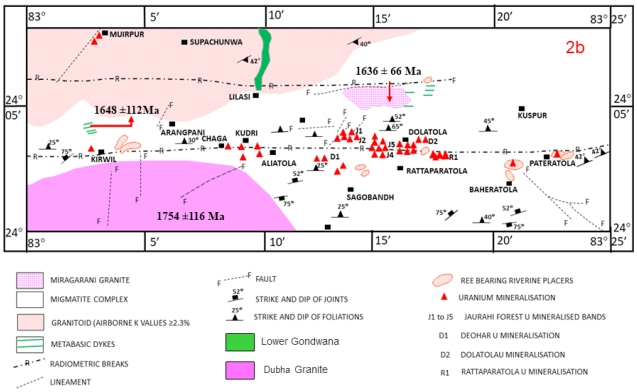

Figure 2b. Detailed geological map of the area around Mirgarani Granite showing uranium occurrences.

3. Geology of the study area

The Mirgarani granite is a high hillock elongated in the E-W direction, forms a domal outcrop in the surrounding low-lying migmatite country rock, and supports a radial drainage pattern. It shows cross-cutting relationships with the meta-basics (amphibolite dykes, calc-granulite, and variants of the migmatite complex), thereby showing intrusive relationships with the migmatite complex (**Figures 2a and 2b**) of the Dudhi Group. Three sets of lineaments were observed: NE-SW, ENE-WSW, and east-west. The migmatite complex hosts several uranium occurrences in Anjangira-Deohar and north of Sagobandh village (**Figure 2a**) [20-23]. The Dudhi Group unconformably overlies the Archean basement and starts with transition sediments with oligomictic quartz pebble meta conglomerates overlaid by Metamorphites, Migmatite Complex, and younger intrusive granites, of various ages Mafic Granulites, and syenites. The migmatite complex consists of palaeosols, mesosomes, biotite melanosomes, stromatic migmatite, pegmatoid, granitoid leucotomies, concordant and discordant bodies of amphibolites, mafic granulites with bands calc-silicate rocks and colonies. Besides these, the mappable variants of granite present in the area are the biotite-hornblende granite of Dubha, magnetite-bearing granitoid, and riebeckite granite of Jaurahi, steno-granites of Mirgarani hillock, and a few outcrops of epidote granite. The mica schist and graphite schist crops south of Asandih (**Figure 2a**). The youngest rocks in the area are Lower Gondwana Sediments with Faulted/unconformity contacts with the Dudhi group of rocks. The area has undergone medium to high-grade regional metamorphism reaching up to upper amphibolite to granulite grade, and a large part of the area belongs to sillimanite—orthoclase isograd. The chronostratigraphic succession of the area is provided in **Table 1**.

Petrography

The Mirgarani granite is leucocratic fine-to medium-grained greyish and pinkish. Under the microscope, it shows a hypidiomorphic granular texture with myrmekitic growth. In some places, it exhibits gneissosity due to parallel alignments of biotite flacks. The essential minerals are potash feldspars (orthoclase, string perthite), quartz, and plagioclase feldspars of albite-oligoclase composition. Biotite and garnet are the chief accessory minerals with minor zircon, apatite, and opaque minerals, such as Ti-magnetite and ilmenite. Medium-sized porphyroblasts of potash feldspars containing inclusions of rounded quartz, albite-oligoclase feldspars, myrmakites, and biotite are suggestive of potash metasomatism. Pink-colored pyrope-almandine garnet was formed at the expense of biotite. The bending of biotite flakes and plagioclase lamellae and the fracturing of quartz and garnet indicate mild stress effects. Mineralogical alterations are of very low intensity and include a slightly cloudy appearance in plagioclase feldspars, saussiritisation in plagioclase feldspar, dendritic growth in biotite, and occasional martitisation in magnetite. Volumetric percentages of modal mineralogy (**Table 2**) and their plots in the QAP diagram of Streckeissens [25] classify Mirgarani granite as Syeno-granites; only three samples fall in the Alkali feldspar granite field (**Figure 3**).

Table 1. Chronostratigraphy of Dudhi Group.

Period	Group	Formation	Lithology
Recent			Alluvium
Permo-Carboniferous (Lower Gondwana)			Lower Gondwana Sediments
~~Fault /Unconformity~~~~~~~~~~~~~~~~~~~~~~~~~~~~~~~~			
Neoproterozoic			Syenites (900 Ma) Alkali feldspar granite Sonwani and Kundabhati (1292 Ma) [97]
Mesoproterozoic 1400-1600 Ma	Dudhi	Intrusive Granites	Tourmaline granite Leucogranite garnetiferous granite and Riebeckite Granites of the Jaurahi Area (1219-1280 Ma) [74]
			Dudhi Granite 1576 ± 76 Ma [75]
Palaeoproterozoic>1600 Ma			Mirgarani Granite 1636 ± 66 Ma
			Kirwil-Sagobabdh Mafic Granulite 1648 ± 112 Ma (post-peak isobaric cooling) [23]
			Harnakachar granitoid 1710 Ma [81]
			Vikasnagar Granite 1717 Ma, [97]
			Rihand Granite 1731 ± 36 Ma
			Katoli granitoid 1730 Ma [81]
			Raspahari Granitoid ca. 1750 Ma [81]
			Dubha Granite 1754 ± 116 Ma [22]
			Muirpur Granite Gniesses 1709 ± 102 Ma [75]
		Migmatite Complex 1787 ± 72 Ma [24]	Quartz Veins
			Quartz Microclene Viens
			Pegmatoid Leucosome Mobilizates (PLM)
			Granitoid Leucosome Mobilizates (GLM)
			Biotite Melanosomes
			Migmatite Mobilizate complex Palaeosomes and Mesosomes (PS, MS)
			Metamorphosed and Ultrametamorphosed Transition Sediments (TS)
		Metamorphites	Metamorphosed and Ultrametamorphosed Transition Sediments (TS)
~~Unconformity~~~~~~~~~~~~~~~~~~~~~~~~~~~~~~~~			
			Transition Sediments with Oligomictic quartz pebble meta-conglomerates (Dauradand area)
~~Fault / Unconformity~~~~~~~~~~~~~~~~~~~~~~~~~~~~~~~~			
Archean ~2600 Ma			Augen gneiss, porphyritic granite, granite gneiss, Amphibolites, banded ferruginous quartzite, Hornblende schist, dolomites, graphite schists, pyroxene granulite, leptinites, and calc-silicate rocks.

Modified after Dhurandhar and Saxena (1996) [20].

Table 2. Modal mineralogy on Mirgarani granite.

Minerals	**MR/1**	**MR/2**	**MR/3**	**MR/4**	**MR/5**	**MR/6**	**MR/7**	**MR/8**
K-Feldspar	49.2	53.4	46.6	53.7	45.4	50.7	53.1	58.4
Ab-Oligoclase	10.2	11.6	7.7	18.3	18.3	7.0	8.4	9.7
Quartz	35.2	27.4	33.7	20.8	22.1	30.9	33	25.4
Biotite	2.4	4.7	1.6	3.8	4.7	10.4	4.3	4.5
Garnet	2.4	2.1	9.3	3	2.8	0.4	0.8	1.5
Opaques	0.2	0.6	1	0.3	0.6			
Others	0.4	0.1	0.1	0.1	0.5	0.3	0.1	0.1

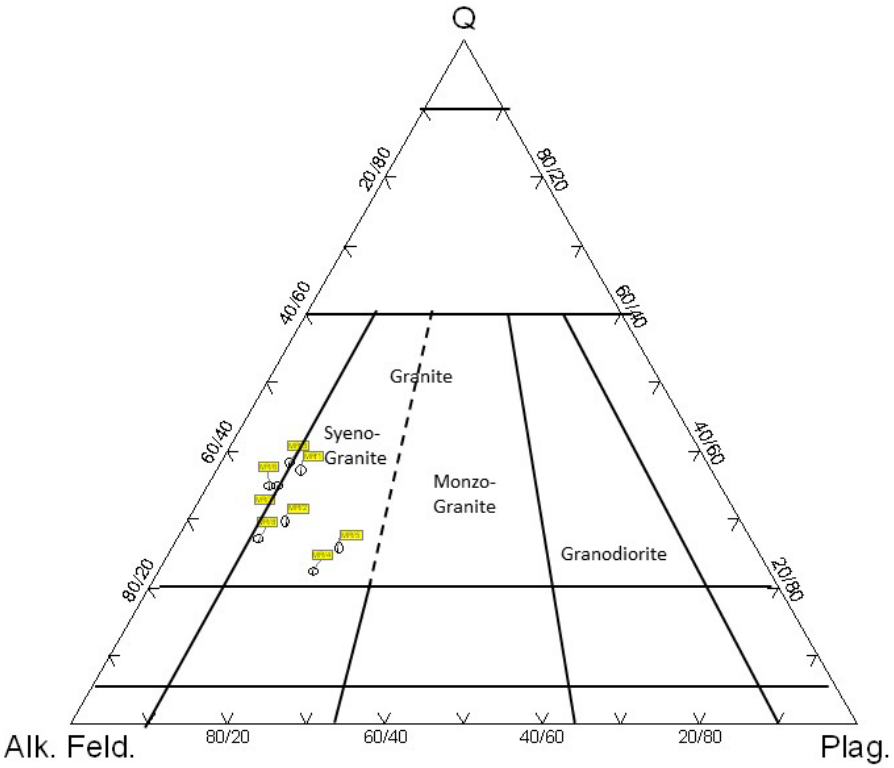

Figure 3. Modal QAP Diagram after Strieckesens (1976) [25] for Mirgarani Granite. Fields 0 Quartzolite, 1 Quartz rich Granitoid, 2 Alkali Feldspar Granite, 3 Granite, 4 Granodiorite, 5 Tonalite, 6 Quartz alkali feldspar Syenite, 7 Quartz Syenite, 8 Quartz Monzonite, 9 Monzodiaorite Monzogabbro, 10 Quartz Diorite Quartz Gabbro, Quartz Anorthosite, 11 Alkali Feldsapr Syenite, 12 Syenite, 13 Monzonite, 14 Foid bearing Monzo diorite monzo gabbro, 15 Diorite, Gabbro Anorthosite.

4. Sampling and analytical techniques

The bulk samples were cleaned, broken, and crushed using a jaw crusher. After quartering and coning, a representative sample was ground to -200 mesh in a shatter box for whole-rock isotopic analysis. One set of samples was analyzed for major, mi-

nor, and trace elements by the wavelength dispersive X-ray fluorescence method using international standards as reference USGS, INRT IGI, RIAP, namely: G1, G2, GSP1, GS-N, SG-1a, SG2, and SG3. The accuracy of the analysis of relative analytical uncertainties is as follows: Si, Al (< 1%), Fe, Mg, Ca (1%-2%), Ti, Na, K (3%-5%), P, and other trace elements (£ 6%). The samples were digested using concentrated HF and HNO_3 in Teflon digestion bombs at 130 °C for 48 h. This was followed by dissolution in HCl acid (HCl). Separation of Rb and Sr from dissolved rock solutions was carried out by ion-exchange chromatography using an AG 50WX12 cation exchange resin in a clean lab under laminar flow. Quantitative estimation of these elements was performed by spiking a known amount of a mixed ^{87}Rb-^{84}Sr tracer, before decomposition. The Rb and Sr isotopic compositions were analyzed using conventional mass spectrometric isotopic dilution techniques with a fully automated, multi-collector thermal ionization mass spectrometer model VG-354. Rb and Sr were loaded as chloride and nitrate, respectively, on Ta ribbon single filament beads with a 1 µL drop of 1N H_3PO_4. The ^{87}Rb and ^{87}Sr tracers used to determine Rb and Sr were calibrated against gravimetrically prepared J. M. salts. Appropriate fractionation corrections were applied to improve accuracy. Based on the replicate analysis, the errors at the 2σ level were 2% for $^{87}Rb/^{86}Sr$ and 0.05% for $^{87}Sr/^{86}Sr$. The mean value for ($^{87}Sr/^{86}Sr$) ratio of the SRM-987 standard was 0.710241 ± 23 (N = 15). Excel plugin Isoplot 3.7 software [26] was used to calculate the slope and intercept of the isochrons. The errors in age and initial Sr ratios quoted here are two standard deviations. More information on the age-dating analytical processes can be found elsewhere [27].

5. Geochemistry

The chemical composition of the Mirgarani granite is presented in **Table 3**. In general, Mirgarani granite shows SiO_2 67.39%-71.9%, TiO_2 0.12 to 0.43%, Al_2O_3 13.46%-14.32%, CaO 1.15%-1.6%, MgO 0.12%-0.36%, FeO 0.97%-1.91%, Fe_2O_3 0.97%-1.91%, MnO 0.03%-0.05%, K_2O 6.02%-6.96%, Na_2O 0.75% to 1.53% and P_2O_5 0.06%. LI 25.29-26.97, DI 75.44-85.74, and FI vary from 83.93-86.99. The Mirgarani granite is enriched in K_2O, FeO, Rb (271 ppm), Pb (77 ppm), Th (25 ppm), U (33 ppm), Cr (27 ppm), Ni (26 ppm), and Co (8 ppm) and depleted in Sr (95), Nb (16 ppm), Ba (399 ppm), and Zr (143 ppm) as compared to the normal granite [28] and continental crust [29]. SiO_2 showed a positive correlation with Al_2O_3, Na_2O, CaO, Larsen's index (LI), Cr, Ni, Ge, As, Sr, Pb, Th, and U and negative correlations with TiO_2, FeO (T), MgO, MnO, K_2O, DI, FI, Rb, Zr, and Nb. On chondrite-normalized multi-element plots (**Figure 4a**), the Mirgarani granite show relative enrichments in Rb, Ba, Th, U, K, Nb, Ce, Sr, Zr, and, with pronounced negative P, and Ti anomalies [30]. The same patterns are shown in primitive mantle normalized plots showing depletion in P and Ti and enrichment in all other elements (**Figure 4b**) [31]. Their multi-element patterns are quite similar to S-Type plutons, although the elemental abundances are variable over a large range from 1.1 to hundreds of times the normalizing values and, likely reflecting source heterogeneities. The Mirgarani granite is peraluminous with A/CNK = 1.17 – 1.31 (average 1.23) and A/NK varies from 1.53 to 1.66 with an average of 1.58 (**Figure 5a**) Shand's index diagram [32]. Agpaitic Index (AI) varies from 0.60 to 0.66 with an average of 0.64. Mirgarani granite is high potassic (K_2O = 6.42%) and has high silica (SiO_2 70.69% avg.), Low Calcic (CaO 1.33 avg.), and magnesium #Mg. 4.22 (**Table 3**) and bearing S-type alkali granite (**Figure 5b**). The S-type feature is further supported by the presence of modal garnet normative corundum 2.52% (**Table 3**) and also by the ACF diagram (**Figure 5c**), where all samples plot in the S-type field. Mirgarani Granites have Low Na_2O content (1.15% avg.), CaO (1.33% avg.), and Sr (95 ppm avg.) contents, which are lost during the conversion of feldspar to clay minerals by weathering and are therefore low in pelitic rocks. Sodium was removed from the solution along with Ca, Sr, and Pb. The Mirgarani Granite also has high Ni, Co, and Cr contents.

Table 3. Geochemical data on Mirgarani Granite showing Major oxides in wt%, trace elements in ppm and HPU in mWm^{-3}.

Oxides	**MR/1**	**MR/2**	**MR/3**	**MR/4**	**MR/5**	**MR/6**	**MR/7**	**MR/8**	**Crust2**	**Granite1**
SiO_2	71.9	71.05	71.26	71.43	69.9	71.74	70.81	67.39	64.2	72.08
TiO_2	0.12	0.26	0.21	0.36	0.43	0.22	0.23	0.29	0.8	0.37
Al_2O_3	14.32	14.1	13.6	13.46	14.03	13.66	13.94	13.57	14.1	13.86
$FeO^{(T)}$	1.93	2.82	2.2	3.11	3.81	2.36	2.43	2.62	6.8	2.44
MgO	0.12	0.22	0.18	0.3	0.36	0.2	0.21	0.19	3.5	0.52
MnO	0.03	0.04	0.03	0.05	0.05	0.04	0.04	0.19	0.12	0.06
CaO	1.38	1.42	1.19	1.39	1.6	1.28	1.26	0.04	4.9	1.33
Na_2O	1.53	1.29	1.35	0.89	0.92	1.3	1.14	1.15	3.1	3.08
K_2O	6.35	6.36	6.25	6.87	6.96	6.1	6.02	6.94	2.3	5.46
P_2O_5	0.01	0.01	0.01	0.01	0.01	0.01	0.01	0.01	0.18	0.18
Total	97.69	97.57	96.28	97.87	98.07	96.91	96.09	92.39	100.00	99.38
Calculated Numbers										
A/CNK	1.2	1.22	1.22	1.24	1.17	1.25	1.31	1.25		
A/NK	1.53	1.57	1.54	1.61	1.55	1.59	1.66	1.55		
AI.	0.66	0.64	0.66	0.66	0.64	0.64	0.60	0.64	0.54	0.79
K/Rb	250.98	214.59	199.52	162.68	191.92	187.52	192.92	193.30	276.70	302.16
Mg/(Mg+Fe)	0.93	0.91	0.90	0.89	0.89	0.90	0.90	0.91	0.29	0.14
B	37.67	55.10	42.99	60.81	74.49	46.11	47.48	51.22		
Solidification Index	12.33	11.94	10.83	11.34	12.04	11.59	11.61	10.03	28.65	10.80
LI	26.97	26.38	26.51	25.38	25.29	26.25	25.72	25.44	25.20	25.20
DI	77.68	76.31	85.74	75.44	81.54	85.64	84.77	84.27		
FI	85.84	84.34	86.46	83.93	83.12	86.05	85.04	86.99	86.52	86.52
HPU	22.78	14.90	14.31	2.38	5.25	13.25	11.36	2.99	1.00	2.89
Trace elements in ppm										
Sc	6	6	6	6	6	6	5	6	19	5
V	18	21	6	17	25	17	11	6	128	20
Cr	32	32	24	27	28	24	25	15	92	4
Co	2.75	9	5	14	15	8	7	23	24	1
Ni	43	27	24	19	27	19	23	7	46	0.5
Cu	28	27	22	29	23	19	25	23	38	10
Zn	32	37	15	20	41	21	32	14	81	1.5
Ge	7	6	6	6	5	6	6	26	1.5	1.3
As	14	10	11	5	6	8	10	6	3.1	1.5
Rb	210	246	260	325	301	270	259	8	69	150
Sr	94	103	89	94	110	97	93	298	285	285
Y	46	41	44	32	32	39	41	77	17.5	40
Zr	104	116	117	170	247	115	126	43	175	180
Nb	17	15	15	15	16	12	18	145	11	20

Table 3 continued

Oxides	MR/1	MR/2	MR/3	MR/4	MR/5	MR/6	MR/7	MR/8	Crust2	Granite1
Sn	3	8	5	8	3	9	6	3	1.5	1.5
Ba	194	377	236	658	615	413	344	22	614	600
Ce	91	3	14	3	3	24	17	3	60	100
Pb	93	83	89	69	56	85	74	358	15	20
Th	30	37	25	16	22	25	28	64	7.1	17
U	77	45	46	2.75	12	42	34	16	1.2	4.8
Th/U	0.39	0.82	0.54	5.82	1.83	0.60	0.82	4.00	5.92	3.54
Rb/Sr	2.23	2.39	2.92	3.46	2.74	2.78	2.78	3.87	0.24	0.53
Rb/Zr	2.02	2.12	2.22	1.91	1.22	2.35	2.06	2.06	0.39	0.83
Rb/Ba	1.08	0.65	1.10	0.49	0.49	0.65	0.75	0.83	0.11	0.25
R1	2706.35	2705.58	2741.60	2743.58	2589.79	2821.86	2833.32	2522.68		
R2	434.50	439.43	403.02	427.63	464.26	414.82	418.67	398.65		
CIPW Normative mineralogy										
Q	35.26	35.48	36.41	36.22	33.57	37.50	37.83	33.41	28.35	30.84
C	2.43	2.52	2.46	2.05	2.09	2.60	3.27	2.75		0.90
Or	37.53	37.59	36.94	40.60	41.13	36.05	35.58	41.01	13.59	32.27
Ab	12.95	10.92	11.42	7.53	7.78	11.00	9.65	6.35	26.23	26.06
An	6.81	7.01	5.87	6.86	7.90	6.31	6.21	5.67	17.76	5.42
Di									0.65	
Hy	1.07	1.50	1.17	1.66	2.01	1.30	1.34	1.30		0.15
Mt	1.40	2.04	1.59	2.25	2.76	1.71	1.76	1.90	9.11	0.62
Il	0.23	0.49	0.40	0.68	0.82	0.42	0.44	0.55	1.52	0.70
Wollastonite (Wo)									1.90	
Hematite (Hm)									0.52	2.01
Hypersthene en	0.07	0.10	0.07	0.12	0.12	0.10	0.10	0.10		0.15
Hypersthene fs	1.00	1.40	1.10	1.53	1.88	1.20	1.24	1.20		

Note: [1]Granite composition [28], [2]Bulk Continental Crust composition [29].

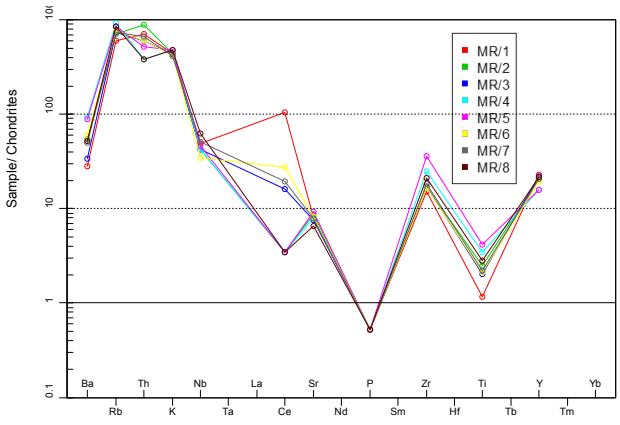

Figure 4a. Trace-element spider diagram for Mirgarani Granite Chondrite normalized after Thompson [30].

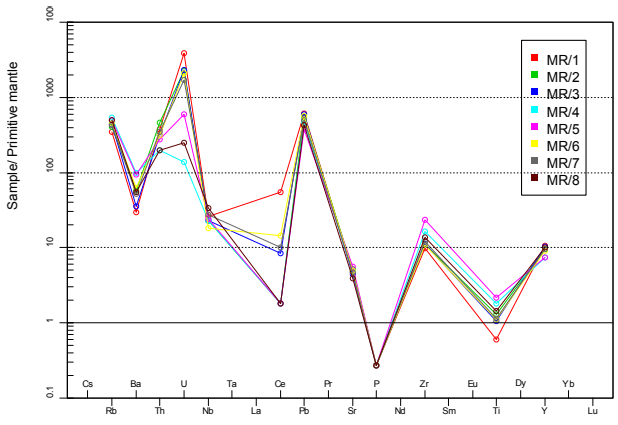

Figure 4b. Extended trace-element spider diagram for Mirgarani Granite Upper Crust normalized after MacDonough and Sun [31].

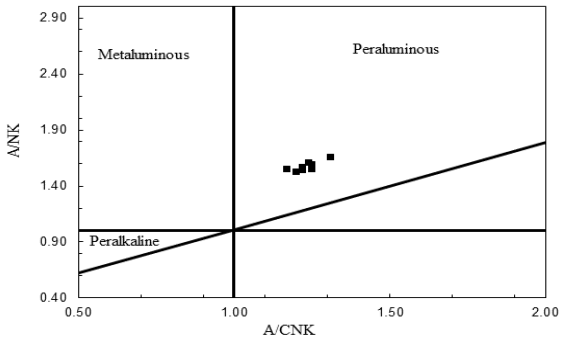

Figure 5a. A/CNK vs A/NK for Mirgarani Granite showing peraluminous character in Shands Index diagram modified after Maniar and Piccoli [32].

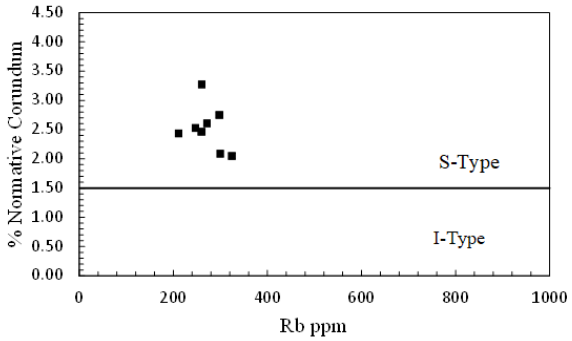

Figure 5b. Rb Vs Normative Corundum Plot for Mirgarani granite occupying S-type field.

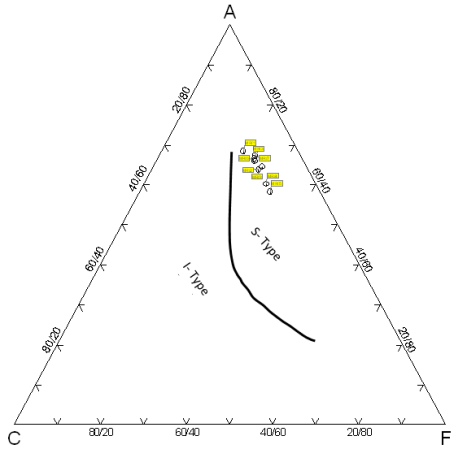

Figure 5c. ACF diagram showing S Type characteristics of Mirgarani Granite.

6. Petrogenesis

Mirgarani Granite is a Calc-Alkali to Alkali-Calcic granite with ($Na_2O + K_2O$)-CaO values varying from 5.9-6.54 with an average of 6.29. The total alkali ($Na_2O + K_2O$) versus SiO_2 TAS diagram (**Figure 6**) [33] shows that the Mirgarani granite is a subalkalic granite. The $Na_2O + K_2O + Fe_2O_3 + MgO + TiO_2$ vs. $(Na_2O + K_2O)/(Fe_2O_3 + MgO + TiO_2)$ plot (**Figures 7a, 7b**) [34] shows evidence of a melt of crustal metagraywackes magma source. The experiments indicate that the meta-graywackes contain biotite and plagioclase but no aluminosilicates. The physical conditions of formation correspond to magmas formed by hybridization in the continental crust of normal thickness at depths of 30 km or less (**Figures 7a, 7b**) [34]. The plotting of MG on the Rb-Sr crustal thickness grid [35] suggests that the crust was thicker than 30 km during the evolution of Mirgarani granite (**Figure 8**).

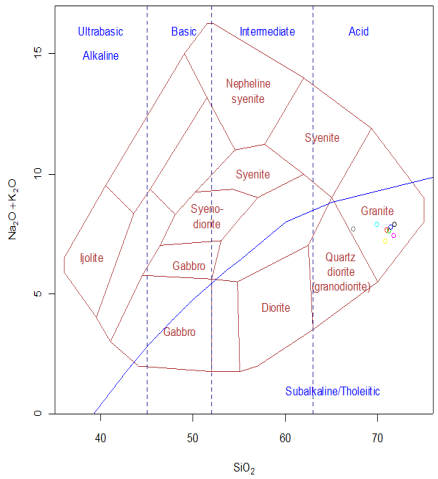

Figure 6. SiO_2 Vs Total Alkalies ($Na_2O = K_2O$) of Cox et al. [33] adopted by Wilson [36] for plutonic rocks. The curved line divides Alkalic and subalkalic rocks. The Mirgarani granite plots in a subalkalic Granite field.

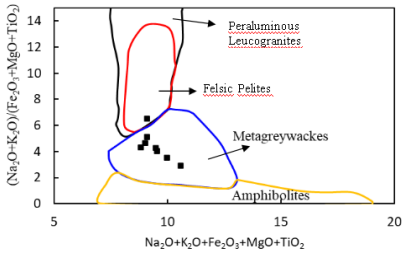

Figure 7a. The binary diagram $Na_2O + K_2O + Fe_2O_3 + MgO + TiO_2$ vs $(Na_2O + K_2O)/ (Fe_2O_3 + MgO + TiO_2)$ after Patiño Douce [34]. Outlined are domains occupied by experimental granitic melts obtained by partial melting of metapelites, metagreywackes, and amphibolites (experiments of Patiño Douce [34] as summarized by Jung et al. [37]).

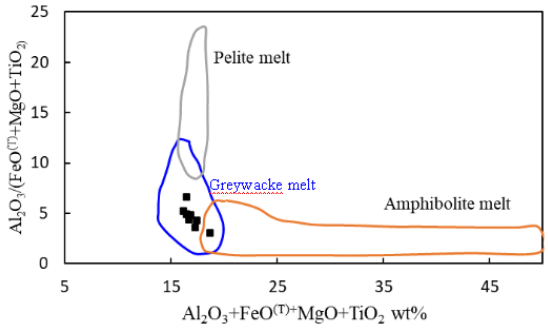

Figure 7b. Binary plot of Al_2O_3 + FeO^t + MgO +TiO_2 versus Al_2O_3/ (FeO^t+ MgO + TiO_2). Outlined are domains occupied by experimental granitic melts obtained by partial melting of metapelites, metagreywackes, and amphibolite (experiments of Patiño Douce [34] as summarized by Jung et al. [37]).

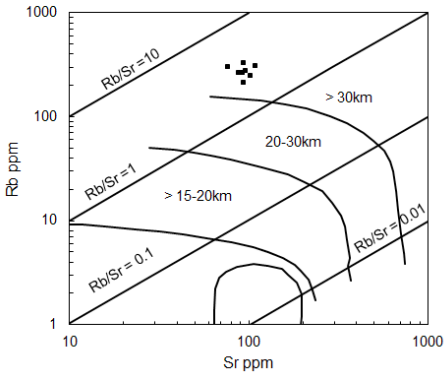

Figure 8. Plot of Rb Vs Sr for Mirgarani Granite the thickness grids after Condie 1973 [35].

A thicker crust increases the probability of crustal anatexis or partial melting of crustal material for the origin of granitic melts. This was further supported by the high initial $^{87}Sr/^{86}Sr$ ratio of 0.715 ± 0.012 (MSWD = 0.11). The presence of garnet and corundum in peraluminous S-type granites also indicates their derivation from the partial melting of sedimentary rocks that had experienced variable surface weathering [38-42]. A high Rb/Sr ratio of 2.23-3.87 with a mean of 2.9 indicates a peraluminous magma source [43]. The Rb-Ba-Sr diagram (**Figure 9**) [44] reveals that the MG is a normal to strongly differentiated granite, which is further supported by the modal plot of the Q-A-P diagram **Figure 3** [45]. The granite melts that created the Mirgarani granite were mainly moderately evolved to strongly evolved. K/Rb ratios of Mirgarani granite vary from 175.47-251.01 ppm with a mean of 200.80 ppm conforming to the K/Rb ratio (150-300) of the normal granite [46]. If the K/Rb ratio is under 100, the granite is highly evolved [47]. This observation occurs because Rb tends to be differentiated in the melt during the segregation stage of aqueous liquid phases from the remaining silicate melts [48]. The importance of K-feldspar, biotite, and plagioclase in differentiation is consistent with Large Ion Litho-modeling (LIL). LIL inter-element variation plots for Sr, Ba-Sr, and Ba-Rb pairs are shown in **Figures 10a and 10b**. Each plot also shows a vector plot representing the net change in the composition of the fluid after 30% Rayleigh fractionation due to the removal of K-feldspar, hornblende, plagioclase, or biotite. In all plots, the trend is consistent with the fractionation of plagioclase, K-feldspar, and biotite. Thus, the log-log plot of LIL suggests that crystal fractionation plays an important role in the magma evolution of the Mirgarani granite.

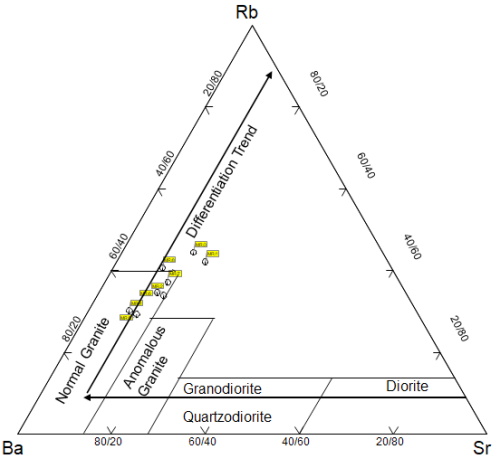

Figure 9. Rb-Ba-Sr Ternary diagram after El Bouseily and El Sokkary [44] reveals that the Mirgarani Granite falls in normal to strongly differentiated granite fields.

The most likely mechanism is crystal fractionation suggested by modeling (**Figures 10a and 10b**). The geochemical characteristics of some elements can be used to trace the materials of magmatic source regions. The Rb/Ba versus Rb/Sr discriminant diagrams (**Figure 11**) exhibit similar source material compositions—mainly clay-rich rocks (sandstone and shale) [51]. Pb-Ba data are plotted in **Figures 12a and 12b**, showing the samples fall in primary Low T, S-type also indicates the behavior of Pb during fractional crystallization.

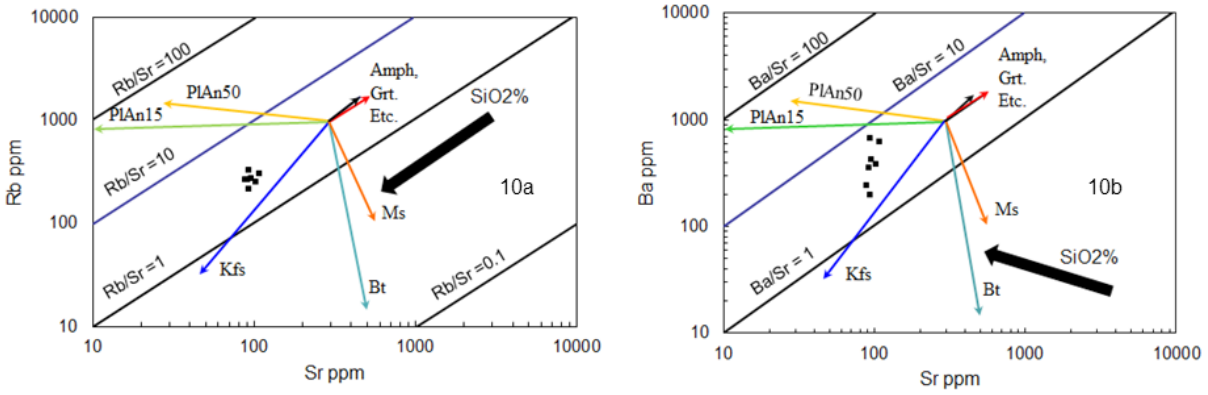

Figure 10. a: Plot of Sr vs. Rb, and **Figure 10b:** Plot of Sr vs. Ba after Rollinson,1993 [76], Janoušek et al., 2004 [83], An Anorthite, PL Plagioclase, Kf K-feldspar, Amph Amphibole, Grt Garnet, Bt Biotite, Ms Muscovite.The black arrow indicates the %SiO_2 variation.

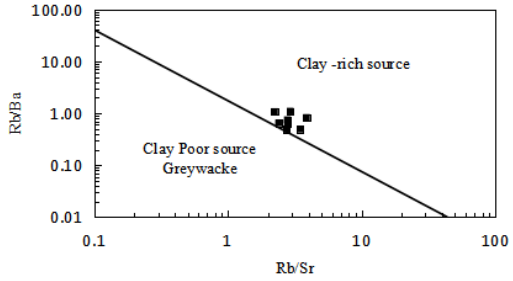

Figure 11. Rb/Sr vs Rb/Ba plot for Mirgarani granite showing its derivation from Clay rich source.

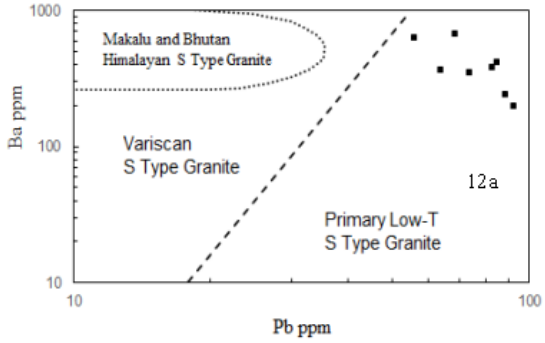

Figure 12a. Logarithmic Pb versus Ba diagrams for Mirgarani Granite showing data for the Makalu, Bhutan, Himalayan, Variscan, S-type granites [52,53].

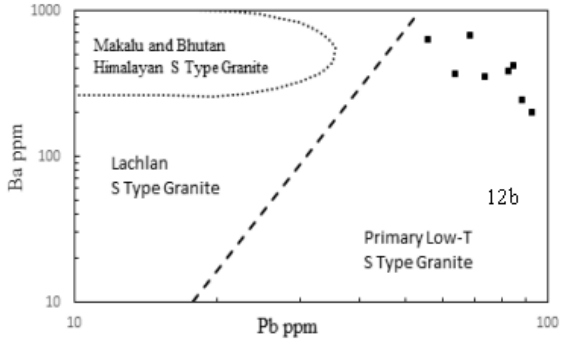

Figure 12b. Logarithmic Pb versus Ba diagram, and Lachlan S-Type granites and primary Low Ti S-Type granite.

7. Zircon saturation and temperature

Zircon behavior in magnetic systems has provided an understanding of magmatic processes and robust Petro-chronology. Watson and Harrison's [42,55] model was used to understanding the Zr saturation with respect to the cationic ratio M (M= Na + K + 2Ca/Al. Si) varies from 1.1 to 1.3 with an average of 1.2, Si, and Zr saturation temperature (**Figures 13a-13f**) clearly shows the fractionation trends. The zircon saturation temperature varies from 764 to 836 °C, with an average of 789 °C (**Table 4**). In the Ab-Or-Q granite system plot [56], the Mirgarani Granite samples occupy a temperature range of 685-700 °C, and M_2 represents the low-pressure granitic minimum at H_2O = 1000 bar [57] in **Figure 14**.

Table 4. Zircon saturation temperature of Mirgarani granite.

S. No.	M	Zr	Zr.sat	TZr.sat.C
MR/1	1.192221	104	87.6	764.1
MR/2	1.186905	116	87.2	773.7
MR/3	1.166125	117	85.7	775.9
MR/4	1.218428	170	89.6	804.8
MR/5	1.252666	247	92.2	836.7
MR/6	1.150865	115	84.6	775.6
MR/7	1.092356	126	80.5	787.7
MR/8	1.155939	145	85.0	795.3

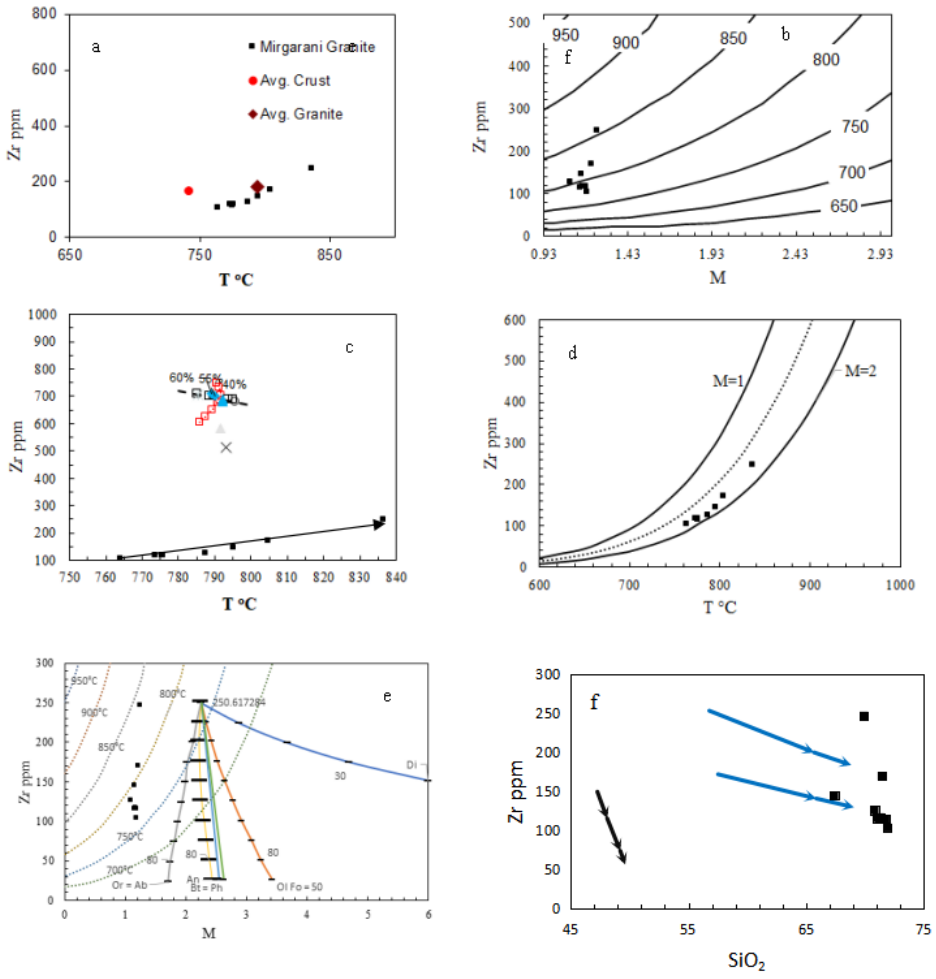

Figure 13. Temperature of crystallization of Mirgarani granite a: Temperature (TC) Vs Zr diagram, b: Binary plot of M=100 (Na+K+-2Ca)/Al*Si versus Zr saturation levels, c: Temperature Vs Zr showing fractionation trends, d: Temperature Vs Zr plots showing various M fields. e: M vs Zr, f: SiO_2 vs Zr with fractionation trends [54,55].

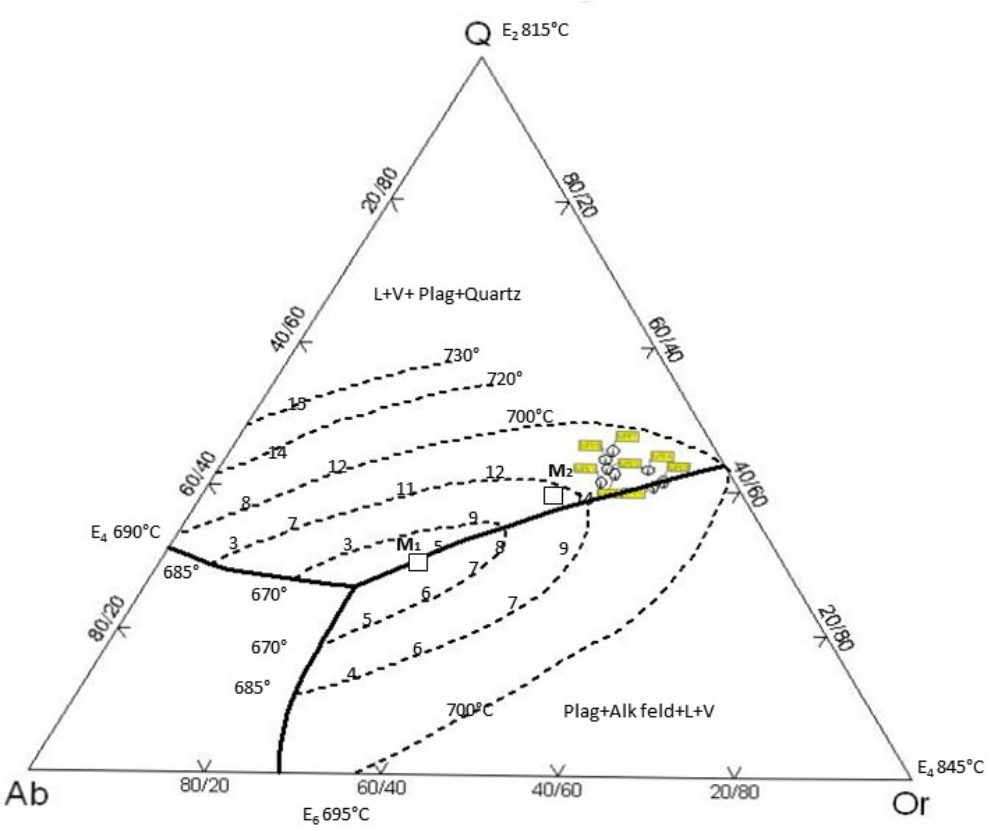

Figure 14. Quartz-Albite-Orthoclase ternary diagram of Mirgarani Granite after Winkler [56], M_1 minimum melt composition at pH_2O = 200bars, M_2 minimum melt composition at pH_2O = 100 bars at 5% An [57]. The numbers correspond to the ternary eutectic at 0.5 and 10 kb pressure, the lines joining eutectic compositions from the cotectic lines in the system. The numbers 3, 6, 9, 11 etc. denote the normative An contents.

8. Radiogenic heat production

Mirgarani granites show elevated levels of heat-producing elements (Th, U, K) and therefore have a high heat-producing capacity of 2.38 to 22.78 $mW \cdot m^{-3}$ with an average of 10.90 $mW \cdot m^{-3}$ (**Table 3**). The radiogenic heat production is calculated by the equation given by Wollenberg and Smith [58]. The unweighted mean of heat-producing capacity for the K-rich Arunta granites is about 6.5 $mW \cdot m^{-3}$ and the granites in the Paleozoic Lachlan Fold belt 3.1 $mW \cdot m^{-3}$ [41]. The bulk heat production in granitic rocks of all ages is ca. 2.0 $\mu W/m^3$. The Archean-Early Proterozoic granitic rocks 1.67 ± 1.49 and 1.25 ± 0.83 $\mu W/m^3$, respectively, and Middle Proterozoic granites presently 4.36 ± 2.17 $\mu W/m^3$, and Cenozoic granites 3.09 ± 1.62 $\mu W/m^3$ [59]. The comparison clearly shows that the Mirgarani granite has a higher heat-producing capacity than granite rocks of all ages, including early and middle Proterozoic granitic rocks, Arunta, and Lachlan fold belt granite. Because there is no specific boundary for defining HHP-type granites, the term HHP, as used here, has a comparative meaning (**Figure 15a**). For comparison, the average value of 6.5 $mW \cdot m^{-3}$ was arbitrarily set as the boundary for discrimination between the Main and HHP groups. **Figure 15b** shows the heat production capacity with respect to the SiO_2 wt.% for meta-sedimentary rocks. There is a decrease in heat production with SiO_2 for all metamorphic conditions for igneous rocks, but the differences within grades for rocks of similar SiO_2 do not show any consistent pattern. The curves for igneous and sedimentary rocks are shown in **Figure 15b**. A comparison of the HPU is shown in **Figure 15c**.

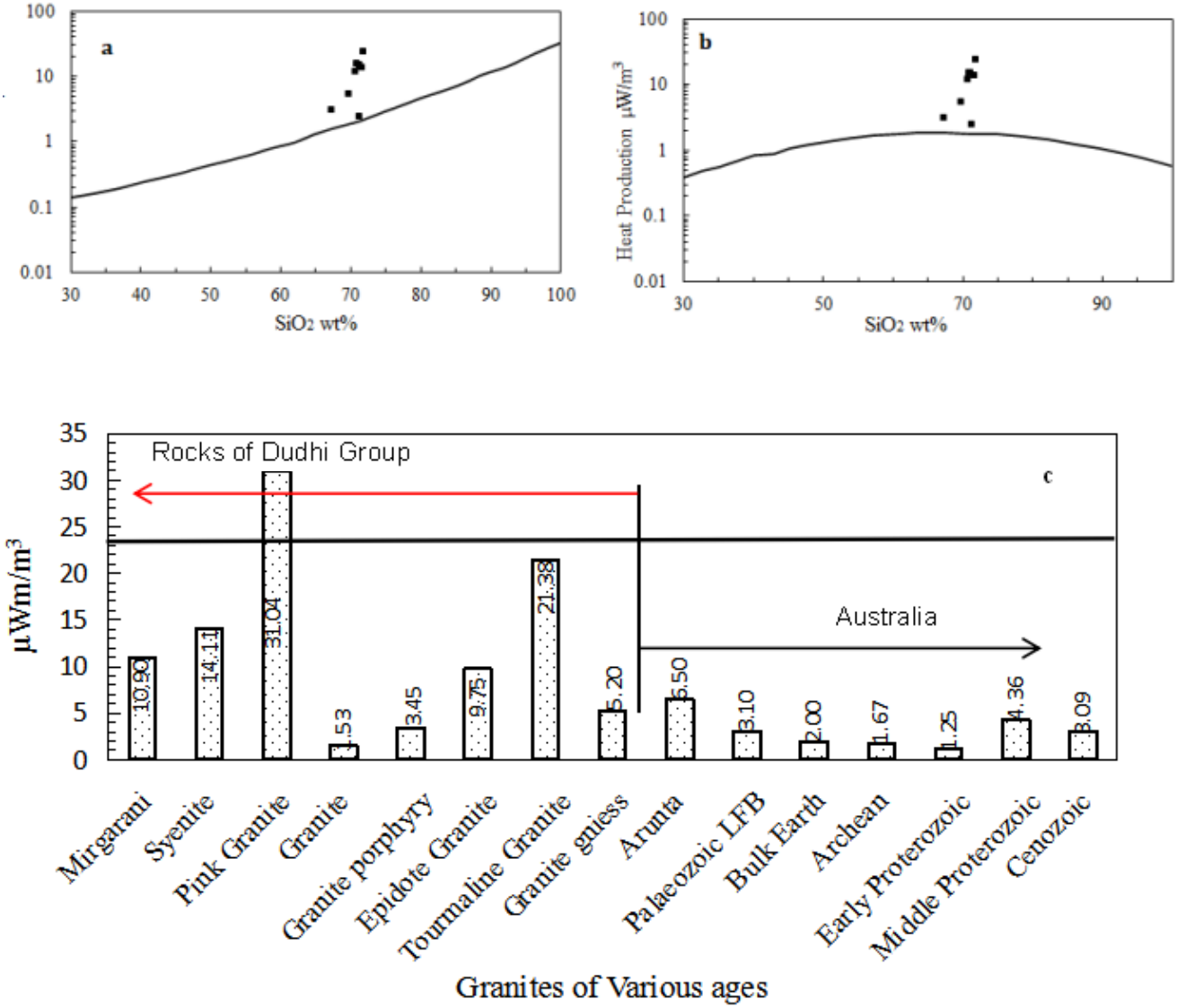

Figure 15. Heat production as a function of SiO_2 wt% with a heat production capacity of Mirgarani granite content. The curves are quadratic fit to heat production of igneous. **15a:** meta-igneous rocks and **15b:** metasedimentary rock samples as a function of metamorphic grade. Black curves are quadratic. For igneous rocks, the fit is constrained to 40 £ SiO_2 wt% £80 SiO_2 wt%; and for sedimentary rocks, the fit is constrained to £30 SiO_2 wt% £ 100 SiO_2 wt%. **15c:** Comparative bar chart of HPU of Granites of Dudhi Group with Australian Granites, Bulk earth, and granites of various ages.

9. Tectonic discrimination

Discriminant diagrams were used to ascertain the geotectonic environment in which the MG was emplaced. The Y + Nb vs. Rb plot (**Figure 16a**) [60]. The MG occupies within plate field (n = 6) with minor overlap in the syn collision granite (n = 2) field, whereas the Y vs Nb plot (**Figure 16b**) [60] occupies WPG (n = 5) to SCG + VAG (n = 3). In the R2 vs. R1 plots, the Mirgarani granite mostly falls in syn-collisional fields (**Figure 16c**). Therefore, the Mirgarani granite can be classified as within plate granite and can be correlated to the bimodal magmatism (Anorthosite-Granite) event in the CGGC during the late Paleo-Proterozoic to early Meso-Proterozoic i.e., ~ 1600 Ma [61].

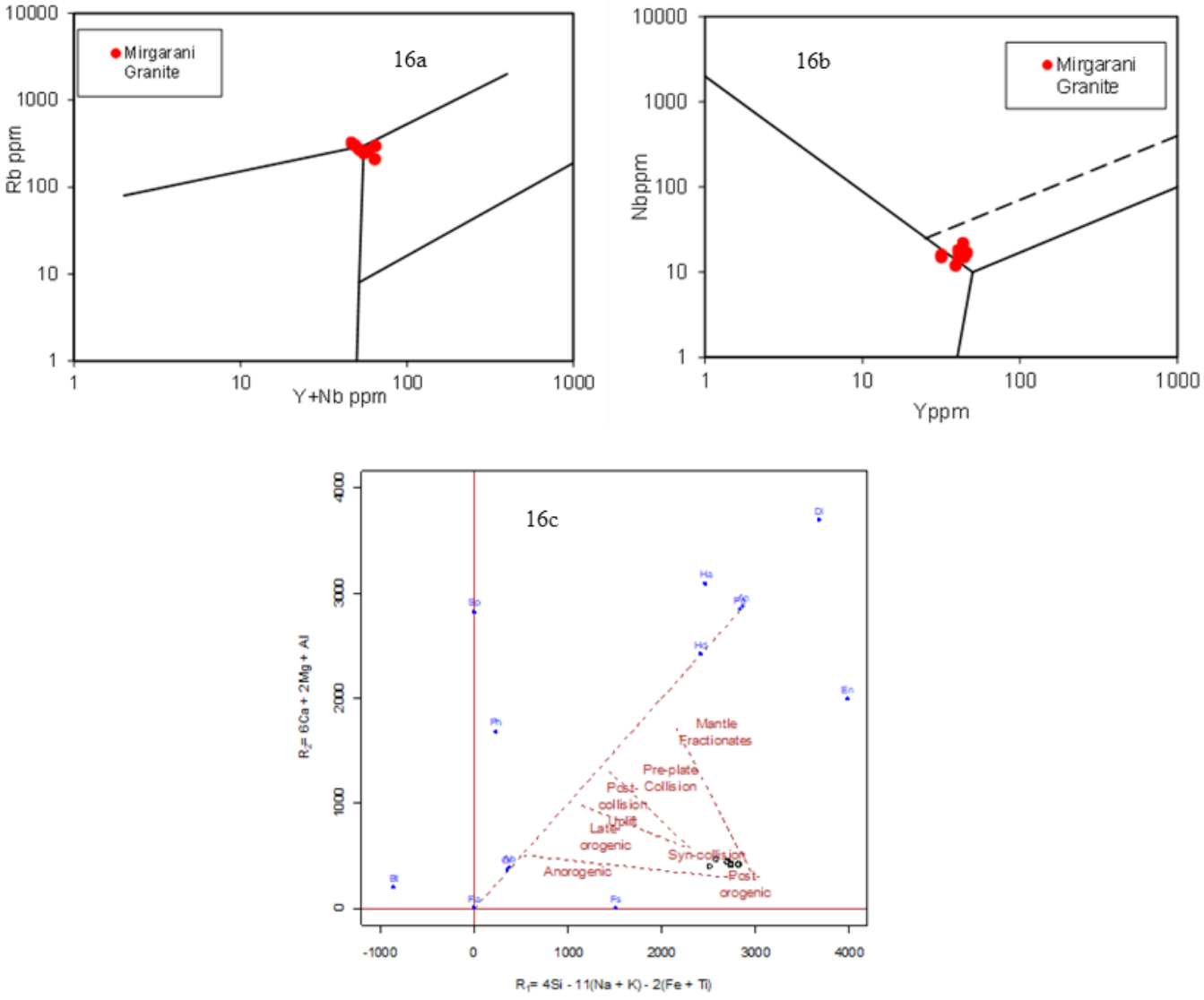

Figure 16. Tectonic discrimination plots for Mirgarani Granite, **16a:** Y+Nb Vs Rb plot showing CCG character, and **16b:** Y vs Nb Plot showing Syn collisional Granite field fileds [60]. **16c:** R_1-R_2 Plot showing syn-collisional origin for Mirgarani Granite Such rocks were generated by partial melting of the deep crustal rocks and intruding in the early stages of major intracontinental rifting during the mid-Proterozoic [62] or into the thickened overriding plate of a continental collision mobile belt [63].

10. Geochronology

The eight samples of Mirgarani granite were collected from Mirgarani hillock and analyzed for Rb-Sr isotopes on thermal ionization source, multi-collector computer-controlled VG-354 mass spectrometer. The standard exchange technique was followed for the separation of Rb and Sr from the powdered rock samples. Rubidium and Strontium contents of the samples (**Table 6**) were measured by conventional isotopic dilution technique as discussed by Gupta et al. [64]. $^{87}Rb/^{86}Sr$ of eight samples has been plotted against the Sr ratio (**Figure 17a**). The straight line obtained defines the isochron age of 1636 ± 66 Ma with an initial Sr ratio of 0.712 ± 0.012 with MSWD 0.11. Strontium evolution in CGGC has been attempted by integrating all the Rb-Sr isotopic data available in CGGC, particularly in the northwestern and western parts of the CGGC. The relevant data are conveniently displayed on the $^{87}Sr/^{86}Sr$ development

diagram (**Figure 17b**). The simplest model for crustal formation involves continuous mantle-to-crust evolution on the one hand and two-stage evolution on the other. Isotopic research should permit the assessment of these models; no clear picture has so far emerged, perhaps because of the recycling of crustal material through the mantle [65]. A development line is defined by a regular trend of initial $^{87}Sr/^{86}Sr$ ratios, as a function of time, from a family of related rock systems. The two-stage model advocates the formation of most of the sialic crust from the upper mantle early in the Earth's history, with younger granitic rocks forming largely by anatexis of this primitive crust [66,67]. The development line for the upper mantle has been represented by [68] line AB in **Figure 17b**. In contrast, if formed in one episode early in the Earth's history, the development line for the entire sialic crust would be represented by a line of much steeper slopes. Using the estimated average Rb/Sr ratio for the sialic crust of 0.15 [65], this line is represented by C'D' in **Figure 17b**. The alternative simple model advocates the continued formation of new continental sialic crust in many episodes of differentiation from the upper mantle, with only minor amounts being formed by anatexis of older continental rocks [69,70]. The development line for the mantle beneath a large volume of such sialic crust may be represented by a curve or succession of straight lines, initially of steep attitude but following a successively gentler slope with time. On this hypothesis a steep vector for crustal rocks would represent only one of the many granite-forming events; it would be restricted to a small volume of crust that originated in a single upper mantle differentiation event. A recent exposition of this hypothesis [71] invoked an environment of plate convergence and a sequence of subduction, partial melting of the mafic lithosphere, and extraction of basaltic and calc-alkalic rocks, with resulting accretion of new continental crust. Repeated reworking of significantly older sialic crust—with anything like normal Rb/Sr ratios—is rejected; the basic hypothesis precludes the possibility of large volumes of different lower Precambrian granites, whose individual ages range over a substantial time interval (say, 500 m.y.), yielding initial $^{87}Sr/^{86}Sr$ ratios on a straight line of a steeper slope than the upper mantle development line. Both models postulate the beginning of the formation of extensive continental sialic crust in the period from 3,000 to 3,500 m.y. ago. Since these models were formulated, Rb-Sr and U-Pb age determinations from several areas have extended the upper limit back to sometime around or before 3,700 m.y. ago.

Table 6. Rb-Sr data on Mirgarani granite.

Sample No.	Rb ppm	Sr ppm	87Rb/86Sr	87Sr/86Sr
MR1	257	55.3	13.9	1.04237
MR2	258	58.2	13.26	1.02732
MR3	253	53.5	14.18	1.04942
MR4	258	56.9	13.54	1.035206
MR5	246	72.6	10.04	0.94999
MR6	259	76.8	9.998	0.94964
MR7	264	51	15.54	1.08066
MR8	253	47.2	16.1	1.08823

Error: 1% in Rb and Sr values, 2% in $^{87}Rb/^{86}Sr$, and 0.05%in $^{87}Sr/^{86}Sr$.

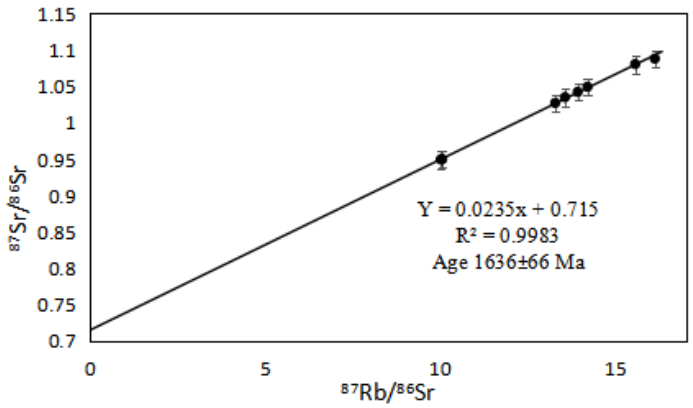

Figure 17a. Rb-Sr Isochron plot for Mirgarani granite.

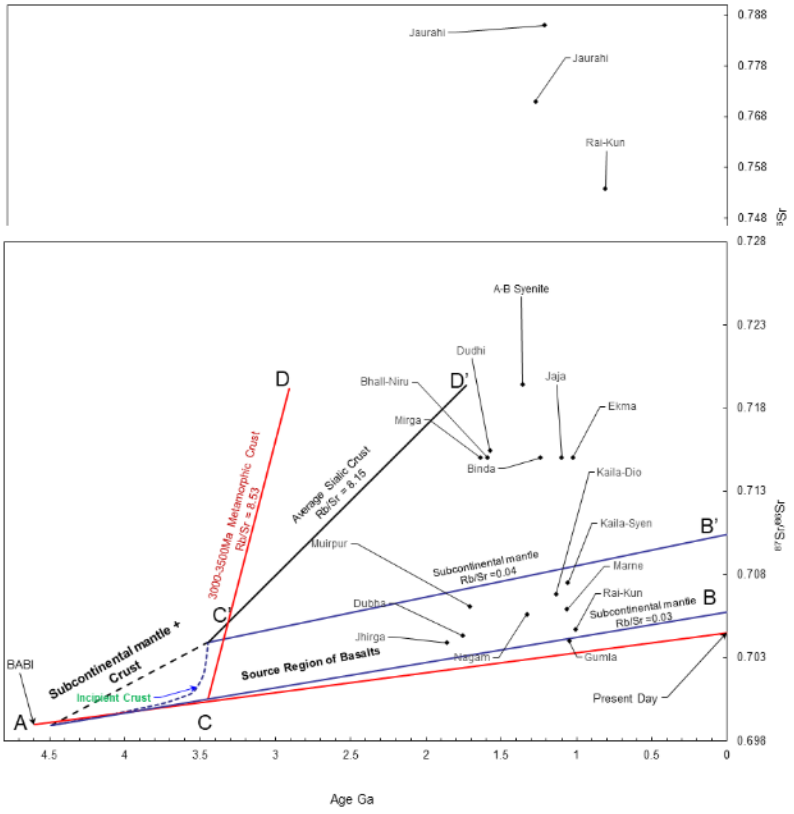

Figure 17b. Diagram showing the variation of the initial $^{87}Sr/^{86}Sr$ ratio with age. Vectors from each point, length immaterial, indicate the direction of isotopic evolution with time; calculated from the mean Rb/Sr ratios for each suite. Suboceanic and subcontinental mantle development lines shown were proposed by Davies et al. [70]; they are bounded by achondrite value (A), the mean value for recent oceanic tholeiites (B), and extension of the trend of values for mafic rocks in southern Africa (B'). It is proposed that the "source region of basalts" field is bounded *by* these two development lines. Hypothetical development line C'D' for average sialic crust conforms with a two-stage model involving a major mantle-crust differentiation about 3500 m.y. ago; this line intersects T = 0 axis at $^{87}Sr/^{86}Sr = 0.725$. The Red line shows $^{87}Sr/^{86}Sr$ ratio (0.69897 ± 0.00003) evolution from BABI to the present day The other parameter for UR model is $^{87}Rb/^{86}Sr$ ratio of the bulk earth is 0.0816 and the present-day Sr value is 0.7045.

11. Discussions

Petrochemical characteristics, field setting, and co-genetic granites and granitoids of Dudhi Group which form the northwestern part of CGGC, and a review of the geochronological data (**Table 7**) show five phases

of granitic activities. The first phase of granitic activity dates from the Gaya area, the age of the Satpura orogenic cycle was considered to be 955 Ma [72,73]. The Chhotanagpur plateau has been formed due to the three successive phases of orogeny during the middle to late Proterozoic time. These orogenic movements have deformed the area in three successive phases.

The CGGC is dissected by three major lineaments (**Figure 18a**). The South Purulia Shear Zone (SPSZ) and Monghyr-Saharsa Ridge Fault roughly coincide with the southern and northwestern boundaries of the CGGC respectively. The lineament, that bound the exposure of Gondwana deposits of Damodar valley runs through Domain I of the CGGC [74] and is hereafter termed Gondwana Boundary Faults (GBF) (**Figure 18a**). Using the GBF as a marker, Domain I is further divided into two geographic sub-domains viz. Domain IA (south) and IB (north) by GBF and southern boundary fault of Gondwana Graben and Jajawal Shear zone. Accessibility issues led to a dearth of geochronological data from the western and northwestern regions of CGGC. The Son-Narmada South Fault (SNSF) and North Fault (SNNF) cause radiometric breaks in the radio-geochemical images based on airborne gamma-ray spectrometric data in the Son-Valley area, where the Mahakoshal group of volcano-sedimentary rock have deposited in the rift valley known as Son Valley. These faults have NE-SW, East-West, and ENE-WSW trending faults [20]. Mirgarani granite is coeval to the granites in Bihar Mica Belt (BMB) around the Bhallupahari-Nerupahar, Hazaribagh area dated 1590 ± 30 Ma [75]. High-precision U-Pb SHRIMP zircon $^{206}Pb/^{238}U$ ages for Microgranular Enclave (1758 ± 19 Ma) and host granitoid (1753 ± 9.1 Ma) from Jhirgadandi Pluton further support that they were coeval. Jhirgadandi granodiorite (Jh) is dated by Rb-Sr whole-rock method 1860 ± 180 Ma with an initial Sr ratio of 0.7039 ± 38 [76]. Other coeval granitoids in the area are Jhirgadandi granitoid (Jh; 1753-1880 Ma), Tumiya granitoid (T; 1780 Ma), and Neruiyadamar granitoid (N; ca. 1880 Ma) within the Mahakoshal group whereas, Harnakachar granitoid (H; 1710 Ma), Katoli granitoid (Ka; 1730 Ma), ± 9.1 Ma, Dudhi Granite; 1750 Ma, Raspahari granitoid (R; ca. 1750 Ma) are in the Dudhi Group. Ainti-Bari syenites dated by Rb-Sr method as 1360 ± 30 Ma with $^{87}Sr/^{86}Sr$ ratio of 0.7194 ± 12 [75]. High Rb and Low Sr Riebeckite granites at the Jaurahi area gave an isochron age of 1280 ± 78 Ma with $^{87}Sr/^{86}Sr$ ratio 0.771 ± 0.039 with MSWD 21. However, the Low Rb and High Sr Riebeckite granites of all the samples considered together then gave an isochrone age of 1219 ± 74 Ma with $^{87}Sr/^{86}Sr$ ratio of 0.786 ± 0.048 with a very high MSWD 56. The Pb-Pb isotopic isochrone age was found at 1219 ± 190 Ma with model μ8.3 ± 0.2 and MSWD of 9.1. It is therefore taken as 1290 ± 190 Ma [77]. Makrohar granulite 1700-1580 Rb-Sr whole-rock isochron ages [78]. Kirwil-Sagobandh Mafic Granulites dated 1648 ± 112 Ma with $^{87}Sr/^{86}Sr$ ratio of 0.70202 ± 0.00032 with MSWD 0.040 [23]. Both of these granulites i.e. Makrohar and Kirwil Sagobandh show post peak isobaric cooling events in the area. Other Granulites in CGGC are in **Table 7**. The IBC pathways > 1457-1648 Ma while the ITD paths are < 1447-930 Ma [11,21,23,78,80,81].

Barambaba granite 1690 ± 70 Ma Rb-Sr age [82], Rihand granite 1731 ± 36 Ma and Vikasnagar granite and Kundabhati granites have Rb-Sr ages of 1717 Ma, and 900-1292 Ma, respectively [79], also the Purulia granites and syenites of Jamua-Dumka sector Bihar are dates 1331 ± 125 [80]. Muirpur Granite five sample whole-rock defines Rb-Sr isochron age of 1709 ± 102 Ma with an initial $^{87}Sr/^{86}Sr$ ratio of 0.70609 ± 342 and MSWD of 0.59 [78], Dudhi Granite Gneiss's six whole-rock samples define an Rb-Sr isochron age of 1576 ± 76 Ma with an initial $^{87}Sr/^{86}Sr$ ratio of 0.71543 ± 89 and MSWD of 0.29 [75]. The Mahakoshal Belt experienced a period of relaxation marked by vast post-collisional episodic magmatism 1880-1710 Ma and forming the Neruiyadamar Granitoid (1880 Ma) and Jhirgadandi granite (1860 Ma, 1753 ± 9.1 Ma), Dudhi Granite gneiss (1750 Ma), Raspahari granitoid (ca. 1750 Ma), Katoli granitoid (1730 Ma) and, Tumiya Granitoid (1780 Ma), Harnakachar granitoid plutons (1710 Ma) of the Mahakoshal Belt [83,84]. These Rb-Sr ages around 1636 to 1880 Ma can be correlated to the Chhotanagpur orogeny and Columbia-Nuna supercontinent.

Table 7. Age data on Chhotanagpur granite Gneiss complex.

Geological Time	Rock types and locality	Methods	Age (Ma)	Reference	LIPs
	Phase V				
Mesozoic (251-66 Ma)	Sylhet Traps	K-Ar	110 ± 3, 133 ± 4	Sarkar et al., 1996 [102]	
	Rajmahal Traps		117 ± 2	Bakshi, 1995 [95]	
	Lamprophyre dykes Minnet and Lamproite Jhariya and Raniganj Rajmahal.	$^{40}Ar/^{39}Ar$ dating	113 ± 7	Sarkar et al., 1980 [114]	
	Dykes intruded on the SW of the Rajmahal Hills	$^{40}Ar/^{39}Ar$ dating	115-118	Kent et al., 2002 [116]	
	Dolerite Dyke near Latehar railway station	K-Ar	185	Ghose et al., 1973 [98]	Wegner's Pangea c.325-175 Ma
	Phase IV				
	Rhyodacite, Mahuandanr-Rajdanda	K-Ar	217-214	Sarkar, 1974, [99]	
Paleozoic (541-251)	Enstatite/Hornblende Peridotite, Pyroxinite and Hornblendite, Richughuta (unmetamorphosed)	K-Ar	275	Ghose et al., 1973 [98]	
	Phase III				
	Aphanitic Quartz rich granite aplite	K-Ar	353	Ghose et al., 1973 [98]	Gondwanaland/ Pannotia (620-580 Ma) Cryogenian Period (ca. 720-635 Ma)
	Syenite, Nepheline syenite and Alkali granite.	K-Ar	435		
Neoproterozoic (1000-541 Ma)	Phase II				
	Allanite Puruliya Bihar Allanite Bahea Singar Bihar	U+Th-Pb	880 880	Nandi and Sen, 1950 [90]	
	Pegmatite, Dumhat	Rb-Sr whole-rock Isochron	886, 932, 941	Pandey et al., 1986a [86]	Rodinia (1100-700 Ma)
	Mica Granite	Rb-Sr Mineral Age	855 ± 25		
	Kunkuri, Raigarh Raikera-Kunkuri	Rb-Sr WR	803 ± 49, 815 ± 47, 1005 ± 51	Singh and Krishna, 2009 [97]	
	Leucogranite Muscovite, Belamu-Jaipur	K-Ar	810 ± 40	Baidya and Chakravarthy, 1988 [96]	
	Pegmatite Columbite -Tantalite, Dhajua pegmatite etc.	U-Pb, Pb-Pb Mineral	910 ± 19	Krishna et al., 2003, [83]	
	Singar Gaya Uraninite from pegmatite	U+Th-Pb	955 ± 40	Holmes et al., 1950 [89]	
Neoproterozoic (1000-541 Ma)	Pichali Bihar, Monazite Magnetite Chaibasa Bihar	U+Th-Pb Alpha-Helium	970 970	Nandi and Sen, 1950 [90] Krishnan et al., 1953 [92]	
	Raigarh Granite II (Kunkuri)	Rb-Sr WR	972 ± 114	Pandey et al., 1998 [79]	

Table 7 continued

Geological Time	Rock types and locality	Methods	Age (Ma)	Reference	LIPs
Neoproterozoic (1000-541 Ma)	Uraninite from Bihar Mica Belt	U+Th-Pb	960 ± 50	Vinogradov et al., 1964 [88]	
	Kundabhati Granite	Rb-Sr	900-1292	Pandey et al., 1998 [79]	
	Monazite from Gaya Allanite from Ranchi	U-Pb U-Pb	965 Ma 980 Ma	Sarkar, 1941 [91] Lal et al., 1976 [94]	
	Migmatitic Quartzo- Feldspathic Gneiss, NE Dumka Near N. margin of CGGC, ITD	Monazite in Garnet Matrix	984-930 Ma	Chatterjee et al., 2010 [12]	
	Basic Granulites, Bero N. Purulia, ITD, 11 to 5kbar	U-Pb Monazite	990-940 Ma	Karmakar et al., 2011 [81]	
Mesoproterozoic (1600-1000 Ma)	Phase I				
	Uraninite	U+Th/Pb	1000 Ma	Vinogradov et al., 1964 [88]	
	Purulia Granite	Rb-Sr WR	1071 ± 64	Ray Barman et al., 1994 [80]	
	Gumla granite	Rb-Sr WR	1051 ± 272, 1048 ±135	Pandey et al., 1998 [79]	
	Ekma Granite	Rb-Sr WR	1025 ± 11	Singh and Krishna, 2009 [99]	
	Alkali syenite, Kailashnathgufa	Rb-Sr WR age	1059 ± 104	Pandey et al., 1998 [79] Singh and Krishna, 2009 [97]	
	Marme pink granite	Rb-Sr WR	1065 ± 74	Singh and Krishna, 2009 [99]	
	Jajawal Granite Gneiss	Rb-Sr WR	1100 ± 20	Pandey et al., 1986b [87]	
	Chianki granite gneiss	Rb-Sr WR	1119 ± 24	Singh and Krishna, 2009 [97]	
	Raigarh diorite, Kailashnathgufa	Rb-Sr WR	1138 ± 193	Pandey et al., 1986b [87] Singh and Krishna, 2009 [97]	
	Migmatitic Gneisses, Jamua-Dumka, ITD	Rb-Sr WR	1178 ± 68 Ma	Ray Burman et al., 1994 [80]	
	Migmatitic Granite gneiss, Hesatu–Belbathan area	Rb-Sr whole-rock	1300-1110	Pandey et al., 1986 a, b [86,87]	
	Binda-Nagnaha, Granite-gneiss	Rb-Sr whole-rock	1242 ± 34	Pandey et al., 1986a [86]	
Paleoproterozoic 2500-1600 Ma	Granite and Riebeckite Granites Granite and Riebeckite Granites	Rb-Sr WR Pb-Pb WR	1219 ± 74, 1280 ± 78 1219 ± 130	Sastry et al., 2017 [77]	Break up of Columbia/Nuna 1.5-1.2 Ga
	Raigarh I Nagam granite	Rb-Sr, WR	1331 ± 42	Singh and Krishna, 2009 [97]	
	Syenite	Rb-Sr, WR	1331 ± 125	Ray Burman et al., 1994 [80]	
	Migmatitic granite gneiss, NE part of the CGGC	K-Ar whole-rock age dating;	1416-1246	Sarkar, 1980 [9]	
	Dumka granulite	Rb-Sr WR	1331 ± 125	Ray Burman et al., 1994 [80]	
	Charnockite Gneiss, Jamua-Dumka Sector Purulia, ITD	Rb-Sr WR	1447 ± 11 Ma		
	Charnockite Gneiss, Deoghar–Dumka, IBC	Rb-Sr WR	1457 ± 63 Ma	Ray Burman et al., 1994 [80] Mukherjee et al., 2019 [16]	Columbia / Nuna 1.9-1.6Ga
	Dumka syenite	Rb-Sr WR	1457 ± 63	Ray Burman et al., 1994 [80]	
	Mica belt granite I, Bhallupahari-Nirupahari	Rb-Sr WR	1590 ± 30	Pandey et al., 1986a [86]	

Table 7 continued

Geological Time	Rock types and locality	Methods	Age (Ma)	Reference	LIPs
Paleoproterozoic 2500-1600 Ma	Mor Valley migmatite	Rb-Sr WR	1580 ± 33	Sarkar et al., 1998 [78]	
	Massive charnockite Basic granulite- Jamua–Dumka, Purulia IBC	Rb-Sr whole-rock isochron	1515 ± 5, 1000 1515	Ray Burman et al., 1994 [80]	
	Dudhi Granite gneiss	Rb-Sr WR	1576 ± 76	Sarkar et al., 1998 [75]	
	Mor valley	Rb-Sr WR	1599-1522	Mallik et al., 1991 [85]	
Paleoproterozoic 2500-1600 Ma	Hypersthene Gneiss, IBC	Rb-Sr WR	1624 ± 5 Ma	Sarkar et al., 1998 [78]	
	Massive Charnockite and Basic Granulites, Jamua-Dumka Sector Purulia, IBC	Rb-Sr WR	1624 ± 5, 1000	Ray Barman et al., 1994 [80]	
	Barambaba granite	Rb-Sr WR	1690 ± 70	Jain et al., 1995 [82]	
	Mirgarani granite	Rb-Sr WR	1636 ± 66	Present Study	
	Kirwil-Sagobandh Mafic Granulites, Post-peak IBC path	Rb-Sr WR	1648 ± 112	Dhurandhar et al., 2003, 2006 [20,22]	
	Makrohar granulite, IBC, 7-7.5 kbar	Rb-Sr WR	1700-1580	Sarkar et al., 1998 [75]	
	Harnakachar granitoid	U-Pb SHRIMP	1710 Ma	Bora and Santosh, 2015 [84]	
	Vikasnagar Granite	Rb-Sr WR	1717 Ma	Pandey et al., 1998 [79]	
	Katoli granitoid	U-Pb SHRIMP	ca.1730 Ma	Bora and Santosh, 2015 [84]	
	Rihand granite	Rb-Sr WR	1731 ± 36	Sarkar et al., 1998 [78]	
	Muirpur granite	Rb-Sr WR	1709 ± 102		
	Raspahari Granitoid	U-Pb SHRIMP	ca. 1750 Ma	Bora and Santosh, 2015 [84]	
	Dubha granite	Rb=Sr WR	1754 ± 16	Dhurandhar et al., 2005 [22]	
	Metapelitic granulite. Southern margin of CGGC	Rb-Sr WR	1741 ± 65	Ray Barman et al., 1994 [80]	
	Tumiya Granitoid In Mahakoshal Group	U-Pb SHRIMP	ca.1780 Ma	Bora and Santosh, 2015 [84]	
Paleoproterozoic 2500-1600 Ma	Tatapani gray migmatite	Rb-Sr WR	1787 ± 72	Hansoti and Deshmukh, 1990 [24]	Columbia / Nuna 1.9-1.6Ga
	Jhirgadandi Granite-Granodiorite in Mahakoshal Group	Rb-Sr WR U-Pb SHRIMP	1860 ± 180 Ma 1753 ± 9.1 Ma	Pandey et al., 2004 [76] Bora et al., 2013 [83] Bora and Santosh, 2015 [84]	
	Neruiyadamar Granite in Mahakoshal Group	U-Pb SHRIMP	ca 1880 Ma	Bora and Santosh, 2015 [84]	

The radioactive minerals are dated around 800-900 Ma typically during Phase II i.e. Uraninite from Gaya Bihar 960 ± 50 [88], 955 ± 40 Ma from Singar [89], Pichali Monazite 970 [90], Gaya monazite dated 965 Ma [91], and Magnetite from Chaibasa also dated 970 Ma [92], Columbite and Tantalite in pegmatite are dated 910 ± 19 by U-Pb, Pb-Pb Mineral methods [93]. Allanite from Ranchi dated 980 Ma [94], and from Singar and Puruliya both are dated 880Ma by the U-Pb method [95]. Moreover, the Pegmatites from these areas viz. Belamu, Jaipur 810 ± 40 by K-Ar method [96], and Kunkuri Raigarh and Raikera area, also dated between 800 to 941 Ma by Rb-Sr isochron methods [97] but these have very high initial strontium ratio indicating a higher degree of crustal contamination (**Table 7** and **Figure 17b**). These episodes correlate well with Rodinia supercontinent.

Phase III is marked by the intrusion of alkaline magma such as Syenite, Nepheline Syenite, and alkali granites dated 435 Ma and Aphanitic Quartz rich granite aplite dated 353 Ma both by K-Ar methods [98].

Phase IV begins with the hornblende peridotite, pyroxenite hornblendite dated 275 Ma by K-Ar method [98] and Rhyodacite, Mahuandanr – Rajdanda area dated 214-217 Ma [99].

Finally, Phase V is marked by extrusives like dykes of Latehar 185 Ma, SW of Rajmahal 115-118 Ma, Lamprophyre and Minnet Lamprophyres Jhariya and Raniganj area dated by $^{40}Ar/^{39}Ar$ 113 ± 7 Ma [100], and volcanic of Rajmahal 117 ± 2 [101] and Sylhet Traps 110 ± 3 to 133 ± 4 Ma in northeastern India [102]. Phases III, IV, and V are related to Pan-African activities and the Pangea breakup.

12. Implications for super continental amalgamation and fragmentations

The evolution of earth's history shows that several supercontinents assembled and broken up viz. 3.0 Ga Ur [103] c. 2.7-2.5 Ga Kenorland; [104]; Lauroscandia; [105]. c. 1.9-1.75Ga Nuna or Columbia assembled or perhaps 1.6 Ga, and fragmented during the interval 1.3-1.2 Ga [106-108]. Rodinia supercontinent was being drafted, based on the growing recognition of correlatable mid-Neoproterozoic (0.8-0.7 Ga) rifted passive margins, many of which were established on the eroded remnants of late Mesoproterozoic (1.3-1.0 Ga) orogenic belts [109]. c. 950-800 Ma Rodinia [110], Rodinia Supercontinent existed from 1000 to 725 Ma. The Cryogenian Period ca. 720-635 Ma, which occurred about 700 Ma may have been a result of the breakup of Rodinia that began about 725 Ma [111], and the subsequent amalgamation of Gondwanaland. c. 620-580 Ma Gondwanaland/Pannotia [112,113]; the break out of Laurentia from Rodinia at 725 Ma marks the re-organization of lithospheric plate motion that resulted in the Pan-African-Brasiliano orogeny.

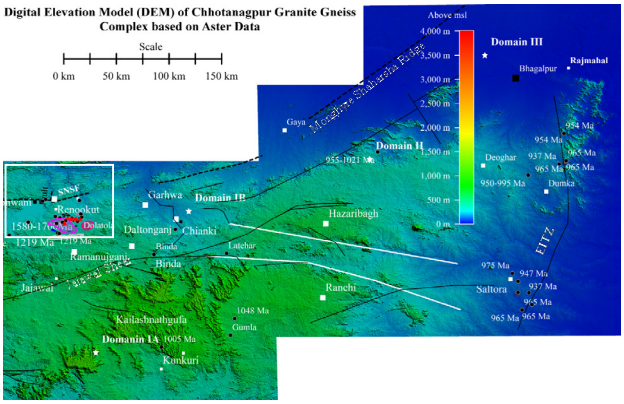

Figure 18a. Digital Elevation Model (DEM) of Chhotanagpur Granite Gneiss Complex showing major tectonic lineaments and study area.

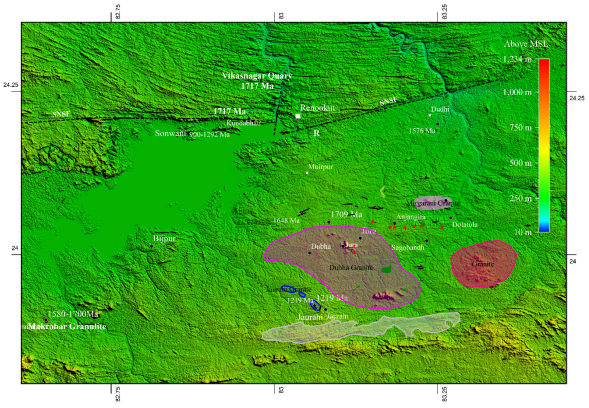

Figure 18b. DEM of Dudhi Group showing ages of various rock types, R: Raspahari Granitoid, Ka: Katoli Granitoid, H: Harnakachar Granitoid.

The formation of Gondwanaland and breakups are debated [114,115] as under:

The Gondwana Assembly 520-450 Ma, and Gondwana breakup 140-130 Ma.

The assembly of Gondwanaland lasted from c720-500 Ma; and in addition to Wegener's Pangea (c. 325-175 Ma). Older supercontinents that existed before Pangea was based on 'common' isotopic ages observed in various places around the globe. The ages obtained from the study area were plotted on the age time chart to depict the evolution of the area with opening and closing events ranging from Nuna-Columbia (Mirgarani Granite) to Rodinia and Pangea-Amasia (**Figure 18c**, and **Table 7**). Dudhi group granitic intrusions between 1.9 to 1.7 Ga are accretion orogen during Columbia-Nuna, igneous activities between 1100 to 700 Ma are correlated with Rodinia, and no igneous activities were observed during the Cryogenian period ca. 720-635 Ma, however, the Gondwana sedimentation took place in the grabens in CGGC. Alkaline and acidic magmatism was again seen during 435 to 117-113 Ma Pan African activities related to Pangea breakup and continent movement due to Kerguelen plume activity [116].

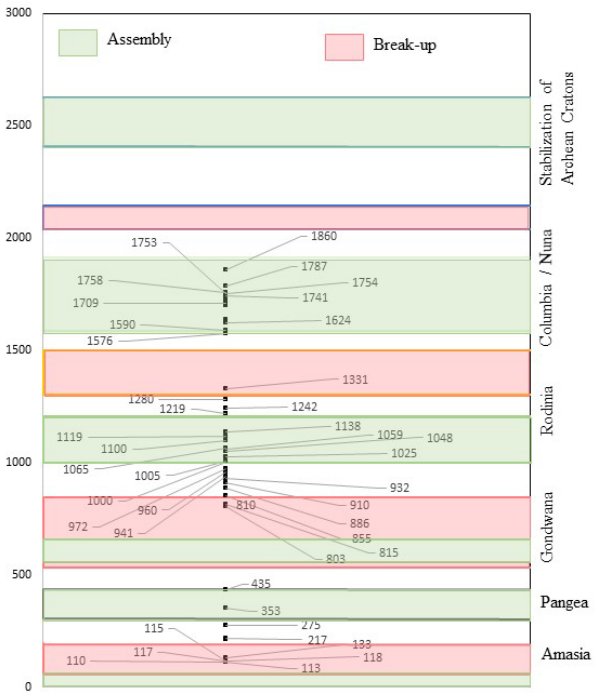

Figure 18c. Supercontinents assembly, break-ups, and relationships of various intrusive and extrusive phases in CGGC.

13. Conclusions

The Mirgarani pluton was emplaced at 1636 ± 66 Ma. It emplaced into the collisional compressional environment between the late Paleo- to early Mesoproterozoic. Geochemically Mirgarani granite is subalkalic peraluminous high silica, iron, potassic, low calcic, and magnesium-bearing S-type granite. It is corundum normative and garnet's presence further corroborates its S-Type characteristics. It is enriched in K_2O, FeO, Rb, Pb, Th, U, Cr, Ni, and Co and depleted in Sr, Nb, Ba, and Zr as compared to the normal granite. Mirgarani granite is formed due to the partial melting or crystal fraction during the granitization of clay-rich metagraywacke. The temperature of magma was ranging between 764-837 °C with an average of 789 °C. It's due to elevated Zircon concentration varying from 104-247 ppm with an average of 143 ppm. It has elevated contents of U, Th, and K resulting in its high heat capacity of 2.38 to 22.78 $mW \cdot m^{-3}$ with an average of 10.90 $mW \cdot m^{-3}$. The Dudhi group of rocks has high heat-producing capacities. It is related to compressional environment during the Columbian - Nuna supercontinent. The review of geochronological data especially from the Northwestern and Western parts of CGGC shows five phases of tectono-magmatic activities viz. Phase I 1880 to 1000 Ma, Phase II 980 to 880 Ma, Phase III 435-353 Ma, Phase IV 275-214 Ma, and Phase V 185-100 Ma. The alkaline magmatism and the igneous activities ranges from the Columbian (Nuna) to Rodinia and Gondwanaland/Pannotia.

Conflicts of Interest

The author declares no conflicts of interest regarding the publication of this paper.

Acknowledgement

The author is grateful to the Atomic Minerals Directorate for Exploration and Research (AMD), and the Department of Atomic Energy (DAE) for providing logistics for field investigations AMD XRF lab is acknowledged for analytical support.

References

[1] Dayal, B., 1979. A conceptual approach for the possibility of Tin mineralisation associated with acid magmatism in parts of Mirzapur district Uttar Pradesh Proc. workshop (IGCP-26) in Mineralisation associated with acid magmatism (MAWAM 1979). Geological Survey of India. 13, 111-116.

[2] Iqabaluddin, Moghani, A., 1981. Stratigraphy of the Bijawar Group in Sun Valley, Mirzapur district, UP and Sidhi district, MP. Geological Survey of India. 3, 81-93.

[3] Chaubey, V.D., Gupta, A., 1990. The Son-valley greenstone belt-some aspects of Precambrian shield geology, Peninsular India. Journal of the Geological Society of India. 35, 229-305.

[4] Nair, K.K.K., Jain, S.C., Yedekar, D.B., 1995. Stratigraphy Structure and Geochemistry of the Mahakoshal Greenstone belt. Memoir Geological Society of India. 31, 403-432.

[5] Yadav, N.L., 1978. Petrochemistry of Pre-Cambrian rocks of Dudhi area, District Mirzapur UP in Recent research in Geology. Hindustan Publication Corporation: Delhi. pp. 447-465.

[6] Bhattacharya, A.K., Gorikhan, R.A., Khajanchi, B.N., et al., 1992. Uranium mineralization hosted by migmatite-mobilizates and breccia zones in the northwestern part of Chhotanagpur granite gneiss complex, Rihand valley, Sonbhadra district Uttar Pradesh. Indian Journal of Geology. 64(3), 259-275.

[7] Mahadevan, T., 2002. Geology of Bihar and Jharkhand. GSI Publications. 2(1).

[8] Acharyya, S.K., 2003. The nature of mesoproterozoic central Indian tectonic zone with exhumed and reworked older granulites. Gondwana Research. 6, 197-214.

[9] Sarkar, S.N., 1980. Precambrian stratigraphy and geochronology of Peninsular India: A review. Indian Journal of Earth Sciences. 7, 12-26.

[10] Sarkar, A.N., 1982. Precambrian tectonic evolution of Eastern India: A model of converging microplates. Tectonophysics. 86, 363-397.

[11] Sarkar, A.N., 1988. Tectonic evolution of the Chotanagpur Plateau and the Gondwana Basins in Eastern India: An interpretation based on supra-subduction geological processes. Mukhopadhaya, D. (editor), precambrian of the Eastern Indian shield. Geological Society of India Memoir. 8, 127-148.

[12] Chatterjee, N., Banerjee, M., Bhattacharya, A., et al., 2010. Monazite chronology, metamorphism–anatexis and tectonic relevance of the mid-Neoproterozoic Eastern Indian Tectonic Zone. Precambrian Research. 179, 99-120.
DOI: https://doi.org/10.1016/j.precamres.2010.02.013

[13] Chatterjee, N., Ghose, N.C., 2011. Extensive early neoproterozoic high-grade metamorphism in North chotanagpur gneissic complex of the central Indian Tectonic Zone. Gondwana Research. 20(2-3), 362-379.
DOI: https://doi.org/10.1016/j.gr.2010.12.003

[14] Mohanty, S., 2012. Spatio-temporal evolution of the Satpura Mountain Belt of India: A comparison with the Capricorn Orogen of Western Australia and implication for evolution of the supercontinent Columbia. Geoscience Frontiers. 3(3), 241-267.
DOI: https://doi.org/10.1016/j.gsf.2011.10.005

[15] Sanyal, S., Sengupta, P., 2012. Metamorphic evolution of the Chotanagpur Granite Gneiss Complex of the East Indian Shield: Current status. Geological Society, London, Special Publications. 365(1), 117-145.
DOI: https://doi.org/10.1144/sp365.7

[16] Mukherjee, S., Dey, A., Sanyal, S., et al., 2019. Proterozoic crustal evolution of the Chhotanagpur granite gneissic complex, Jharkhand-Bihar-West Bengal, India: Current status and future prospect tectonics and structural geology in Indian Context Soumyajit Mukherjee (editor). Springer International Publication: New York. pp. 7-54.

[17] Auden, J.B., 1933. Vindhyan sedimentation in the sun valley, Mirzapur district. Geological Survey of India. 62(2), 141-250.

[18] Chaubey, V.D., 1970. The Narmada-Son line thrust, the great boundary fault along the southern margin of Vindhyan basin, Central India, West Commemoration volume. Today and Tomorrow's Printers and Publishers, Faridabad: Delhi. pp. 420-438.

[19] Gupta, A., 1982. Interpretation of Landsat imagery of a part of the Son Valley and its correlation with Bouguer gravity and airborne magnetic anomaly data. Journal of the Geological Society of India. 23, 136-145.

[20] Dhurandhar, A.P., Saxena, D.N., 1996. Integrated airborne gamma-ray spectral and satellite data analysis for U and REE mineralisation-A case study from north Sagobandh area, District Sonbhadra, Uttar Pradesh, India. Journal of the Indian Society of Remote Sensing. 27(1), 43-57.
DOI: https://doi.org/10.1007/bf02990774

[21] Dhurandhar, A.P., Rajagopalan, V., Raminaidu, Ch.,

et al., 2003. Petrological and geochemical characterisation of uraniferous pegmatoid leucosomes of Jura, District Sonbhadra, Uttar Pradesh, India. Gond. Geol. Magz. SPL. 7, 279-295.

[22] Dhurandhar, A.P., Latha, A., Krishna, V., 2005. Geochronology and Petrochemistry of the Dubha Granite, Sonbhadra District, Uttar Pradesh. Journal of the Geological Society of India. 65(4), 459-467.

[23] Dhurandhar, A.P., Srivastava, S.K., Sastry, D.V.L.N., et al., 2006. Geochemistry and geochronology of metabasic intrusions in Kirwil-Sagobandh Area, North-western Chhotanagpur Terrain. Indian Journal of Petroleum Geology. 78(1-4), 119-134.

[24] Hansoti, S.K., Deshmukh, A.N., 1990. Structural controls of uranium mineralisation in Proterozoic rocks of Sendur Tatapani area, Sarguja district MadhyaPradesh. Precambians of Central India. Geological Survey of India Special Publication. 28, 676-695.

[25] Streckiessens, A., 1976. To each plutonic rock its proper name. Earth Science Reviews. 12, 1-33.

[26] Ludwing, K.R., 2012. ISOPLOT 3.75 A Geochronological Toolkit for Microsoft Excel. Berkeley Geochronology Center Special Publication. 5, 75.

[27] Pandey, B.K., Gupta, J.N., Sarma, K.J., et al., 1997. Sm-Nd, Pb-Pb, and Rb-Sr geochronology and petrogenesis of mafic dyke swarm of Mahbubnagar, south India: Implications for Paleoproterozoic crustal evolution of the eastern Dharwar craton. Precambrian Research. 84, 181-196.

[28] Wedepohl, K.H., 1969. Handbook of geochemistry. New York: Springer-Verlog. 1, 236.

[29] Gao, S., Luo, T.C., Zhang, B.R., et al., 1998. Chemical composition of the continental crust as revealed by studies in east China. Geochimica et Cosmochimica Acta. 62, 1959-1975.

[30] Thompson, R.N., 1982. Magmatism of the British Tertiary Volcanic Province. Scottish Journal of Geology. 18(1), 49-107. doi: 10.1144/sjg18010049.

[31] McDonough, W.F., Sun, S.S., 1995. The composition of the Earth. Chemical Geology. 120, 223-253.

[32] Maniar, P.D., Piccoli, P.M., 1989. Tectonic discrimination of granitoids. Geological Society of America Bulletin. 101, 635-643.

[33] Cox, K.G., Bell, J.D., Pankhurst, R.J., 1979. The interpretation of igneous rocks. Allen and Unwin: London. pp. 450.
DOI: https://doi.org/10.1007/978-94-017-3373-1

[34] Patiño Douce, A.E., 1999. What do experiments tell us about the relative contributions of crust and mantle to the origin of granitic magmas? Castro, A., Fernandez, C., Vigneresse, J. L. (editors), Understanding Granites: Integrating New and Classical Techniques. Geological Society, London, Special Publications. 168, 55-75.

[35] Condie, K.C., 1973. Archean magmatism and crustal thickening. Geological Society of America Bulletin. 84, 2981-2991.
DOI: https://doi.org/10.1130/0016-7606(1973)84<2981:AMACT>2.0.CO;2

[36] Wilson, M., 1989. Igneous petrogenesis a global tectonic approach. London: Unwin Hyman. pp. 126, 466.

[37] Jung, C., Jung, S., Hellebrand, E., et al., 2009. Trace element constraints on mid-crustal partial melting processes—a garnet ion probe study from polyphase migmatites (Damara orogen, Namibia). Transactions of the Royal Society of Edinburgh Earth Sciences. 100(1-2), 205-218.

[38] Chappell, B.W., White, A.J.R., 1974. Two contrasting granite types. Pacific Geology. 8, 173-174.

[39] Chappell, B.W., White, A.J.R., 2001. Two contrasting granite types: 25 years later. Australian Journal of Earth Sciences. 48, 489-499.

[40] White, A.J.R., Chappell, B.W., 1977. Ultrametamorphism and granitoid genesis. Tectonophysics. 43(1-2), 7-22.
DOI: https://doi.org/10.1016/0040-1951(77)90003-8

[41] White, A.J.R., Chappell, B.W., 1983. Granitoid types and their distribution in the Lachlan Fold Belt, southeast Australia. Roddick, J.A., (editor), Circum-Pacific Plutonic terranes. Geological Society of America, Memoir. 159, 21-34.
DOI: https://doi.org/10.1130/MEM159-p21

[42] White, A.J.R., Chappell, B.W., 1988. Some supracrustal (S-type) granites of the Lachlan Fold Belt. Transactions of the Royal Society of Edinburgh. Earth Sciences. 79, 169-181.

[43] Calvin, F.M., 1985. Are strongly peraluminous magmas derived from pelitic sedimentary sources? Journal of Geology. 93, 673-689.

[44] El Bouseily, A.M., El Sokkary, A.A., 1975. The relation of Rb, Ba, and Sr in granitic rocks. Chemical Geology. 16, 207-219.

[45] Streckeisen, A.L., LeMaitre, R.W., 1979. Chemical approximation to modal QAPF classification of the igneous rocks. Neus Jahrbuch fur Mineralogie. 136, 169-206.

[46] Shaw, D.M., 1968. A review of K-Rb fractionation trends by covariance analysis. Geochimica Et Cosmochimica Acta. 32, 573-601.

[47] Rossi, J.N., Toselli, A.J., Basei, M.A., et al., 2011. Geochemical indicators of metalliferous fertility in the Carboniferous San Blas pluton, Sierra de Velasco, Argentina. Geological Society, London, Special Publications. 350(1), 175-186.
DOI: https://doi.org/10.1144/sp350.1010.1144/sp350.10

[48] Clarke, D.B., 1992. The mineralogy of peraluminous granites: A review. Canadian Mineralogist. 19, 3-17.

[49] Rollinson, H.R., 1993. Using geochemical data: Evaluation, presentation, interpretation. 1st edition. Longman: London. pp. 384.

[50] Janoušek, V., Finger, F., Roberts, M.P., et al., 2004. Deciphering petrogenesis of deeply buried granites: Whole-rock geochemical constraints on the origin of largely undepleted felsic granulites from the Moldanubian Zone of the Bohemian Massif. Earth & Environmental Science Transactions of the Royal Society of Edinburgh. 95, 141-159.
DOI: https://doi.org/10.1017/S0263593300000985

[51] Sylvester, P.J., 1998. Post-Collisional strongly peraluminous granites. Lithos. 45(1-4), 29-44.

[52] Dietrich, V., Gansser, A., 1981. The leucogranites of the Bhutan Himalaya. Schweizer Mineralogisch Petrographische Mitteilungen. 61, 177-202.

[53] Visona, D., Lombardo, B., 2002. Two-mica and tourmaline leucogra-718nites from the Everest-Makalu region (Nepal-Tibet). Himalayan719leucogranite genesis by isobaric heating? Lithos. 62, 125-150.

[54] Watson, E.B., Harrison, T.M., 1983. Zircon saturation revisited: Temperature and composition effects in a variety of crustal magma types. Earth and Planetary Science Letters. 64, 295-304.
DOI: https://doi.org/10.1016/0012-821X(83)90211-X

[55] Watson, E.B., Harrison, T.M., 1984. Accessory phases and the geochemical evolution of crustal magmas. Physics of the Earth and Planetary Interiors. 35, 19-30.
DOI: https://doi.org/10.1016/0031-9201(84)90031-1

[56] Winkler, H.G.F., 1974. Petrogenesis of metamorphic rocks. Springer-Verlag: New York. pp. 320.

[57] James, R.S., Hamilton, D.L., 1969. Phase relation in the system $NaAlSi_3O_8$-$KAlSi_3O_8$-$CaAl_2Si_2O_8$ at 1-kilobar water vapour pressure. Contributions to Mineralogy & Petrology. 21, 111-141.

[58] Wollenberg, H.A., Smit, A.R., 1987. Radiogenic heat production of crustal rocks: an assessment based on geochemical data. Geophysical Research Letters. 14(3), 295-298.

[59] Artemieva, I.M., Thybo, H., Jakobsen, K., et al., 2017. Heat production in granitic rocks: Global analysis based on a new data compilation. GRANITE2017, Earth-Science Reviews. 172, 1-26.

[60] Pearce, J.A., Nigel, B.W.H., Andrew, G.T., 1984. Trace element discrimination diagrams for the tectonic interpretation of granitic rocks. Journal of Petrology. 25, 956-983.

[61] Ghose, N.C., 1992. Chhotanagpur gneiss-granulite complex, eastern India: Present status and future prospect. Indian Journal of Geology. 64(1), 100-121.

[62] Emslie, R.F., 1978. Anorthosite massif, Rapakivi granites and late Proterozoic rifting od North America. Precambrian Research. 7, 61-98.

[63] Dewey, J.F., Bruke, K.C.A., 1973. Tibetian, Variscan and Precambrian basement reactivation products of continental collision. Journal of Geology. 81, 683-692.

[64] Gupta, J.N., Pandey, B.K., Prasad, R.N., et al., 1988. Rb-Sr geochronology of some granitic rocks around Arbail and age of uraniferous aerinite and quartz pebble conglomerates of western Karnataka. Geological Society of India Memoir. 9, 101-108.

[65] Armstrong, R.L., 1968. A model for the evolution of strontium and lead isotopes in a dynamic earth. Reviews of Geophysics. 6(2), 175-199.

[66] Patterson, C., Tatsumoto, M., 1964. The significance of lead isotopes in detrital feldspar with respect to chemical differentiation within the earth's mantle. Geochimica et Cosmochimica Acta. 28, 1-22.

[67] Stueber, A.M., Ramamurthy, V., 1966. Strontium isotope and alkali element abundances in ultramafic rocks. Geochimica et Cosmochimica Acta. 28, 1243-1259.

[68] Faure, G., Hurley, P.M., 1963. The isotopic composition of strontium in oceanic and continental basalts: Application to the origin of igneous rocks. Journal of Petrology. 4, 31-50.

[69] Hurley, P.M., Hughes, H., Faure, G., et al., 1962. Radiogenic strontium-87 model of continent formation. Journal of Geophysical Research. 67, 5316.

[70] Davies, R.D., Allsopp, H.L., Erlank, A.J., et al., 1970. Sr-isotopic studies on various layered intrusions in southern Africa. Special Publication of the Geological Society of South Africa. 1, 576-593.

[71] Moorbath, S., 1975. Evolution of Precambrian crust from strontium isotopic evidences. Nature. 254, 395-398.

[72] Holmes, A., Leland, W.T., Nier, A.O., 1950. Age of uranite from a pegmatite near Singar Gaya district.

India American Mineralogist. 35(1-2), 19-28.

[73] Holmes, A., 1955. Dating the Precambrian of peninsular India and Cylon. Geological Association of Canada. 7, 81-106.

[74] Mandal, P., 2016. Shear-wave splitting in Eastern Indian Shield: Detection of a Pan-African suture separating Archean and Meso-Proterozoic terrains. Precambrian Research. 275, 278-285.
DOI: https://doi.org/10.1016/j.precamres.2016.01.019

[75] Pandey, B.K., Chabria, T., Gupta, J.N., 1995. Geochronological characterisation of the proterozoic terrains of peninsular India: Relevance to the first-order target selection for uranium exploration. Exploration & Research for Atomic Minerals. 8, 187-213.

[76] Pandey, D., Sinha, K.K., Sharma, P.K., 2004. Jhirgadandi Pluton—A Lower Proterozoic, A-Type, Anorogenic, Within—Plate Granite from the son-Narmada Lineament, Sonbhadra district, Uttar Pradesh. Precambrian Crustal Evolution and Metallogenesis with Special Reference to Central India. Hindustan Publishing Corporation (India): New Delhi.

[77] Sastry, D.V.L.N., Krishna, V., Latha, A. (editors), et al., 2017. Rb-Sr and Pb-Pb geochronological studies on the granites of Jaurahi Sonbhadra District UP. National Symposium on Emerging Trends in Geosciences, Mineral Exploration, and Environmental Sciences for Sustainable Developments; 2017 Dec 20-21; Hyderabad, India. India: Indian society of Applied geochemists and Atomic Minerals Directorate for Exploration and Research. p. 49-50.

[78] Sarkar, A., Bodas, M., Kundu, H.K. (editors), et al., 1998. Geochronology and geochemistry of Mesoproterozoic intrusive plutonites from the eastern segment of the Mahakoshal green stone belt, central India. Proceedings of International Seminar on "Precambrian crust in eastern and central India"; Bhubaneswar. p. 82-85.

[79] Pandey, B.K., Krishna, V., Chabria, T. (editors), 1998. An overview of the geochronological data on the rocks of Chhotanagpur gneiss-granulite complex and adjoining sedimentary sequences, Eastern and Central India. Abstract Volume, International Seminar on "Precambrian crust in eastern and central India"; Bhubaneswar. pp. 131-135.

[80] Ray Barman, T., Bishui, P.K., Mukhopadhyay, K., et al., 1994. Rb-Sr geochronology of the high-grade rocks from Purulia, West Bengal, and Jamua-Dumka sector, Bihar. Indian Minerals. 48, 45-60.

[81] Karmakar, S., Bose, S., Sarbadhikari, A.B., et al., 2011. Evolution of granulite enclaves and associated gneisses from Purulia, Chhotanagpur Granite Gneiss Complex, India: Evidence for 990-940Ma tectonothermal event(s) at the eastern India cratonic fringe zone. Journal of Asian Earth Sciences. 41(1), 69-88.
DOI: https://doi.org/10.1016/j.jseaes.2010.12.006

[82] Jain, S.C., Nair, K.K.K., Yedekar, D.B., 1995. Tectonic evolution of the Son-Narmada-Tapti Lineament zone in Geoscientific studies of Son-Narmada-Tapti Lineament zone, Project CRUMENSONATA. Geological Survey of India. 10, 333-371.

[83] Bora, S., Kumar, S., Yi, K., et al., 2013. Geochemistry and U-Pb SHRIMP zircon chronology of granitoids and microgranular enclaves from Jhirgadandi Pluton of Mahakoshal Belt, Central India Tectonic Zone, India. Journal of Asian Earth Sciences. 70-71, 99-114.

[84] Bora, S., Kumar, S., 2015. Geochemistry of biotites and host granitoid plutons from the Proterozoic Mahakoshal Belt, central India Tectonic Zone: Implication for nature and tectonic setting of magmatism. International Geology Review. 57(11-12), 1686-1706.
DOI: https://doi.org/10.1080/00206814.2015.1032372

[85] Mallik, A.K., Gupta, S.N., Ray Barman, T., 1991. Dating of early Precambrian granite–greenstone complex of the Eastern Indian Precambrian shield with special reference to the Chotanagpur granite gneiss complex. Records of the Geological Survey of India. 124, 20-21.

[86] Pandey, B.K., Gupta, J.N., Lal, Y., 1986. Whole rock and mineral isochron ages for the granites from Bihar Mica Belt of Hazaribagh Bihar, India. Indian Journal of Earth Sciences. 12(2&3), 157-162.

[87] Pandey B.K., Upadhyady, L., Sinha, K.K., 1986. Geochronology of Jajawal-Binda-Nagnaha granitoids in relation to uranium mineralization. Indian Journal of Earth Sciences. 12(2&3), 163-168.

[88] Vinogradov, A., Tugarinov, A., Zhykov, C., et al., 1964. Geochronology of Indian Precambrian, 22nd Session of the International Geological Congress. X, 553-567.

[89] Holmes, A., Leland, W.T., Nier, A.O., 1950. Age of uranite from a pegmatite near Singar Gaya district. India American Mineralogist. 35(1-2), 19-28.

[90] Nandi, S.K., Sen, D.N., 1950. Investigation on Indian radioactive minerals, II, Allanite. Journal of

Vacuum Science & Technology. 9, 124-128.

[91] Sarkar, T.C., 1941. The lead ratio of a crystal of monazite from the Gaya district Bihar, India. Proceedings of the Indian Academy of Sciences Section A. 13, 245-248.

[92] Krishnan, M.S., 1953. Structural and tectonic history of India. Geological Survey Memoir. 81, 1-93.

[93] Krishna, V., Sastry, D.V.L.N., Pandey, B.K. (editors), et al., 2003. U-Pb and Pb-Pb ages on columbite-tantalite minerals from pegmatites of Bihar Mica Belt, Jharkhand, India. Silver Jubilee Symp., Nat. Inst. Oceanography, Goa. India: Indian Soc. Mass Spec. p. 650-653.

[94] Lal, N., Saini, H.S., Nagpaul, K.K., et al., 1976. Tectonic and cooling history of the Bihar Mica Belt, India, as revealed by fission-track analysis. Tectonophysics. 34(3-4), 163-180.
DOI: https://doi.org/10.1016/0040-1951(76)90094-9

[95] Aswathanarayana, U., 1956. Absolute ages of the Archaean orogenic cycles of India. American Journal of Science. 254(1), 19-31.
DOI: https://doi.org/10.2475/ajs.254.1.19

[96] Baidya, T.K., Chakravarthy, P.S., 1988. Mineralisation in Belamu-Jaipur sector of northwestern Purulia district, West Bengal. Memoir-Geological Society of India. 8, 147-165.

[97] Singh, Y., Krishna, V., 2009. Rb-Sr geochronology and petrogenesis of granitoids from the chhotanagpur granite gneiss complex of Raikera-Kunkuri Region, Central India. Journal of the Geological Society of India. 74, 200-208.

[98] Ghose, N.C., Smakin, B.M., Smirnov, V.N., 1973. Some geochronological observations on the precambrians of Chhotangpur Bihar, India. Geological Magazine. 110, 477-482.

[99] Sarkar, A. (editor), 1974. K-Ar age of Mahuadanr rhyodacite: Evidence for late Triassic effusive activity in Eastern India. 9th International Gondwana Symposium, Hyderabad. p. 687-695.

[100] Sarkar, A., Paul, D.K., Balasubrahmanyan, M.N., et al., 1980. Lamprophyres from the Indian Gondwanas—K–Ar ages and chemistry. Journal Geological Society India. 21, 188-193.

[101] Baksi, A.K., 1995. Petrogenesis and timing of volcanism in the Rajmahal flood basalt province, northeastern India. Chemical Geology. 121(1-4), 73-90.
DOI: https://doi.org/10.1016/0009-2541(94)00124-q

[102] Sarkar, A., Datta, A.K., Poddar, B.C., et al., 1996. Geochronological studies of Mesozoic igneous rocks of eastern India. Journal of Southeast Asian Earth sciences. 13, 77-81.

[103] Eriksson, P.G., Mazumder, R., Catuneanu, O., et al., 2006. Precambrian continental freeboard and geological evolution: A time perspective. Earth-Science Reviews. 79, 165-204.

[104] Lubnina, N.V., Slabunov, A.I., 2011. Reconstruction of the Kenorland supercontinent in the Neoarchean based on paleomagnetic and geological data. Moscow University Geology Bulletin. 66, 242-249.
DOI: https://doi.org/10.3103/S0145875211040077

[105] Mints, M.V., Eriksson, P.G., 2016. Secular changes in relationships between plate-tectonic and mantle-plume engendered processes during Precambrian time. Geodynamics & Tectonophysics. 7(2), 173-232.
DOI: https://doi.org/10.5800/GT-2016-7-2-0203

[106] Zhang, S., Zheng, X.L., Evans, D.A.D., et al., 2012. Pre-Rodinia supercontinent Nuna shaping up: A global synthesis with new paleomagnetic results from North China. Earth and Planetary Science Letters. 353-354, 145-155.

[107] Nance, D.R., Murphy, B.J., 2013. Origins of the supercontinent cycle. Geoscience Frontiers. 4(4), 439-448.
DOI: https://doi.org/10.1016/j.gsf.2012.12.007

[108] Meert, J.G., Santhosh, M., 2017. The Columbia supercontinent revisited. Gondwana Research. 50, 67-83.

[109] Evans, D.A.D., Mitchell, R.N., 2011. Assembly and breakup of the core of Paleoproterozoic—Mesoproterozoic supercontinent Nuna. Geology. 39(5), 443-446.
DOI: https://doi.org/10.1130/G31654.1

[110] Li, Z.X., Bogdanova, S.V., Collins, A.S., et al., 2008. Assembly, configuration, and break-up history of Rodinia-A synthesis. Precambrian Research. 160(1-2), 179-210.
DOI: https://doi.org/10.1016/j.precamres.2007.04.021

[111] Long, J., Zhang, S., Luo, K., 2019. Cryogenian magmatic activity and early life evolution. Scientific Reports. 9(1).
DOI: https://doi.org/10.1038/s41598-019-43177-8

[112] Dalziel, I.W.D., 1997. Neoproterozoic-Paleozoic Geography and Tectonics: Review, hypothesis, environmental speculation. Geological Society of America Bulletin. 109, 16-42.
DOI: https://doi.org/10.1130/0016-7606(1997)109<0016:ONPGAT>2.3.CO;2

[113] Dalziel, I.W.D., 2013. Antarctica and supercon-

tinental evolution: Clues and puzzles. Earth and Environmental Science Transactions of the Royal Society of Edinburgh. 104, 3-16.

DOI: https://doi.org/10.1017/S1755691012000096

[114] Unrug, R., 2007. Rodinia to Gondwana: The geodynamic map of Gondwana supercontinent assembly. GSA Today. 7(1), 2-6.

[115] Nance, R.D., Murphy, J.B., 2018. Supercontinents and the case for Pannotia. Wilson, R.W., Houseman, G.A., Mccaffrey, K.J.W., Doré, A.G., Buiter, SJH (editors). Fifty Years of The Wilson Cycle Concept in Plate Tectonics. 470, 1-17.

DOI: https://doi.org/10.1144/ SP470.5

[116] Kent, R.W., Storey, M., Saunders, A.D., 1992. Large igneous provinces: Sites of plume impact or plume incubation. Geology. 20, 891-894.

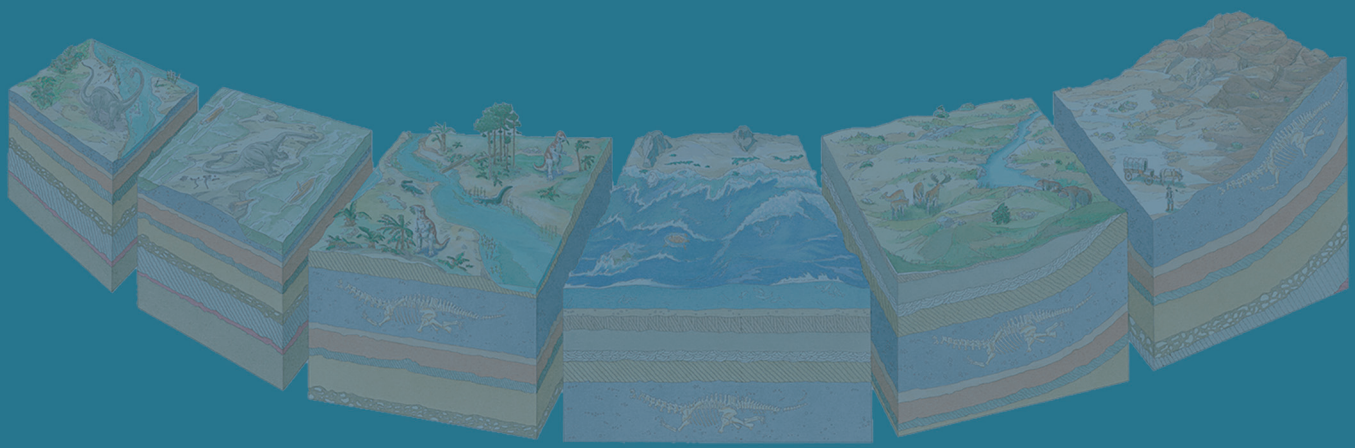

BILINGUAL
PUBLISHING GROUP
Pioneer of Global Academics Since 1984

Tel:+65 65881289
E-mail: contact@bilpublishing.com
Website:https://journals.bilpubgroup.com

2810-9384
01
9 772810 938231